FEDERAL UNIVERSITY OF SÃO CARLOS
CENTER FOR EXACT SCIENCES AND TECHNOLOGY
GRADUATE PROGRAM IN MATERIALS SCIENCE AND ENGINEERING

IONIC CONDUCTIVITY IN GLASSES: FUNDAMENTALS AND APPLICATION TO SOLID STATE BATTERIES

Vinicius Martins Zallocco

São Carlos-SP
2026

FEDERAL UNIVERSITY OF SÃO CARLOS
CENTER FOR EXACT SCIENCES AND TECHNOLOGY
GRADUATE PROGRAM IN MATERIALS SCIENCE AND ENGINEERING

IONIC CONDUCTIVITY IN GLASSES: FUNDAMENTALS AND APPLICATION TO SOLID STATE BATTERIES

Vinicius Martins Zallocco

Thesis submitted to the Graduate Program in Materials Science and Engineering in partial fulfillment of the requirements for the degree of Ph.D. in Materials Science and Engineering

Supervisor: Prof. Dr. Ana Candida Martins Rodrigues
Funding agencies: FAPESP (grant: 2021/12412-8 and 2013/07793-6) and CAPES PrInt (grant: 88887.936884/2024-00)

São Carlos-SP
2026

DEDICATION

To my family, for their unconditional love and support.

VITAE

Master degree in Materials Science and Engineering from the Federal University of São Carlos (UFSCar), São Paulo, Brazil (2021).
Bachelor degree in Civil Engineering from the FEI University Center, São Bernardo do Campo, São Paulo, Brazil (2019).

UNIVERSIDADE FEDERAL DE SÃO CARLOS

Centro de Ciências Exatas e de Tecnologia
Programa de Pós-Graduação em Ciência e Engenharia de Materiais

Folha de Aprovação

Defesa de Tese de Doutorado do candidato Vinicius Martins Zallocco, realizada em 09/02/2026.

Comissão Julgadora:

Profa. Dra. Ana Candida Martins Rodrigues (UFSCar)

Prof. Dr. Marcello Rubens Barsi Andreeta (UFSCar)

Prof. Dr. Marco Aurelio Liutheviciene Cordeiro (UFSCar)

Prof. Dr. Caio Barca Bragatto (AU)

Prof. Dr. Rafael Bianchini Nuernberg (ICMCB)

O Relatório de Defesa assinado pelos membros da Comissão Julgadora encontra-se arquivado junto ao Programa de Pós-Graduação em Ciência e Engenharia de Materiais.

ACKNOWLEDGMENTS

To my family, especially my father and my mother, for their unconditional emotional support.

To Professor Dr. Ana Candida Martins Rodrigues, for the opportunity, freedom, and trust in allowing me to explore new horizons in this work.

To the entire LaMaV community, especially Ricardo Felipe Lancelotti and João Victor Campos, for the enriching discussions and their willingness to collaborate.

To the LaMaV technician, José Rodrigues da Silva – Zé, for his attention and daily assistance in the laboratory.

To the entire ICGM community, especially Laure Monconduit and Lorenzo Stivano, for their invaluable willingness to teach, guide, and support my development as a researcher.

To the University Mountaineering and Hiking Club (C.U.M.E), for all the friendships and outdoor activities that were essential to maintaining emotional and mental balance throughout this journey.

To FAPESP, for the CEPID thematic project that enabled a scholarship, allowing me to dedicate myself fully to research. FAPESP (grant: 2021/12412-8 and 2013/07793-6).

To CAPES PrInt, for the financial support that allowed me to develop my career in applied technology, which was fundamental in enabling me to be where I am professionally today. CAPES PrInt (grant: 88887.936884/2024-00).

To the staff of the SENAI Institute of Innovation in Electrochemistry, who supported and helped me in numerous ways during the final stage of my PhD.

This study was financed in part by the Coordenação de Aperfeiçoamento de Pessoal de Nível Superior - Brasil (CAPES) - Finance Code 001.

ABSTRACT

Understanding ionic transport in solids is critical for advancing solid-state electrolytes, where Ionic conductivity is mainly the product of the effective charge carrier density and its mobility. However, due to the low mobility of ions in solid-state, measuring the individual contributions of mobility and effective charge carrier density represents an experimental challenge. In this work, electrochemical impedance spectroscopy combined with space charge polarization theory is employed to independently quantify the effective charge carrier density in ion-conducting glasses. A systematic investigation of lithium disilicate glass establishes optimized experimental conditions and reveals that only a small fraction of alkali ions contributes to ionic conduction at room temperature. Extension of this methodology to lithium silicate and phosphate glasses demonstrates a composition-dependent two-regime behavior: at moderate alkali concentrations, conductivity enhancements are primarily governed by increases in effective charge carrier density, whereas near vitrification limits ionic mobility becomes the dominant factor. Additionally, the incorporation of chloride into $Li_2O–P_2O_5–AlCl_3$ glasses significantly enhances ionic conductivity. Since the addition of $AlCl_3$ does not introduce new cationic charge carriers such as Li^+, the observed enhancement in ionic conductivity must instead originate from an interaction between chloride anions and the glass network. Finally, these fundamental insights are translated into application through the development of a solvent-free, photo-cross-linked glass–polymer composite electrolyte, which exhibits improved electrochemical stability, reduced interfacial resistance, and superior performance in all-solid-state lithium battery cells compared to conventional polymer electrolytes.

Keywords: ionic conductivity; effective charge carrier; interfacial capacitance; electrode polarization; complex impedance.

RESUMO

CONDUTIVIDADE IÔNICA EM VIDROS: FUNDAMENTO E APLICAÇÃO EM BATERIAS DE ESTADO SÓLIDO

A compreensão do transporte iônico em sólidos é fundamental para o avanço de eletrólitos de estado sólido, nos quais a condutividade iônica resulta da densidade efetiva de portadores de carga e de sua mobilidade. Contudo, a baixa mobilidade dos íons dificulta a determinação experimental independente dessas contribuições. Neste trabalho, a espectroscopia de impedância eletroquímica, combinada com a teoria da polarização de carga espacial, é utilizada para quantificar a densidade efetiva de portadores de carga em vidros condutores iônicos. Uma investigação sistemática do vidro dissilicato de lítio estabelece condições experimentais otimizadas e revela que apenas uma pequena fração dos íons alcalinos contribui para a condução iônica à temperatura ambiente, sendo essa fração efetiva dependente da temperatura. A aplicação da metodologia a vidros silicatos e fosfatos de lítio revela dois regimes distintos: em concentrações moderadas de álcalis, a condutividade é dominada pelo aumento da densidade de portadores de carga, enquanto, próximo aos limites de vitrificação, a mobilidade iônica torna-se predominante. A incorporação de cloreto em vidros $Li_2O–P_2O_5–AlCl_3$ aumenta a condutividade iônica. Uma vez que a adição de $AlCl_3$ não introduz novos portadores de carga catiônicos, como Li^+, o aumento observado na condutividade iônica deve, em vez disso, originar-se de uma interação entre os ânions cloreto e a rede vítrea. Por fim, esses conceitos são aplicados no desenvolvimento de um eletrólito compósito vidro–polímero, livre de solventes e foto-reticulado, com melhor estabilidade eletroquímica e desempenho superior em baterias de lítio totalmente em estado sólido.

Palavras-chave: condutividade iônica; portador de carga efetivo; capacitância interfacial; polarização de eletrodo; impedância complexa.

PUBLICATIONS

Roni A. Silva et all. (2025). Structure–property relationships in sodium phosphate glasses and glass-ceramics containing tantalum oxide. ***Journal of the American Ceramic Society.***

V.M. Zallocco, J. V. Campos, A. C. M. Rodrigues. (2024). Interfacial capacitance in lithium disilicate glass: Experimental factors and charge carrier density. ***The American Ceramic Society***.

J. V. Campos, I. R. Lavagnini, **V. M. Zallocco**, L. M. Jesus, A. C. M. Rodrigues. (2023). Ultrafast crystallization and sintering of Li1.3Al0.3Ti1.7(PO4)3 glass through flash sinter-crystallization. ***The American Ceramic Society***.

J. V. Campos, I. R. Lavagnini, **V. M. Zallocco**, E. B. Ferreira, E. M. J. A. Pallone, A. C. M. Rodrigues. (2023). Flash sintering with concurrent crystallization of $Li_{1.5}Al_{0.5}Ge_{1.5}(PO_4)_3$ glass. ***Acta Materiali***

TABLE OF CONTENTS

CHAPTER 1 - INTRODUCTION

The growing interest in solid-state electrolytes for various technologies — including solid-state batteries — has driven the academic community to deepen its understanding of the fundamental mechanisms governing ionic transport in solids. It is widely acknowledged that ionic conductivity under a DC electric field ($\sigma_{d.c.}$) follows the relationship:

$$\sigma_{d.c.} = n_e \, Z \, e \, \mu, \qquad (1)$$

where n_e is the effective charge carrier density, Z the ion valency, e the elementary charge and μ the ion mobility. One open question related to glass ionic conductivity is whether all mobile ions, or a fraction of them, contribute to the ionic conduction phenomena. In fact, independent determination of mobility and effective charge carrier density in solids is a challenging task. For instance, while for semiconductors the electron's mobility is easily determined by the Hall effect, in ionic conductors, however, this technique yields minute Hall voltages [1,2] that are hardly measurable. This issue stems from the significantly lower ionic mobility compared to the electron mobility in electronic conductors.

Shedding light on the interdependence between charge carrier density and mobility would deepen our understanding of solid-state ionic conductivity. This, in turn, could pave the way for tailoring chemical compositions to enhance ionic conductivity, one of the primary limitations hindering the widespread application of solid electrolytes in solid-state batteries.

Chapter 2 of this thesis presents the state of the art in our understanding of ionic conductivity in glasses, highlighting the techniques previously employed to explore the interdependence between charge carrier density and mobility, along with their implications and key conclusions.

Chapter 3 employs a widely known glass in glass science, lithium disilicate (LS2), to explore the effect of experimental factors to determine the effective charge carrier density using the space-charge polarization phenomena. By applying theoretical equation on optimal experimental

conditions, we found out that 1% of all ions in LS_2 participate effectively on the ionic conduction at 25 °C. This ratio increases to 5 and 12% at 130 and 280 °C, respectively.

Chapter 4 employs the optimal experimental condition found in Chapter 3 to better understand the relationship between charge carrier density and their mobility as a function of lithium concentration by measuring the effective charge carrier density in 55 Li_2O – 45 P_2O_5, 55 Li_2O – 60 P_2O_5, 40 Li_2O – 45 P_2O_5, 33 Li_2O – 67 SiO_2 and 40 Li_2O – 60 SiO_2. It was found a two-regime behavior: at moderate alkali concentration, conductivity increase is driven primarily by a rise in charge carrier concentration (n_e) while mobility (μ_{ion}) remains nearly composition-independent. Near vitrification limits of both systems, the increase in ionic conductivity seems to be mobility controlled.

Chapter 5 presents results on the increase in ionic conductivity in the new glass system $(100–x)[\ yLi_2O–(100–y)P_2O_5)]–xAlCl_3$, with x = {5, 10, and 15}. Since the addition of $AlCl_3$ does not introduce new cationic charge carriers such as Li^+, the observed enhancement in ionic conductivity must instead originate from a synergistic interaction between chloride anions and the glass network. Overall, these findings demonstrate that the incorporation of different anions is a promising approach to increase conductivity and thereby aid the design of high-performance solid electrolytes.

Chapter 6 focuses on the technological application of glasses in all-solid-state batteries. Two glass compositions and an amorphous one were explored — 64.5 Li_2O – 35.5 P_2O_5, 50 Li_2O – 50 Nb_2O_5 – 20 P_2O_5, and LiPON (60 $LiPO_3$ – 40 Li_3N) — to develop a solvent-free, photo-cross-linked composite glass-polymer electrolyte (CSE). The CSE demonstrated superior electrochemical performance compared to the standard solid polymer electrolyte (SPE), including higher oxidation potential, lower charge transfer resistance, improved chemical stability, and enhanced plating/stripping stability. Additionally, coin cell solid-state batteries (Li/solid-electrolyte/LFP) were assembled, showing that the CSE enabled better capacity retention at different discharge rates than the SPE.

Chapter 7 concludes the thesis by summarizing the main findings.

CHAPTER 2 - BACKGROUND

Chapter 2 of this thesis presents the state of the art in understanding ionic conductivity in glasses. It explores the fundamental aspects governing ionic transport and examines key experimental techniques already employed by scientific community to investigate the interdependence between charge carrier density and mobility. The discussion highlights findings from the literature along with their implications for understanding conductivity in disordered solids. The chapter concludes by introducing the concept of space charge polarization, which forms the central methodological approach adopted in this study.

2.1 The Vitreous State

Edgar Zanotto and John Mauro [3] define glass as “a condensed state of matter, out of its thermodynamic equilibrium (metastable), non-crystalline, and which exhibits the glass transition phenomenon (Tg). The structure of glasses is similar to that of their supercooled liquid (SCL) counterparts, and they spontaneously relax toward the SCL state. Their ultimate fate is crystallization”. More simply, a glass is formed when a liquid is cooled rapidly enough to avoid crystallization, resulting in the vitreous state of matter defined above.

Structurally speaking, the atoms in glass form an extensive three-dimensional network. This network lacks the long-range periodicity and symmetry found in crystals but is not entirely disordered like in amorphous materials. In other words, glasses exhibit short-range order. For instacen, Figure 2-1 illustrates the structural differences between a crystalline and a glassy oxide material (e.g., SiO_2) [4]. The crystalline state shows long-range atomic order and symmetry (Figure 2-1a), while the glassy state does not (Figure 2-1b). However, the distances and bonding between first-neighbor atoms (Si – O and O – O) are essentially the same in both cases, showing the short-range order. For instance, glassy silica features a highly connected network where $[SiO_4]^{4-}$ tetrahedra are linked via bridging oxygen atoms (– Si –

O – Si –). These are the same tetrahedral units found in crystalline forms such as tridymite and cristobalite, differing only in the bond angles between them.

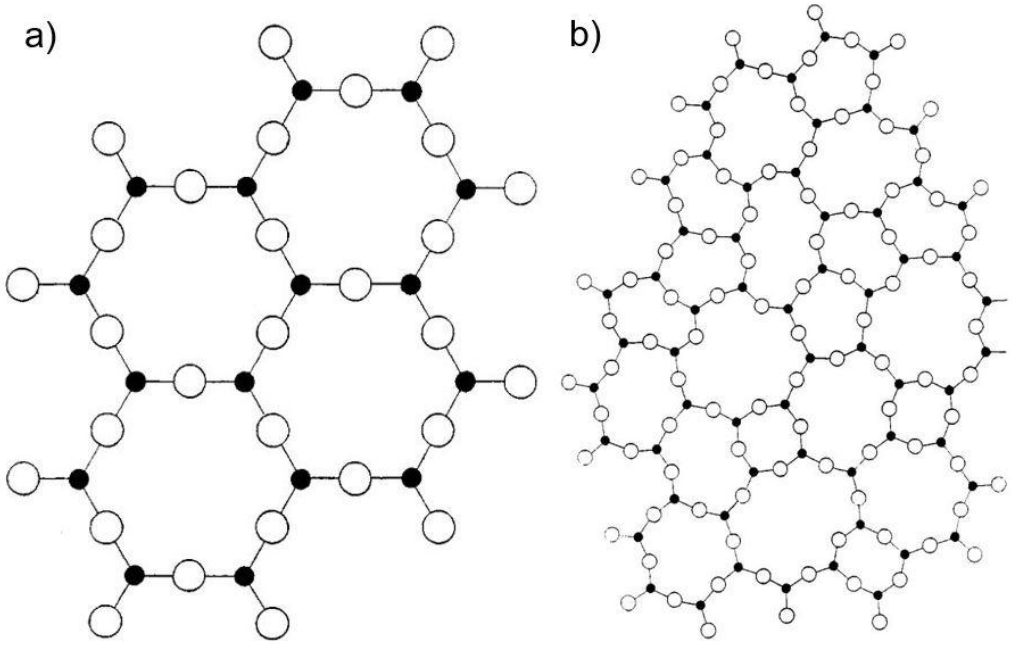

Figure 2-1. Two-dimensional illustration of a (a) crystalline and (b) glassy structure for an oxide such as SiO2. The black circles represent silicon atoms while the white circles represent oxygen atoms. Adapted from [4]. According to Zachariazen, this drawing represents a crystal of the A2O3 type - but it could represent silica, if we assume that a fourth oxygen is above or below the plane of the sheet.

In most cases, glass is formed from a mixture of chemical elements. It is therefore convenient to categorize these elements into two groups: network formers (NWF) and network modifiers (NWM). Network formers are oxides that, as the name implies, contribute to the formation of the glass network. Examples include SiO_2, GeO_2, MoO_3, B_2O_3, Al_2O_3, Sb_2O_3, As_2O_3, P_2O_5, V_2O_5, As_2O_5, and Ta_2O_5 [4,5]. It is worth noting that not all of these oxides vitrify on their own — for instance, MoO_3 does not — but they can participate in glass network formation when combined with other formers [5]. On the other hand, network

modifiers are oxides that break the network's connectivity. This is the case for alkali oxides (M_2O, where M = Li, Na, K...) and alkaline earth oxides (MO, where M = Mg, Ca, Sr...). These modifiers disrupt the covalent – O – Si – bonds, forming ionocovalent – O···M interactions (with covalent bonds represented by dashes and ionic interactions by dots), leading to the creation of nonbridging oxygen atoms (NBOs) [5]. Figure 2-2 schematically illustrates how the structure of vitreous silica is modified when Na_2O and CaO are added to the system [5].

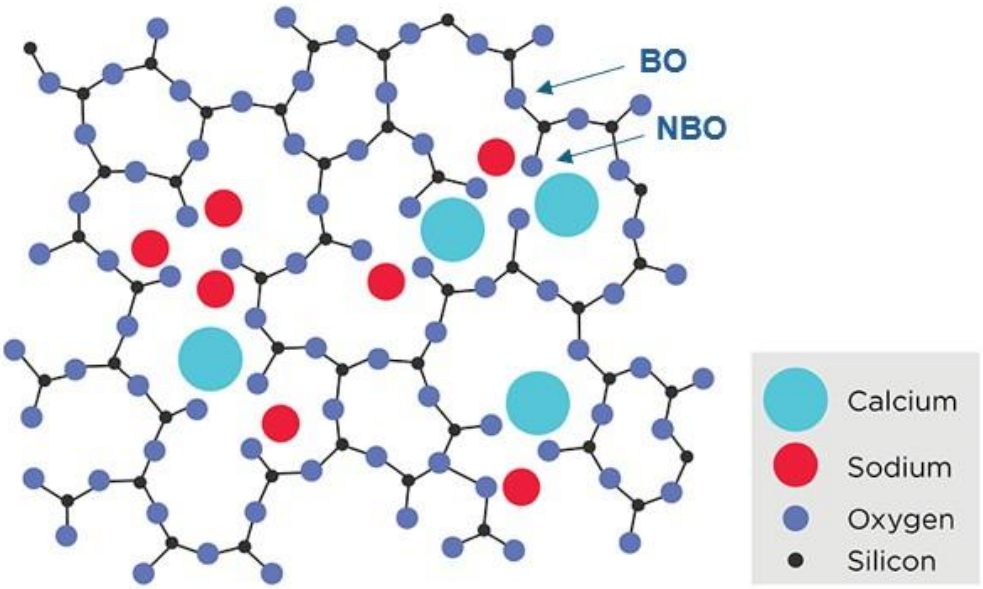

Figure 2-2. Two-dimensional illustration of the atomic structure of a soda-lime-silica glass, highlighting bridging oxygens (BOs) bonded to network-forming atoms (Si) and nonbridging oxygens (NBOs) associated with network-modifying cations (Na, Ca). Adapted from [5].

2.2 Ionic conductivity in Glass

Ionically conducting glasses are those that contain significant amounts of network modifiers, such as lithium or sodium. In these glasses, ionic conductivity occurs almost entirely through the movement of alkali ions, meaning that the ionic transport number (t_{ion}) is approximately 1. As shown in Equation (1) of Chapter 1, the ionic conductivity of the system is determined by the concentration of effective charge carriers, their mobility, and the valence of

the ion. Experimentally, it is widely accepted that the temperature dependence of conductivity (σ(T)) in glasses follows the relationship expressed by an Arrhenius equation, Equation (1):

$$\sigma_{d.c.}(T) = \sigma_0 \exp\left(-\frac{E_{ion}}{kT}\right), \qquad (1)$$

where σ_0 is the pre-exponential factor, T is the temperature, *k* is the Boltzmann constant, and E_{ion} is the activation energy for the ionic conduction process. The main difference between glasses and crystals lies in the fact that glasses do not exhibit a single, well-defined activation energy value [6]. For instance, Figure 2-3 schematically illustrates the difference in energy barrier profiles between a glass and a crystal. The energy landscape for ion transport differs markedly between glasses and crystals. In glasses, the non-crystalline structure leads to an irregular, non-periodic energy profile with variable barrier heights and hopping distances, resulting in a broad distribution of activation energy. In contrast, crystals exhibit a periodic and uniform energy landscape, with consistent and well-defined pathways for ion migration. This comparison helps to explain that in crystals, ions hop consistently from site to site due to the uniformity of the energy barriers. In glasses, however, ions must navigate a more irregular energy landscape, occasionally encountering high or low barriers, leading to a more tortuous and energetically heterogeneous conduction path. However, it is important to mention that the activation energy E_{ion} – expression 1 measured experimentally is the result of these irregular energy landscape and the average of all energy barriers.

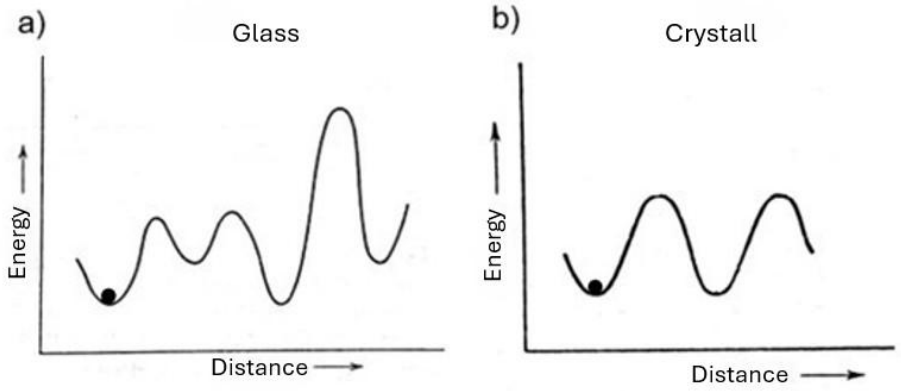

Figure 2-3. Illustration of energy barriers along a one-dimensional migration path for an ion in (a) a glassy and (b) a crystalline network. Adapted from [6].

Since ionic conductivity is essentially a hopping process, it is also widely accepted that both the number of charge carriers and their mobility are thermally activated, each associated with its own activation energy, as expressed in Equations (2) and (3) [2,7]:

$$n(T) = n_0 \exp\left(-\frac{E_c}{kT}\right), \quad (2)$$

$$\mu(T) = \mu_0 \exp\left(-\frac{E_m}{kT}\right), \quad (3)$$

In this sense, by combining Equation (1) of Chapter 1 with Equations (2-3) from this Chapter, the temperature dependence of ionic conductivity can be rearranged into Equation (4). This equation is particularly important, as it provides the foundation for the subsequent discussion on ionic conductivity throughout this thesis.

$$\sigma_{d.c.}(T) = eZn_0\mu_0 \exp\left(-\frac{(E_c + E_m)}{kT}\right), \quad (4)$$

2.2.1 Key Determinants in Solid-State Ionic Conductivity

2.2.1.1 Alkali Concentration

As previously mentioned, ionic conductivity in glasses is closely related to the quantity and type of mobile charge-carrying ions. Figure 2-4 illustrates the increase in ionic conductivity in lithium [8] and sodium [9] silicate glasses as a function of alkali content. It is particularly noteworthy that there is a sharp increase in conductivity for alkali concentrations (x) below $x < 0.10$. For concentrations above this threshold ($x > 0.10$), the increase in conductivity becomes monotonic, though not linear, as the conductivity axis is presented on a logarithmic scale.

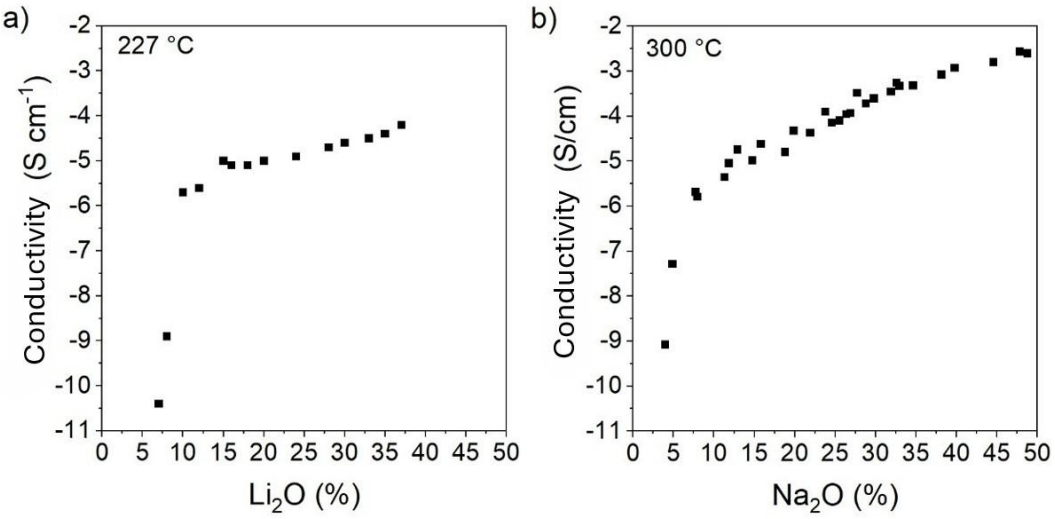

Figure 2-4. Variation of ionic conductivity in silicate glasses as a function of (a) Li_2O and (b) Na_2O concentration. Data were extracted from the SciGlass software, which referenced article [8] for lithium and a book [9] for sodium.

This behavior can be attributed to structural changes within the glass network induced by the addition of alkali oxides. Introducing alkali oxides such as Li_2O or Na_2O into the glass matrix leads to the formation of non-bridging oxygens (NBOs). Each alkali ion introduced breaks a ionocovalent bond, resulting in an oxygen atom bonded to only one glass former atom, with its negative charge balanced by a nearby alkali cation, as can be seen in Figure 2-2. This process effectively depolymerizes the glass network, reducing its rigidity and creating more open pathways for ion diffusion, introducing sites that facilitate ion hopping.

To explain this effect, the weak electrolyte theory [10], proposed by Ravaine & Souquet, suggests that alkaline oxides (solute, e.g., Li_2O) are weakly dissociated in the glass matrix (solvent, e.g., SiO_2) (hence the name weak electrolyte theory), according to the equilibrium described by equation (5):

$$Li_2O \leftrightarrow LiO^- + Li^+ \qquad (5),$$

where only a fraction of the available lithium atoms would be effective charge carriers as Li^+ [1,10,11] . Furthermore, it proposes that mobility is independent

of the chemical composition. This theory helps to explain the large, non-linear variations in conductivity for modifier oxide concentrations greater than 10 mol%. For concentrations less than 10 mol%, Varshneya [5] proposes that liquid phase separation is responsible for the even more abrupt variation in conductivity. The hypothesis is that at low concentrations (~1% of Li_2O), the glass nano-structure would consist of droplets of a lithium-rich phase immersed in a matrix (another phase) with lower lithium content. In this way, as lithium concentration increases, the number of these droplets would increase until they touch, resulting in interconnected channels that would explain the sharp increase up to 10%. However, in his book, there are no referenced studies or micrographs demonstrating this interconnectivity of lithium-rich phases. Furthermore, it is important to emphasize that liquid phase separation occurs in lithium silicates for concentrations below 32% Li_2O [12]

2.2.1.2 Positive Mixed Glass Former Effect (PMGFE)

The positive mixed glass former effect (PMGFE) refers to the phenomenon where the partial substitution of one glass former with other results in an enhancement of ionic conductivity — without an increase in the concentration of mobile charge carriers. This effect highlights that ionic transport in glasses is influenced not only by the number of carriers but also by the structural configuration of the glass network.

For example, Figure 2-5 illustrates this behavior in the Li_2O–Al_2O_3–P_2O_5 glass system, where the highest ionic conductivity (~3.4×10^{-7} S cm^{-1} at 50 °C) is observed at 6.25 mol% Al_2O_3. This enhancement is attributed to a combination of phosphate network depolymerization, an increased number of non-bridging oxygens (NBOs), and changes in aluminum coordination environments [13,14]. These structural adjustments lead to a reduction in molar volume and a shortening of the lithium ion hopping distance, thereby enhancing ionic transport.

A similar trend is observed in the the Li_2O – Nb_2O_5 – P_2O_5 glass system, show in Figure 2-5b. In this case, the addition of Nb_2O_5 results in the formation

of P–O–Nb bonds and the incorporation of [NbO_6] units into the glass network [15,16]. These units introduce negatively charged sites that provides favorable environments for Li^+ migration by creating energetically favorable pathways for conduction [15,16]. Again, this improvement in conductivity occurs without increasing the overall Li^+ content, highlighting the PMGFE.

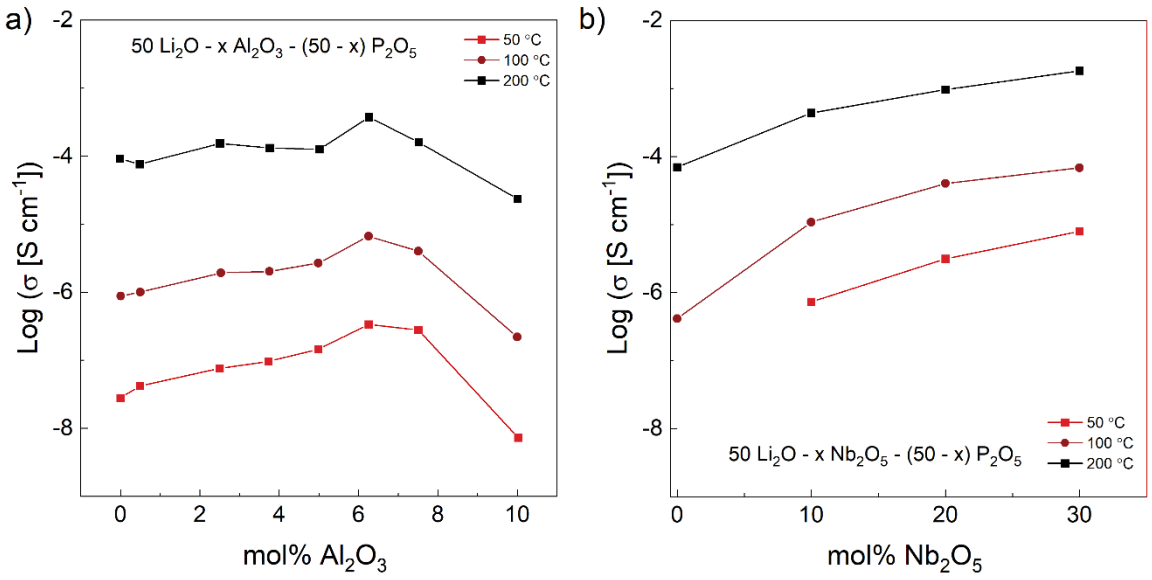

Figure 2-5. Enhancement of ionic conductivity due to the positive mixed glass former effect for (a) 50 Li_2O – x Al_2O_3 – (50-x) P_2O_5 and (b) 50 Li_2O – x Al_2O_3 (50-x) P_2O_5. Data were extracted, respectively, from [13,14] and [15,16].

2.2.1.3 Halogen Incorporation

The incorporation of halogens into glass structures to enhance ionic conductivity has been recognized since the pioneering work of Malugani and Robert [17,18], and later Levasseur et al. [18]. In recent years, numerous studies [17–24] have investigated the effects of adding lithium halides — such as LiX (X = F, Cl, Br, I) — to glass systems. These works demonstrate that ionic conductivity can be significantly improved through partial substitution of Li_2O with Li_2X_2, even without increasing the overall concentration of charge carriers [19,20,25].

Unlike PMGFE, where conductivity enhancement is typically linked to structural rearrangements within the glass network, halogen incorporation appears to follow a different mechanism. Several studies report that halide ions do not actively participate in the glass network formation and remain decoupled from glass network [17–19,22,26]. As a result, the enhancement in conductivity is not attributed to changes in network connectivity or polymerization. However, it is still unclear if the increased ionic conductivity can be attributed to the mobility of Li^+ ions facilitated by the presence of halides, which may influence the local ionic environment and reduce the energy barrier for ion hopping.

2.3 Activation Energy, Charge Carrier Density and Mobility

From the evidence presented above, ionic conductivity in glasses can be enhanced through various strategies. In some cases, such as alkali oxide addition, conductivity improvements arise from an increased concentration of charge carriers. In others, like the positive mixed glass former effect (PMGFE), structural modifications within the glass network led to enhanced conductivity without altering the concentration of charge carrier. Additionally, in cases such as halogen incorporation, improvements occur even without significant structural changes or increases in charge carrier concentration. As outlined in Equation (1) of Chapter 1, ionic conductivity fundamentally depends on the concentration of charge carriers and their mobility. Therefore, understanding the individual contributions of these parameters — charge carrier density and ionic mobility — and determining whether one dominates over the other is crucial for a deeper comprehension of the mechanisms governing ionic conduction in solid-state systems. To achieve this, studies must often focus on the independent determination of either the charge carrier concentration or the ionic mobility within a given glass composition.

Before reviewing the methods and models used to determine these individual contributions to ionic conductivity, it is important to address a common misconception in the literature regarding the distinction between

"weak" and "strong" electrolyte behavior in glasses. On one end of the spectrum, Ravaine and Souquet [10] proposed that only a small fraction of ions is dissociated – thus forming the basis of the so-called “weak electrolyte model” – and contributes to the conduction phenomenon, with ionic mobility considered independent of chemical composition. On the opposite end, Steve Martins [27] introduced the term “strong electrolyte” – suggesting that all ions contribute to the conduction process - and justified it based on the Anderson-Stuart model [28]. However, a careful analysis of Anderson-Stuart model [28] reveals that the model is primarily focused on developing a structural approach for estimating the activation energy of the ionic conductivity, rather than specifying the number of mobile ions. Indeed, as will be explored in the next paragraphs, the Anderson-Stuart model [28] agrees in certain level with Ravaine and Souquet [10].

As a scientist, it is important to question whether there are any other possibilities besides these two extremes. It is reasonable that these models represent limiting cases, and that the actual behavior depends on the specific glass composition — in some systems, the number of effective charge carriers may vary significantly, while in others, mobility may play a more dominant role. Consequently, compositional dependence on conductivity can differ from one material system to another, with both parameters contributing to the observed behavior.

Ravaine and Souquet investigated ionic transport by constructing a concentration cell by juxtaposing two silicate glass samples with different Na_2O concentrations (glass 1 and glass 2). By measuring the cell voltage, they calculated the thermodynamic activity of M_2O. Their results demonstrated that ionic conductivity is proportional to the chemical activities (a), which is, in turn, related to the concentration of the effective charge carrier (C^+). From this analysis, they inferred that ionic conductivity primarily depends on the concentration of effective charge carriers, as expressed by Equation (6). Moreover, they argued that mobility is composition-independent, as reflected in Equation (6), where the mobility term is absent.

$$\frac{\sigma_1}{\sigma_2} \propto \frac{a_{M2O}^1}{a_{M2O}^2} \propto \frac{C_1^+}{C_2^+}, \qquad (6)$$

Later, Souquet et al. [1], based on the ionic conductivity values above and below glass the transition temperature (T_g), proposed a model to calculate the charge carrier formation and mobility enthalpies, which allows the determination of effective charge carrier density. Using their model, authors found that alkali disilicate glasses have an effective charge carrier ratio (n_e / n_t, n_t = total number of charge carrier) about 10^{-4} at 227 °C and 10^{-7} -10^{-9} at room temperature. They concluded that in the studied glass system, i.e, alkali disilicate, mobility is independent of alkali concentration, where just a small part of all ions effectively contributes to the conduction phenomena, inferring that ionic conductivity is largely related to the charge carrier concentration.

Anderson and Stuart [28] proposed the determination of activation energy of ionic conductivity (E_a) as a sum of the energy required to move the ion from one equilibrium position to the other (electrostatic energy, E_b) plus the energy required to deform the glass network to allow the movement of the ion (strain energy, E_s), as expressed by Equation (7). The first energy (E_b) is determined by using classical theory of ionic crystal while the second energy (E_s) is determined by the theory of elasticity.

$$E_a = E_b + E_s, \qquad (7)$$

The most significant aspect of this theory lies in its implications. For instance, in their study on oxide glasses with varying composition of sodium oxide (Na_2O) and silica (SiO_2) [28], they have concluded that binding energy plays a more dominant role than strain energy. Specifically, as sodium oxide content increases from 8.4% to 35.7%, the proportion of binding energy decreased slightly from 87% to 85%, while the strain energy increased slightly from 13% to 15% of the total activation energy. The total activation energy itself decreased from 21.6 to 15.0 kcal/mol (0.94 to 0.65 eV). Similar results were obtained by Steve Martin [29], who applied this model to a sodium borate

system. He found that increasing the sodium oxide content from 1% to 10.3% led to a decrease in binding energy from 87% to 73%, while the strain energy increased from 13% to 27%. Although the changes are more pronounced in borate glasses, both studies demonstrate that binding energy plays a more dominant role in the formation of the charge carrier than in its mobility. In this context, the Anderson and Stuart model [28] aligns with the conclusions of Ravaine and Souquet [10], suggesting that conductivity is primarily determined by charge carrier density—that is, by binding energy.

Almond, Duncan, and West [30] considering the dispersion frequency ($f_{dispersion}$ is the frequency where $2*\sigma_{d.c.} \sim \sigma_{a.c.}$) of the ionic conductivity as being equal to the frequency of effective jumps have determined the charge carrier concentration for β-alumina, polycrystalline Li_4SiO_4, $Ag_7I_4AsO_4$ glass, and K/Ca nitrate glass. The authors have estimated the percentage of effective charge carrier for these materials, being 22.0%, 0.5%, 1.1%, and 0.1%, respectively. Additionally, they concluded that the increase in ionic conductivity with temperature in β-alumina, polycrystalline Li_4SiO_4, $Ag_7I_4AsO_4$ glass, and K/Ca nitrate glass would be mainly due to the increase in mobility of the charge carriers. Despite the fact that this study discusses different glasses, it is worth mentioning that the concentration of charge carriers is orders of magnitude higher than that published by Souquet et al. [1].

As we can observe, there is no consensus about the individual contribution of mobility and charge carrier concentration, where the main difficulty relies in how to determine both terms from expression 1 experimentally. In fact, the Hall effect is widely employed in semiconductors to determine charge carrier mobility; However, when applied to ionic conductors, this technique presents considerable challenges because ionic mobilities are several orders of magnitude lower than those of electrons. Consequently, this technique yields minute Hall voltages [1,2] that are hardly measurable, making it technically difficult to interpret the signals with sufficient precision. Nevertheless, some measurements have been done in ionic conductors. For example, into the context of crystalline materials, examples include α-AgI [31], $C_5H_6NAgI_6$ [32],

and α-$RbAg_4I_5$ [33]. When it comes to ionic glasses, applications of the Hall effect are even more limited. One of the very few known examples is the work by Clement et al. [34], who investigated the system $xAgI\cdot(1–x)AgPO_3$. [6,11]

Another approach proposed to calculate the concentration of charge carriers, independently of mobility involves electrochemical impedance spectroscopy combined with space charge polarization. When using blocking electrodes, at low frequencies an electrical double layer forms — a phenomenon also referred to as ‘electrode polarization’. According to space charge layer theory, a robust and well-established theory presented by McDonald [35], describes an interfacial capacitance that arises from this electrode polarization. The magnitude of this capacitance, which develops between ionic-conducting media and blocking electrodes, directly correlates with charge carrier concentration.

Applying this technique to low alkali (10^{-2} ppm) silica glasses, Tomozawa et al. [36] found an effective charge carrier density of about 10^{12} – 10^{13} cm^{-3}. Similarly, Martin et al. [2] also applied space charge polarization, and found a low effective charge carrier concentration of 100 ppm for $LiPO_3$ and 1000 ppm for $NaPO_3$ glasses at 25 °C. It is worth mentioning that the estimated value of n_t (total number of charge carriers) from Martin’s experiments exceeded by orders of magnitude the theoretical value, which raises the question about possible artifacts in their measurements.

Given that the combined approach of impedance spectroscopy and space charge polarization seems to provide a more direct and simpler method for estimating charge carrier concentrations, this thesis will focus, in chapter 3 and 4, primarily on this technique. Specifically, we will examine interfacial and surface conditions to evaluate experimental parameters and develop a methodology for applying this approach to oxide glass ionic conductors.

2.4 Space Charge Polarization

The increase in permittivity observed in the Au/glass/Au system at low frequencies (<100 Hz) [37–39] is attributed to a phenomenon known as space charge polarization. This type of polarization, also referred to as electrode polarization, arises due to the accumulation of mobile ions at the electrode/electrolyte interface, as illustrated in Figure 2-. Essentially, in the presence of a blocking or partially blocking electrode, a interfacial capacitance, often described as a double-layer capacitance, forms at this interface. In such cases, the electrode capacitance becomes proportional to the concentration of mobile charge carriers in the electrolyte, as shown below.

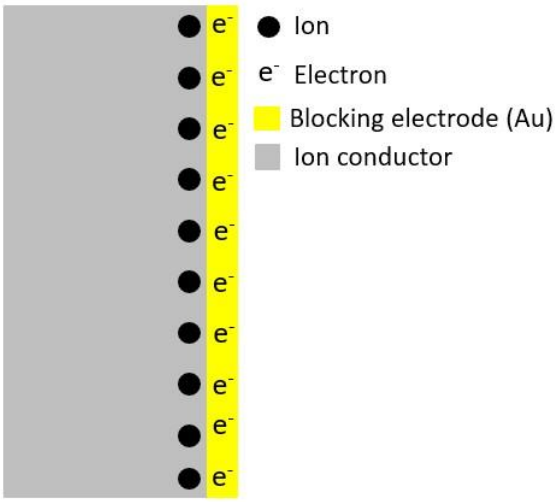

Figure 2-6. Schematic figure of electrode polarization due to the accumulation of charges at the electrolyte (glass)/electrode (Au) interface.

Significant theoretical work has been devoted into developing a theory to understand and describe space charge polarization [35,38–43]. Among these, MacDonald's theory [35] remains the most important reference in the field, originally developed for blocking electrodes. Later, Beaumont & Jacobs [43] proposed a modified theory for partially blocking electrodes, initially applied to KCl crystals. However, it was found that their equations can be used to interpret

and explain what is observed empirically in ionic conducting glasses [2,36,37,44].

Steve Martin et al. [2], using the Beaumont & Jacobs equations [43], presented equations relating the relative permittivity of the double layer (ε_{SC}) to the density of effective charge carriers (n_e [atoms cm^{-3}]). This permittivity (ε_{SC}) is defined at the plateau, at low frequencies, in the graph of the real part of the complex permittivity as a function of frequency, as expressed by equation (8) and illustrated in Figure 2-:

$$\varepsilon_{SC} \equiv \lim_{\omega \to 0} \varepsilon'(\omega) = \varepsilon_\infty + \frac{2L\varepsilon_\infty}{(2+\rho)^2}\sqrt{\frac{n_e e^2}{kT\varepsilon_0\varepsilon_\infty}} \qquad (8),$$

where T is the temperature [K], k is the Boltzmann constant [J K^{-1}], ε_0 is the vacuum permittivity [F m^{-1}], ε_∞ is the relative permittivity at high frequency, ρ is the blocking factor (=0 for blocking electrodes and >0 for partially blocking electrodes) and $\omega = 2\pi f$, where f is the frequency [Hz].

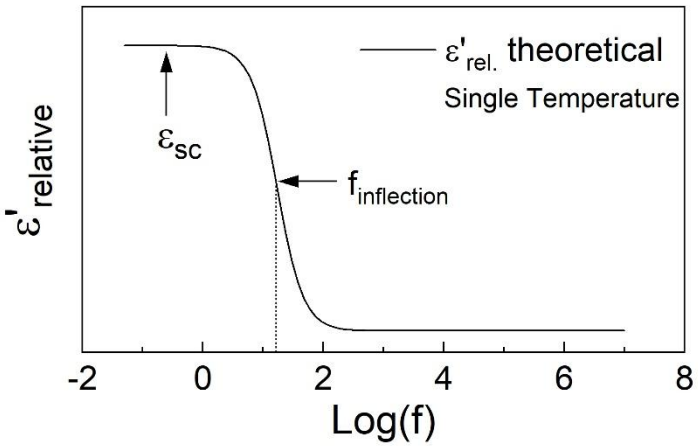

Figure 2-7. Schematic graph of the theoretical curve emphasizing the frequency of the inflection point ($f_{inflection}$) and the permittivity of the double layer formed at low frequencies, from the space charge polarization (ε_{SC}). It is important to note that the numbers in the graph are arbitrary, the main ideas is to illustrated the shape of the curve.

Furthermore, Tomozawa et al. [36,37] also based on the same theory, deduced equations estimating the effective density of charge carriers from the inflection point of the real part of the complex permittivity as a function of frequency, as expressed by equation (5) and also illustrated in Figure 2-:

$$\omega_{inflexão} = \frac{2\sigma_{dc}(2+\rho)}{L\sqrt{\frac{n_e e^2 \varepsilon_0 \varepsilon_\infty}{kT}}} \qquad (9)$$

where σ_{dc} is the frequency independent ionic conductivity [Ω^{-1} cm^{-1}] and e the electron charge [C]. This equation will also be used, and the results will be compared to the results obtained from Equation (8).

CHAPTER 3 – INTERFACIAL CAPACITANCE IN LITHIUM DISILICATE GLASS ELECTROLYTE VIA ELECTRODE POLARIZATION: EFFECT OF EXPERIMENTAL FACTORS AND DETERMINATION OF CHARGE CARRIER DENSITY

Based on a paper published in Journal of American Ceramic Society
https://doi.org/10.1111/jace.20210

3.1 Introduction

Impedance spectroscopy (IS) a widely used technique for probing the electrical properties of materials and their interfaces, particularly in solid electrolytes [45–47]. By analyzing the complex impedance over a broad frequency range, IS enables the separation of different transport processes, ranging from bulk ionic conduction to interfacial phenomena at the electrode/electrolyte contact.

In solid electrolyte systems with blocking electrodes, fast processes such as bulk and grain-boundary ionic conduction take place in the high-frequency to mid-frequency (approx. >1000 Hz; with smaller capacitances $\sim 10^{-12}$ – 10^{-8} F), whereas slower processes associated with electrode polarization and electrical double-layer (EDL) formation appear at low frequencies (approx. <100 Hz [48]; with higher capacitances $\sim 10^{-4}$ F) [49]. As shown in Chapter 2, electrode polarization can provide valuable insights into the density of mobile charge carriers [2,36,37,44], because the resulting electrical double-layer (EDL) formed upon polarization [6,50] is proportional to the effective charge carrier density in the electrolyte [2,36,37,44].

While the EDL is well understood in liquid electrolyte systems [51–54] [55–57], its formation and behavior at solid–solid interfaces remain limited. In such systems, deviations from ideal capacitive behavior are commonly described using a constant phase element (CPE), whose physical origin is still debated. Earlier proposed explanations include purely dimensional-geometric

arguments, attributing deviations from ideality to surface flaws [58], pores [59], scratches, and roughness [60] of the solid electrode. More recently [61–63], physicochemical explanations are related to surface chemistry inhomogeneities or slow ion adsorption on the interface [57,63]. However, systematic investigations of interfacial capacitance in solid electrolytes are scarce and largely limited to earlier studies.

As a result, given the limited publications on the interfacial capacitance formed by solid-state electrolytes and solid metal-blocking electrodes, further research is necessary to advance the development of the field. In this study [64], we have systematically analyzed the influence of a.c. input voltage, surface roughness, polishing medium (mechanical and chemo-mechanical), sample thickness, range of temperature and frequency, and the number of impedance cycles on the interfacial capacitance of lithium disilicate glass sputtered with gold electrodes. Additionally, since the interfacial capacitance is proportional to the number of charge carriers, we explored space charge polarization theory to estimate the effective charge carrier density as a case of study.

3.2 Materials and Methods

3.2.1 Glass synthesis

Lithium disilicate glass (0.33 Li_2O • 0.66 SiO_2) was obtained according to methodology in [64]. Stoichiometric amounts of Li_2CO_3 (Sigma Aldrich, ≥99,0%) and SiO_2 (Vitrovita, ≥99,9%) were homogenized on a rotary jar mill for 6h at 250 rpm. The mixture was melted in a platinum crucible using an electric furnace (Deltech DT-33-RS-812-C) at 1400 °C for 3 h with intermittent, slow, and circular stirring with a silica rod, every hour to remove air bubbles. After the melting time, it was splat cooled, which involves pressing the material between two copper plates to allow a faster cooling rate. The glass was annealed at T_g (glass transition temperature) – 50 °C, for 2 h.

3.2.2 Sample preparation

The samples for impedance spectroscopy analysis were prepared in a parallelepipedal shape with an approximate area of 0.3 cm^2 with thicknesses ranging from 0.32 to 3.56 mm. The geometric factors for each measured sample are compiled in Table 3-1. Different surface treatments were achieved by polishing different samples with sandpaper #600 (SiC), velvet fabric soaked with a diamond suspension of 45 and 9 μm, and a cerium oxide (CeO_2) suspension of 0.5 μm. To assure parallelism between the faces during polishing, the samples were embedded into a homemade device. It is worth mentioning that the use of sandpaper and diamond suspension as polishing media involves a mechanical polishing procedure, whereas cerium oxide is recognized as a chemical mechanical polishing media [65,66]. This experimental variable will also be examined and discussed.

Table 3-1. Geometric factors of the samples used in this work.

Sample		Area [cm^2]	Thickness [cm]	Geometric Factor [cm^{-1}]
a.c. input experiment		0.303	0.112	0.370
Cyclability experiment		0.384	0.101	0.263
Roughness	97 nm	0.262	0.138	0.527
	61 nm	0.262	0.138	0.527
	30 nm	0.262	0.138	0.527
	18 nm	0.303	0.074	0.244

3.2.3 Characterization

The characteristic temperatures of the glass (the glass transition, T_g, and the crystallization peak temperature, T_p) were determined by differential scanning calorimetry (DSC) in air using a DSC-Netzsch 404 equipment at 10 K/min in a platinum crucible with a lid.

The surface roughness was measured by an Olympus LEXT OLS 4000 Confocal Microscope. The parameter chosen in this work to represent the

change in surface roughness is the arithmetic mean height (R_a [μm]) as illustrated in supplementary material Figure S1 and supplementary equation (SE 1). Four lines from three distinct areas were acquired, totaling twelve lines, for each sample. The values reported in this work are the average between these twelve measurements.

Gold electrodes (thickness = 115 nm) were deposited on both parallel sides of the samples using Quorum Q150R ES sputtering. Electrical characterization was carried out in a two-point cell in the air using complex impedance spectroscopy with a Novocontrol Alpha-A High-Performance Frequency Analyzer. From 100 to 280 °C, measurements were taken every 30 °C in the frequency range of 10^7 to 5 x 10^{-2} Hz. We varied the a.c. input voltage from 15 to 300 mV.

3.2.4 Data Analysis

The raw data acquired on the impedance equipment, which is the real (Z') and imaginary (Z'') part of impedance, serves as the initial input. The data was then translated into the permittivity formalism using the relationship shown below:

$$\varepsilon'(\omega) = \frac{-Z''}{\omega\, \varepsilon_0\, [(z')^2 + (z'')^2]}\, \frac{L}{A}, \qquad (1)$$

$$\varepsilon''(\omega) = \frac{Z'}{\omega\, \varepsilon_0\, [(z')^2 + (z'')^2]}\, \frac{L}{A}, \qquad (2)$$

where *L*/*A* is the sample geometric factor, *(L*=thickness, *A*= surface area in contact with the electrode).

Thus, values of ε' will be plotted against frequency, in order to estimate both ε_{dl} and ε_∞, necessary to calculate n_e from equation (8) of Chapter 2. However, since both ε_{dl} and ε_∞ are not clearly identified in the experimental graphs (Figure 3-1b), we also used an equivalent electrical circuit to evaluate the electrode capacitance. In addition, the inflection point, as illustrated in

Figure 1b, was employed to calculate the number of charge carriers (n_e) using equation (2).

3.2.4.1 Calculating the electrode capacitance using an equivalent circuit

In this approach (approach (i)), to estimate the electrode capacitance (C_{dl}), we chose a R//CPE$_{bulk}$-CPE$_{electrode}$ equivalent circuit to fit the impedance data, as shown in the Nyquist diagram of Figure 3-1a. It is important to highlight that Figure 3-1a displays only two temperatures for clarity of the graph. The real part of permittivity as a function of frequency was calculated using equation (3) and is shown in Figure 3-1b. Note that in this approach we limited the frequency range to be fitted by the equivalent circuit because of the absence of a plateau at lower frequencies. A star in both Figure 3-1a and b show the lower limiting frequency. How this limiting frequency was estimated will be explained later in the text.

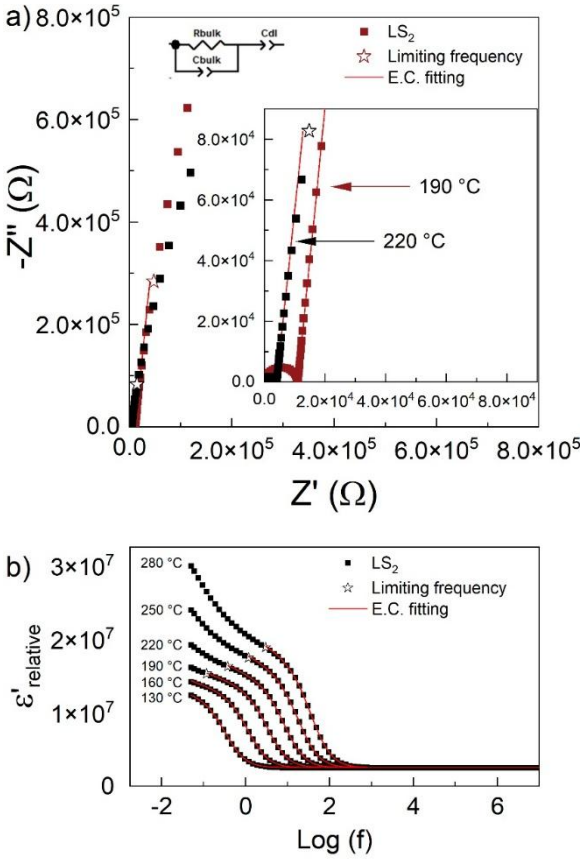

Figure 3-1. (a) Complex impedance diagram and (b) permittivity as a function of log(f) for experimental values obtained in this work for lithium disilicate glass with a surface roughness of 18 nm at various temperatures and the simulated model (R//CPE-CPE) illustrating the lower limiting frequency used in the data fit.

Data were fittd using the Zview software, which in the case of a CPE, gives values for the CPE's parameters Q and α. The effective capacitance (C_{eff}) of a CPE may thus be calculated using the following expression [67]:

$$C_{eff} = Q^{\frac{1}{\alpha}} R^{\frac{1-\alpha}{\alpha}}, \qquad (3)$$

where R is the global ohmic resistance (in our case, the bulk glass resistance). Note that, when $\alpha = 1$, the CPE acts as and ideal capacitor, thus $C_{eff} = Q$. To increase the precision, a limiting frequency illustrated in Figure 3-1a and b was chosen to ensure that the errors in the Q and α parameters of the electrode CPE are less than 0.5% and 0.1%, respectively, for all fits.

After estimating the effective capacitance of the electrical double layer (C_{dl}=C_{eff}), its permittivity (ε_{dl}) was calculated using the expression (4).

$$\varepsilon_{dl} = \frac{C_{dl}}{\varepsilon_0}\frac{L}{A} \qquad (4)$$

Thus, the number of effective charge carrier (n_e) may be estimated using equation (8) of Chapter 2, where the blocking factor ρ was considered 0 since gold electrode ideally acts as a blocking electrode.

3.2.4.2 Using the inflection frequency to calculate n_e

This approach (approach (ii) considers the inflection frequency of the ε' vs log (f) graph, as demonstrated by Tomozawa et al. [36,37]. As shown in equation (2), the inflection frequency is proportional to n_e and may be used to calculate the effective charge carrier density. This alternate strategy has an advantage over the first one. It can be used without the need for calculating the electrode capacitance and regardless of the presence of a plateau at low or high frequencies. In this approach, one only needs to reach the inflection frequency ($f_{inflection}$), which makes it applicable even at lower temperatures.

The approach (iii) uses the peak frequency of the ε'' vs log(f) graph. This approach is similar to approach (ii) since, in an ideal Debye behavior, the

inflection point also corresponds to the dielectric loss peak [6]. The peak point of the ε'' vs log(f) graph was used as a consistency test. To ensure a higher precision, the inflection and peak frequency from real and imaginary part of complex permittivity were determined by the second and first derivative, respectively. The derivatives were plotted, and the frequency was determined graphically at the intersection with y=0, as illustrated by Figure 3-2 in the supplementary information.

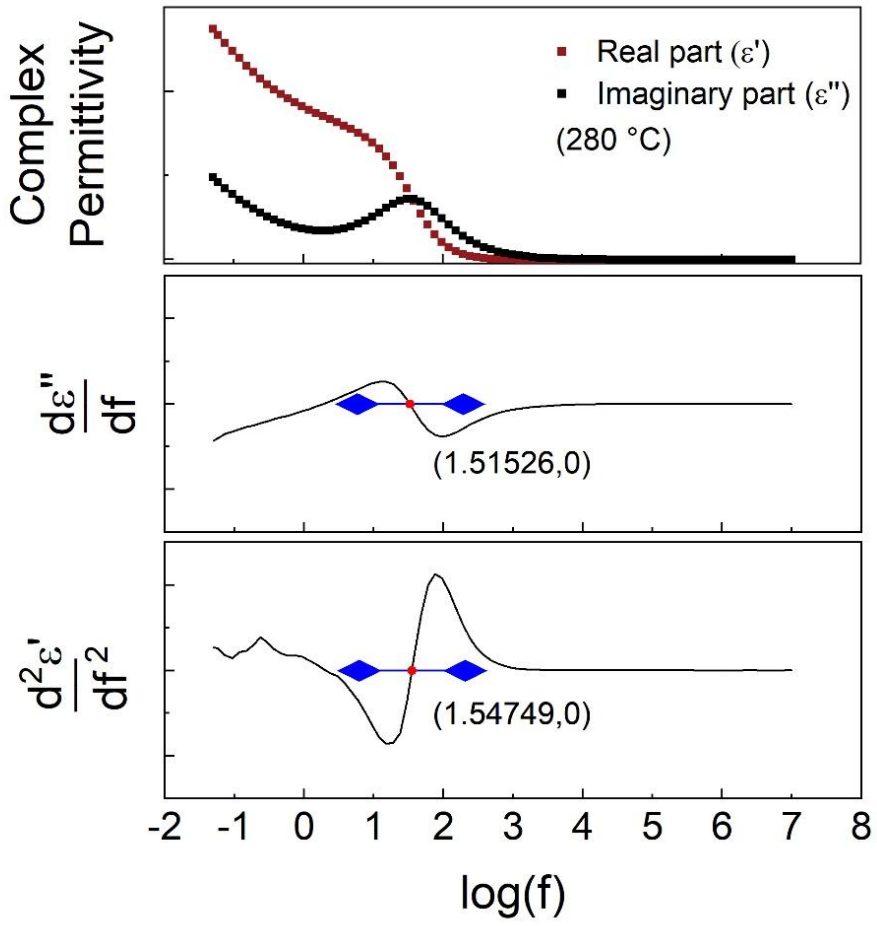

Figure 3-2. Schematics of the method used to determine the inflection and peak frequency from the derivatives.

For all three approaches outlined, the permittivity at high frequency (ε_∞) must be determined. Because of a lack of plateau at high frequency when considering a high-resolution plot, and since this high frequency region is

associated with the bulk capacitance, ε_∞ was determined by estimating the apparent (or geometrical) capacitance of the bulk glass (CPE_{bulk}) using the equivalent circuit model and employing equation (3) and (4).

3.3 Results

3.3.1 Glass thermal characterization

The DSC curve of LS_2 glass is shown in Figure 3-3a. As expected, the profile exhibits a base line change in the endothermic direction corresponding to the glass transition temperature and an exothermic peak resulting from the glass crystallization. The glass transition temperature (T_g = 452 °C) was determined by the intersection method as highlighted in the Figure 3-3a inset, while the crystallization peak is found at 678 °C. These results are comparable with previous reports [68–70]. In addition, Figure 3-3b illustrates a typical XRD pattern of glassy material, with an amorphous halo between 2θ = 15-30°, characteristic of silicate glasses, confirming the glassy state of synthesized LS_2 glass, which is transparent, colorless, and bubble-free.

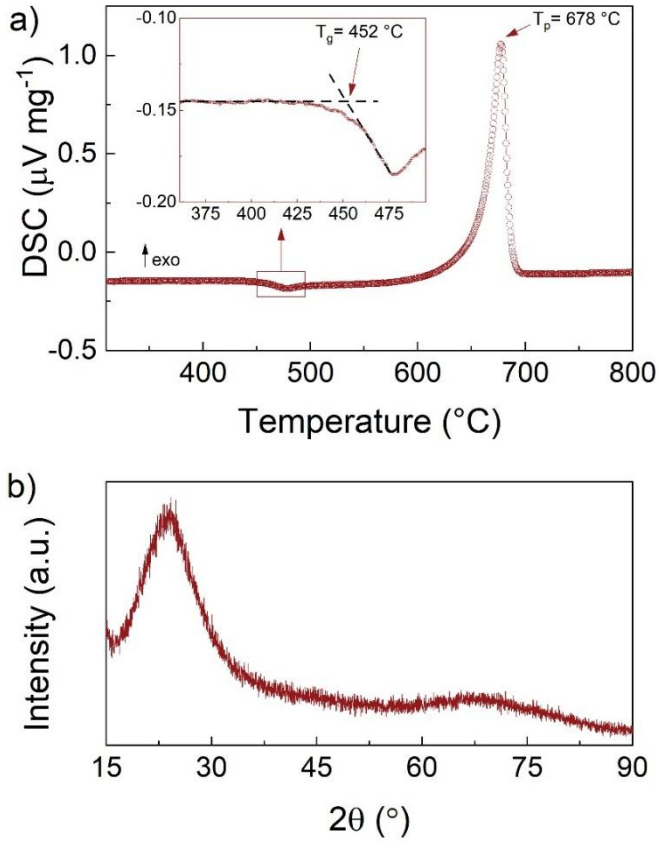

Figure 3-3. Differential scanning calorimetry curve for as quenched LS_2 bulk glass at a heating rate of 10 °C min^{-1}; (b) X-ray diffractogram pattern for LS_2 glass.

3.3.2 Surface roughness characterization

Figure 3-4 illustrates the optical images of the sample's surface for each different polishing treatment. The inset is a 3D image in perspective, highlighting the surface roughness. As can be observed, the reduction of the polishing particles size produces a clear shift in surface roughness. Table 3-2 presents the arithmetic mean height (Ra [µm]) values for the respective surface condition. For the sake of simplicity, hereinafter, we will refer to this surface parameter as surface roughness.

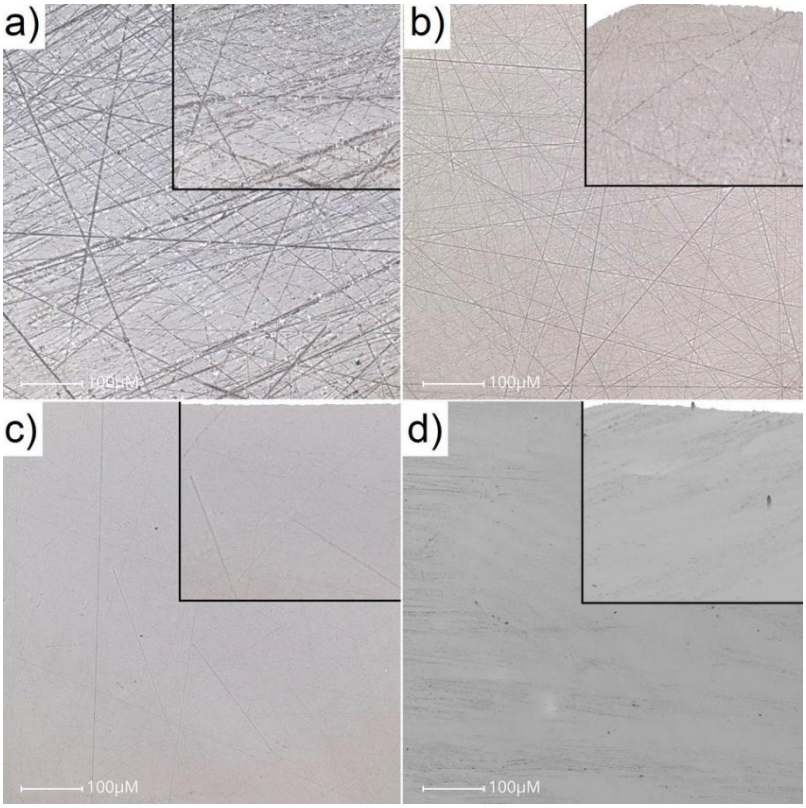

Figure 3-4. Optical images from LS_2 surface after polishing using (a) sandpaper #600; (b) 45 µm diamond solution; (c) 9 µm diamond solution; (c) 0.5 µm cerium oxide solution. The inset are 3D images from the respective surface.

Table 3-2. Arithmetic mean height (R_a) of the surface after treatment. Twelve linear analyses from three distinct locations of each sample were used to calculate the average.

Polishing	Polishing media	Arithmetic mean height [nm]
#600	Sandpaper	97 ± 10
45 μm	Diamond solution	61 ± 29
9 μm	Diamond solution	30 ± 5
0.5 μm	Cerium oxide	18 ± 4

3.3.3 Electrical measurements

Prior to the measurements, approximately 115 nm of gold electrode was sputtered on the samples' two parallel sides as illustrated in Figure 3-5 The ionic conductivity was measured using impedance spectroscopy, and the data was analyzed using complex impedance plots (Nyquist diagrams), permittivity formalism, and Arrhenius plots.

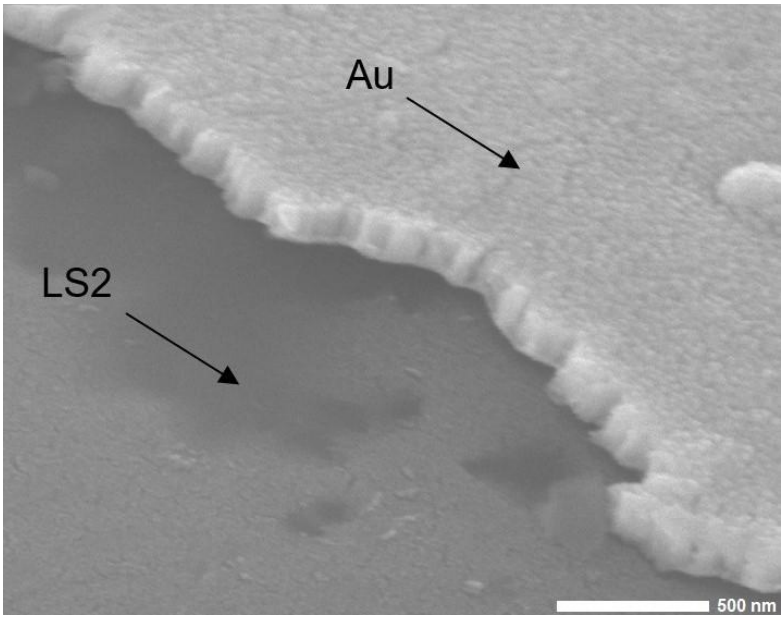

Figure 3-5. Scanning electron microscopy in BSE mode image of the gold electrode (~115 nm) deposited on top of the LS_2 surface by magnetron sputtering.

3.3.3.1 Influence of a.c. input voltage on impedance data

The magnitude of the a.c. input voltage may induce some electrochemical reaction in the samples, detected by a bending of the electrode polarization straight line, which can be associated to the beginning of a semi-circle due to a resistance of charge transfer [49]. Therefore, the influence of this parameter was carefully investigated. Figure 3-6a shows the complex plane plots obtained for gold sputtered lithium disilicate at 100°C using different a.c. input voltages. As can be seen, no appreciable difference between experimental points was detected, that is, the semicircles and the electrode spikes coincide between the different conditions. On the other hand, for measurements conducted at 280 °C (Figure 3-6b), it is seen that the electrode spike begins to bend from applied voltages of 120 mV, signaling a charge transfer resistance due to a potential electrochemical process. However, the semicircle at high frequency remains unchanged, suggesting no alteration in the bulk behavior and glass resistance. As a result, a suitable input voltage for the electrode polarization experiment to minimize potential electrochemical process was determined to be within a range of 15 to 60 mV. To maximize the sample signal, we conducted the experiment at a voltage of 60 mV.

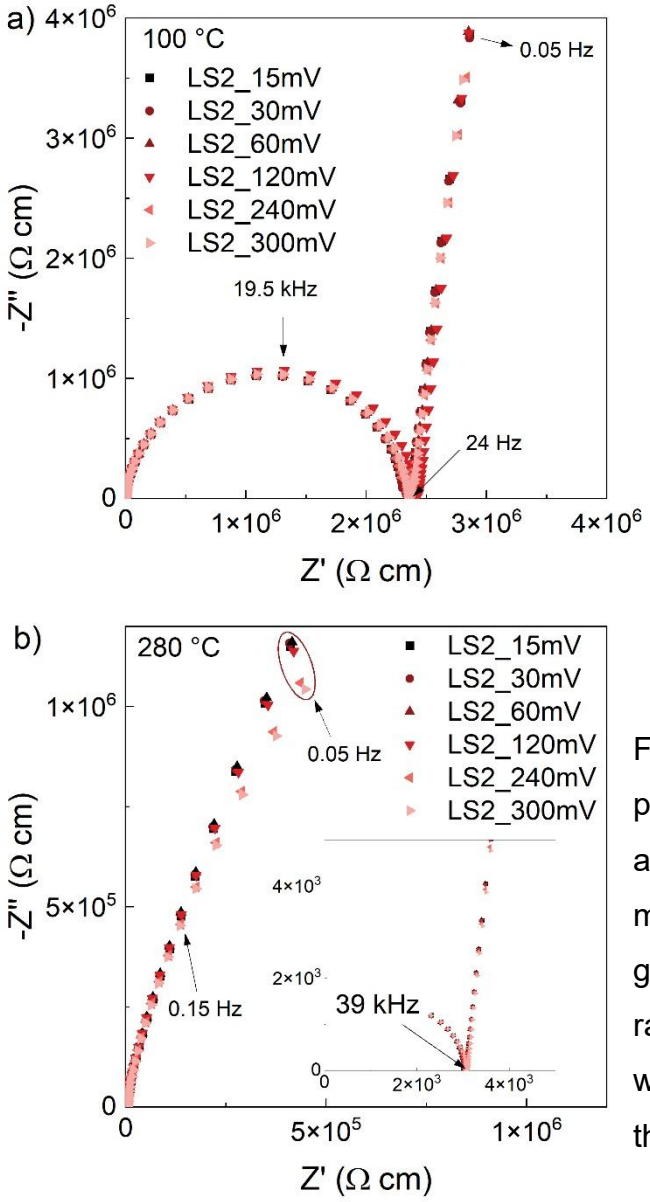

Figure 3-6. Complex impedance plane of LS_2 data (gold electrodes) at (a) 100 °C and (b) 280 °C. The measurements were performed at gradually increasing voltages ranging from 15 mV to 300 mV without removing the sample from the instrument.

3.3.3.2 Influence of cycles on impedance data

To test the data reproducibility, the sample were submitted to several measurement cycles. Each cycle consisted in taking data from 100 °C to 280 °C (with 30 °C increments) in the frequency range of 1 x 10^7 to 5 x 10^{-2} Hz. Figure 3-7 illustrates the first four cycles taken 2 hours apart between them without removing the sample from the instrument. It is observed that the electrode polarization spike of the first cycle differs from the following cycles. However,

from the second cycle onwards, the experimental points on the electrode polarization are reproducible. Additionally, it can be stated that the electrode exhibited a more ideal behavior in the second cycle, that is, the angle increases to near 90°, indicating a value closer to 1 for CPE's parameter α. The sample's resistivity between cycles varies less than 1.5% (see inset), which lies in the experimental error of the impedance technique [71].

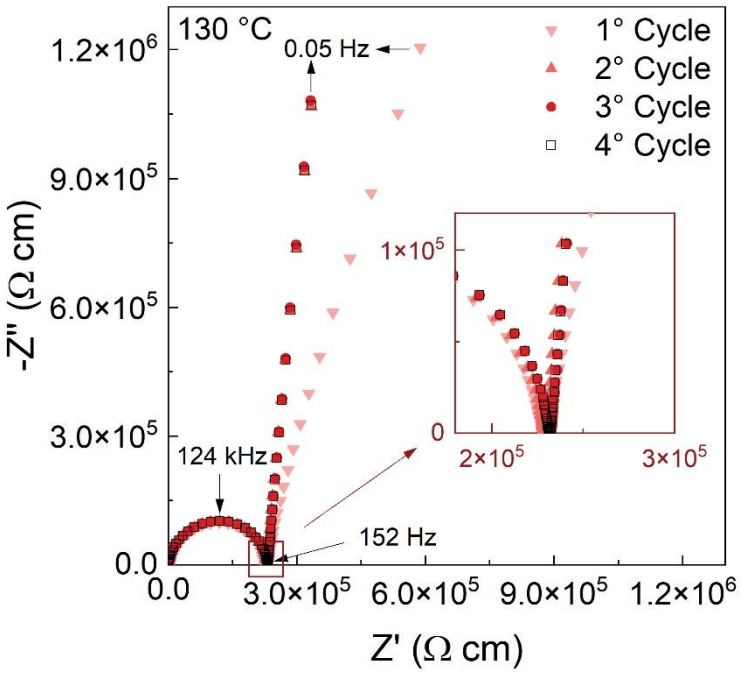

Figure 3-7. Nyquist plot for four measurement cycles (60mV applied voltage) of LS_2 glass sample with gold electrode. The measurements were done without removing the sample from the equipment and 2 hours apart between cycles.

Regarding the distinction between the first and second cycles, the change is also evident in both the real and imaginary components of the complex permittivity, as depicted in Figure 3-8a,b for the first cycle and Figure 3-8c,d for the second cycle. Concerning the real part of the complex permittivity (ε'), noticeable trends emerge from the second cycle onwards, that is, consistent regular spacing between the curves of different temperatures, particularly for frequencies lower than 100 Hz. For instance, during the first cycle, there is a more substantial gap between the curves at 190 °C and 220 °C

– when compared to the interval between other consecutive temperatures, along with a merging of curves at 250 °C and 280 °C – a phenomenon not observed on the second cycle. Similar trends are evident in the imaginary part of the complex permittivity (ε''), that is, for the first cycle (Figure 3-8b) there is a larger leap in the peak value from 190 °C to 220 °C, as well as a relatively similar peak value for 250 °C and 280 °C – which is analogous to the merging curve in the real part (Figure 3-8a). In this way, starting from the second cycle (Figure 3-8c,d), there is a gradual, and regular increase in the values of both, real and imaginary part of complex permittivity, with rising temperature. Consequently, all the results presented in this study are from the second cycle, where data on the electrode spike become reproducible. Additionally, Figure 3-9 in encompasses all cycles and temperatures in a single figure for comparison. Nevertheless, the change in the full spectrum of electrode polarization from the first to the second cycle is still under discussion.

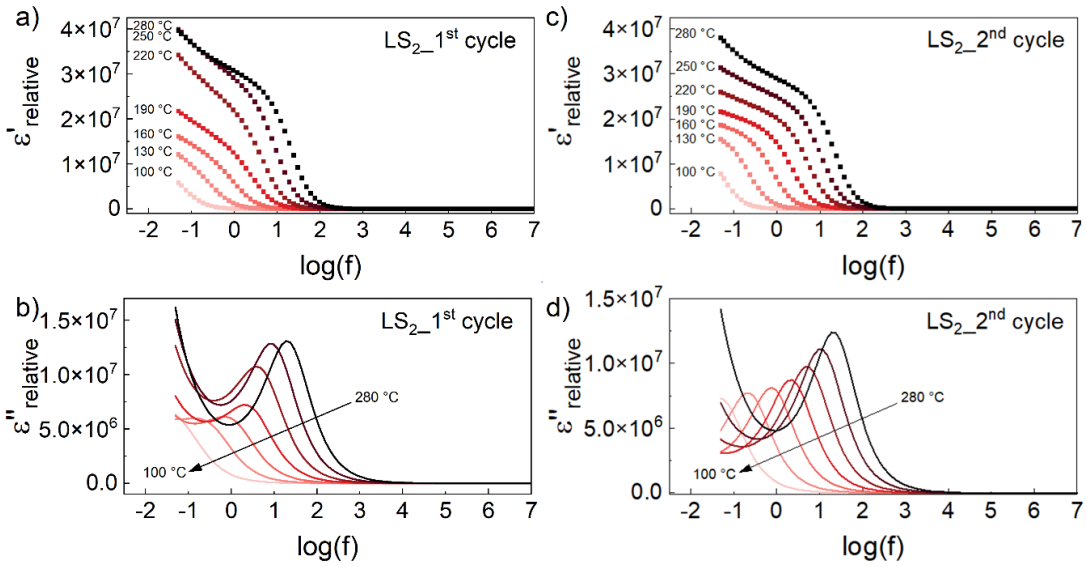

Figure 3-8. (a) real and (b) imaginary part of complex permittivity as a function of log(f) for the 1st measurement cycle of LS_2 sample with gold electrode; (c) and (d) represent the real and imaginary part for the 2nd measurement, respectively. To enhance clarity, the imaginary part was depicted as a "line" rather than using "dots". This was done to prevent overcrowding, facilitating the clear visualization of the differences discussed in the text.

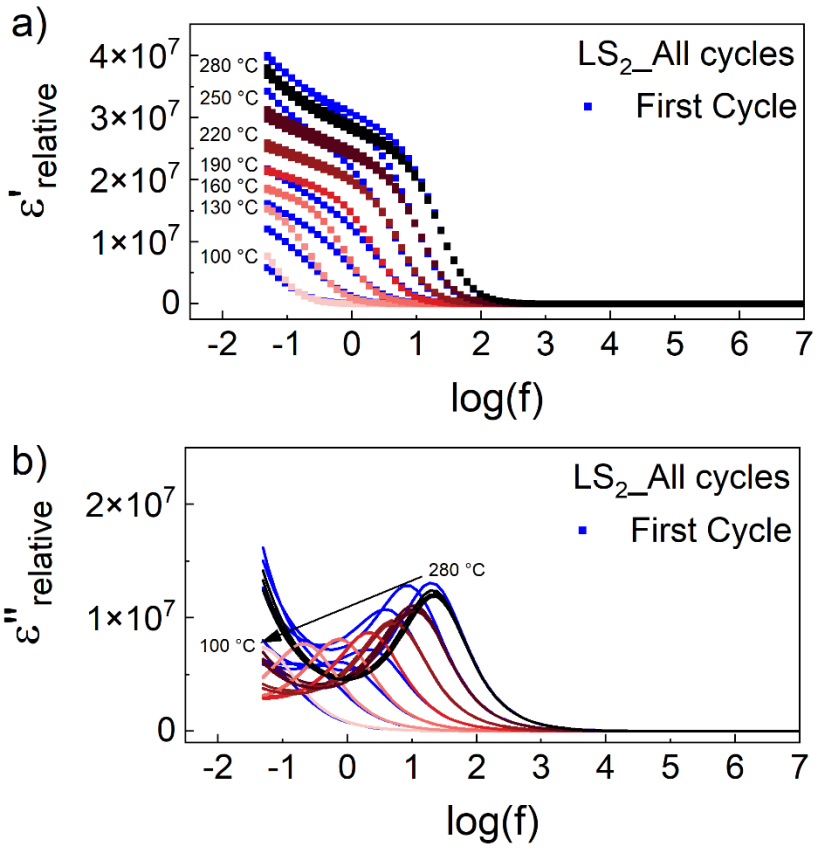

Figure 3-9. (a) real and (b) imaginary part of complex permittivity as a function of log(f) for the 1st, 2nd, 3rd, and 4th measurements cycles of LS_2 sample with gold electrodes. The data from the 1st cycle are shown in blue, while those from the 2nd cycle onward are shown in shades of red. For each temperature, the shades of red are overlaid, that is, not so differentiable because of the similarity of the data.

3.3.3.3 Influence of surface roughness on interfacial capacitance

Another experimental variable tested in this study is the surface roughness. The Nyquist diagrams obtained for LS_2 with all surface roughness values shown in Table 3-1 are illustrated in Figure 3-10. It can be observed that the angle of the electrode spike increases as surface roughness decreases, which aligns with expectations, as a more polished surface is closer to the ideal behavior with an angle of 90° ($\alpha\ parameter \approx 1$). This is further confirmed when analyzing the α parameter from the equivalent circuit fit, equal to 0.86, 0.88,

0.90 and 0.92 for the arithmetic mean height (Ra) 97, 61, 30 and 18 nm, respectively.

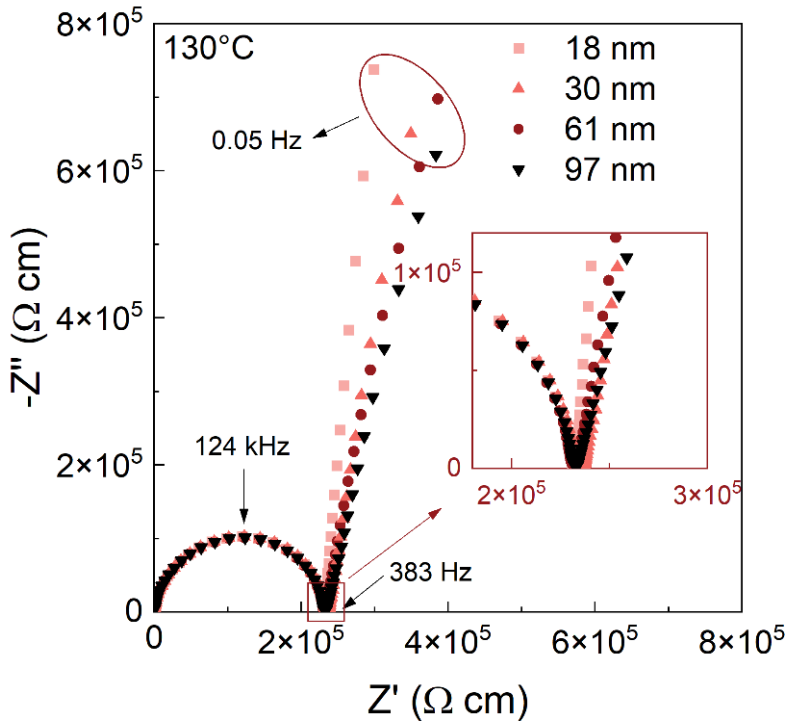

Figure 3-10. Nyquist plot of LS_2 glass with gold electrode and different surface roughness, measurements with two points electrodes, in air.

Furthermore, Figure 3-11 a and b show the specific interfacial capacitance for each surface condition. Figure 3-11a depicts the specific interfacial capacitance values estimated at the limiting frequency calculated using equations (1) and (4), while in Figure 3-11b the values were estimated by the equivalent circuit approach (i). In both cases, it is observed that surface roughness has a minor impact on specific capacitance values when the surface is mechanically polished with diamond suspension. In fact, the specific interfacial capacitance values for the sample surfaces with roughness values of 97 nm, 61 nm, and 30 nm are quite comparable. In contrast, the chemical-mechanical polishing using cerium oxide (with a roughness of 18 nm) exhibited specific interfacial capacitance values approximately two to three times lower when compared to those obtained by mechanical polishing, despite the

electrode spike exhibiting behavior closest to the ideal. In the same way, the equivalent circuit (Figure 3-11b) approach also estimates a specific interfacial capacitance approximately one order of magnitude lower than that calculated in Figure 3-11a, exhibiting the same pattern, that is, samples mechanically polished display specific capacitance values two to four times higher when compared to those obtained by chemo-mechanical polishing.

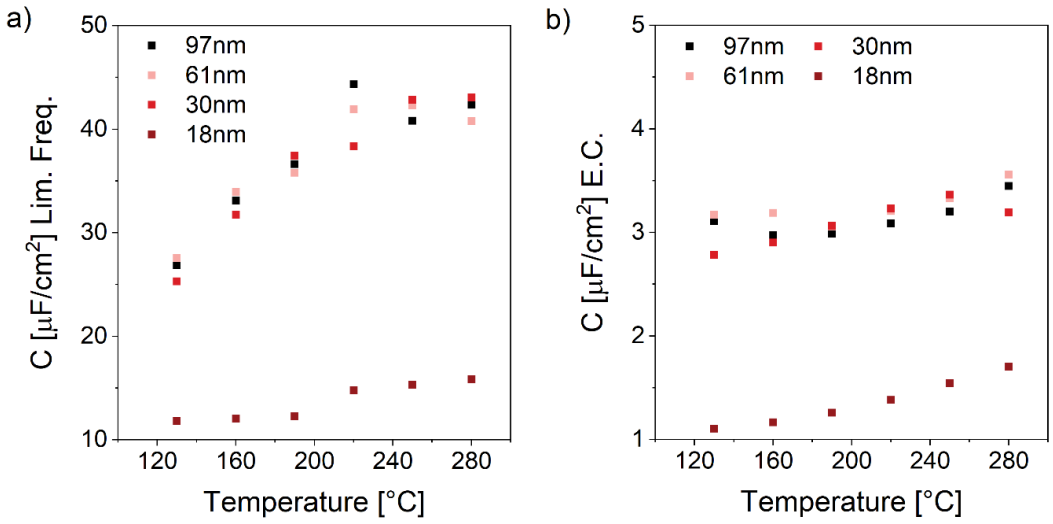

Figure 3-11. Interfacial specific capacitance as a function of surface treatment and roughness measured (a) at the limiting frequency and (b) estimated from the equivalent circuit. 18 nm roughness surface was obtained by polishing with CeO_2.

The difference in interfacial capacitance observed in Figure 3-11 between the mechanical and the chemical-mechanical treatment can be explained by the presence of cerium on the glass surface. Cerium oxide (CeO_2) has been widely employed as a glass polishing agent because it results in high-quality polished surfaces. This is a result of combining mechanical and chemical polishing. While the mechanical part involves purely wear caused by the cerium particles, the chemical is essentially due to the instability of CeO_2 in an aqueous solution, which leads the Ce^{4+} to reduce into Ce^{3+} [65,66], which further involves complex multi-step chemical reactions between ceria particles, water, and silica in lithium disilicate surface [66]. As a result, it can produce smoother surfaces

when compared to a baseline arithmetic mean height (Ra) expected for the cerium oxide particle size alone. However, the most important aspect is that cerium can be detected on the surface of silica-based glasses [72,73], and depending on the polishing procedure, can range from 10 nm up to 8 μm depth. Therefore, one can assume that the presence of cerium on the surface led to the interfacial capacitance values two to three times lower than the treatment with SiC sandpaper and diamond solution, as seen in Figure 3-9 and Figure 3-10c and d. Comprehensive investigations into the mechanisms responsible for the impact of cerium (Ce) inclusions on interfacial capacitance would undoubtedly be of great interest to the glass community. However, it remains outside the scope of this study; their precise nature is yet to be fully elucidated

3.3.3.4 Calculating the effective number of charge carriers (n_e)

As previously discussed, approach (i) focuses on a set of frequencies, while approach (ii) and (iii) examine the inflection and peak frequency of the complex permittivity related to space charge polarization, respectively. Table 3-3 summarizes all the variables defined in this work, such as the limiting frequency ($f_{limiting}$) of the equivalent circuit, inflection ($f_{inflection}$) and peak (f_{peak}) frequencies determined through derivatives, bulk permittivity (ε_∞), electrical double layer permittivity (ε_{dl}) and capacitance (C_{dl}) calculated at the limiting frequency. In this way, the effect of the experimental variables on the interfacial capacitance and the estimation of effective charge carriers will be discussed.

Table 3-3. Values of limiting frequency ($f_{limiting}$) of equivalent circuit, inflection ($f_{inflection}$) and peak (f_{peak}) frequencies determined through derivatives, bulk permittivity (ε_∞), electric double layer permittivity (ε_{dl}) and capacitance (C_{dl}) estimated at the limiting frequency determined in this work for all samples.

Sample	Temperature [°C]	$f_{limiting}$ [Hz]	$f_{inflectio}$ [Hz]	f_{peak} [Hz]	ε_∞ relative	ε_{dl} relative	C_{dl} [F]

97 nm	130	-	0.1141	0.0822	56	4.846E+07	8.146E-06
	160	0.0934	0.4031	0.3177	56	4.638E+07	7.796E-06
	190	0.1868	1.2668	0.9915	55	4.660E+07	7.834E-06
	220	0.1868	3.5400	2.8694	54	4.811E+07	8.087E-06
	250	0.7476	8.4898	7.2627	53	4.992E+07	8.391E-06
	280	1.4956	18.34	16.3606	51	5.374E+07	9.034E-06
61 nm	130	-	0.1264	0.1064	57	4.944E+07	8.311E-06
	160	0.0934	0.4107	0.3277	57	4.973E+07	8.360E-06
	190	0.1868	1.3555	1.1784	56	4.762E+07	8.004E-06
	220	0.23542	3.6241	3.0981	55	4.999E+07	8.404E-06
	250	0.59336	9.139	8.0556	54	5.193E+07	8.730E-06
	280	1.8844	18.9365	17.697	51	5.546E+07	9.324E-06
30 nm	130	-	0.1356	0.10287	56	4.340E+07	7.296E-06
	160	0.0934	0.4784	0.4079	56	4.522E+07	7.601E-06
	190	0.1483	1.3673	1.2064	56	4.775E+07	8.028E-06
	220	0.4709	3.4300	3.0406	55	5.040E+07	8.472E-06
	250	0.7476	7.7922	6.7959	54	5.246E+07	8.819E-06
	280	1.8844	17.6339	15.0865	51	4.977E+07	8.367E-06
18 nm	130	-	0.324	0.303	33	9.249E+06	3.352E-06

160	0.23542	1.127	1.07	32	9.750E+06	3.534E-06
190	0.94202	3.281	3.09	32	1.053E+07	3.815E-06
220	1.1869	8.185	7.709	32	1.156E+07	4.189E-06
250	7.5404	17.66	16.481	31	1.291E+07	4.680E-06
280	23.947	35.237	32.734	31	1.425E+07	5.164E-06

In approach (i), we used the electrode capacitance values, estimated by an equivalent circuit and a limiting frequency, to calculate the effective number of charge carriers, using equations (3) and (4), and equation (8) of Chapter 2. Equation (8) of Chapter 2 were applied to the capacitance values (Figure 3-11) obtained for samples with different roughness. Results are shown in Figure 3-12.

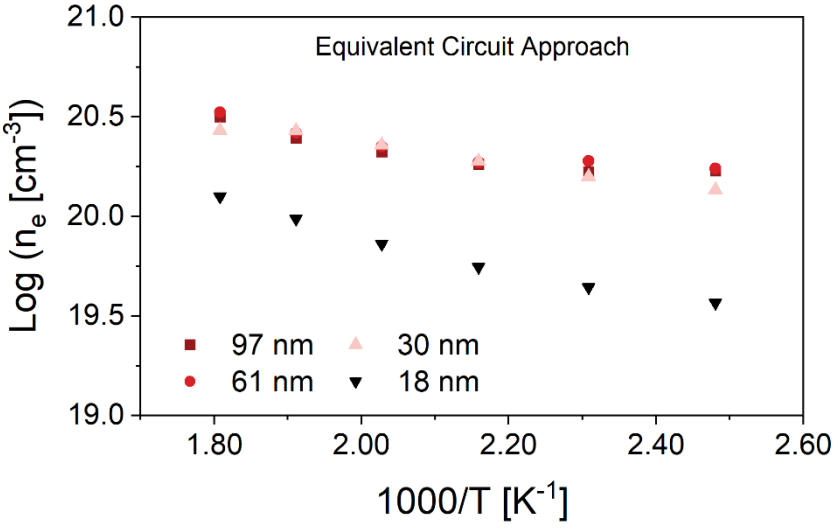

Figure 3-12. Number of effective charge carriers calculated based on the interfacial capacitance estimated through equivalent circuit for different surface treatment. 18 nm roughness surface was obtained by polishing with CeO_2.

Figure 3-12 shows that the influence of surface treatment is also reflected in the estimated number of effective charge carriers, as expected. Similar behavior to the capacitance results can be noted, i.e., the number of effective charge carriers is comparable for different roughness obtained by mechanical polishing (97, 61, and 30 nm). In contrast, samples submitted to the chemical-mechanical polishing (18 nm) of cerium oxide exhibited values around half an order of magnitude lower. This difference is attributed to the lower values of interfacial capacitance measured due to the presence of cerium in the surface as discussed hereinbefore.

As evidenced by the absence of a clear plateau at the low frequencies (Figure 3-1b), the formation of the EDL is frequency-dependent, making the exact determination of its capacitance uncertain. The strategy to employ equivalent circuits and use a set of data to estimate the interfacial capacitance has potential, however, the capacitance estimated by the equivalent circuit is around 10 times lower (Figure 3-11) than that calculated through permittivity measurements at a fixed limiting frequency.

In this way, to avoid discrepancies in capacitance values, in approach (ii) we calculated the effective number of charge carriers by employing a strategy described by Tomozawa et al. [36,37], using the inflection frequency ($f_{inflection}$) of the ε' log (f) graph illustrated in Figure 2-. Since the measurements were taken in a range of 130 – 280 °C, it is possible to calculate the number density of charge carrier, n_e, at different temperatures. Thus, the evolution of n_e with the temperature can be exhibited in an Arrhenius plot, as illustrated by Figure 3-13. For comparison, Figure 3-13 shows the Arrhenius plot of n_e calculated from capacitance values (equations (3) and (4), and equation (8) of Chapter 2), and from the inflection point and peak frequency (equation (9)) for different surface roughness. The activation energy calculated by the slope of the Arrhenius plot of n_e, (Figure 3-13) may be ascribed to the activation energy of charge carrier formation [2]. For comparison, the Arrhenius plot of ionic conductivity is shown in the same figures.

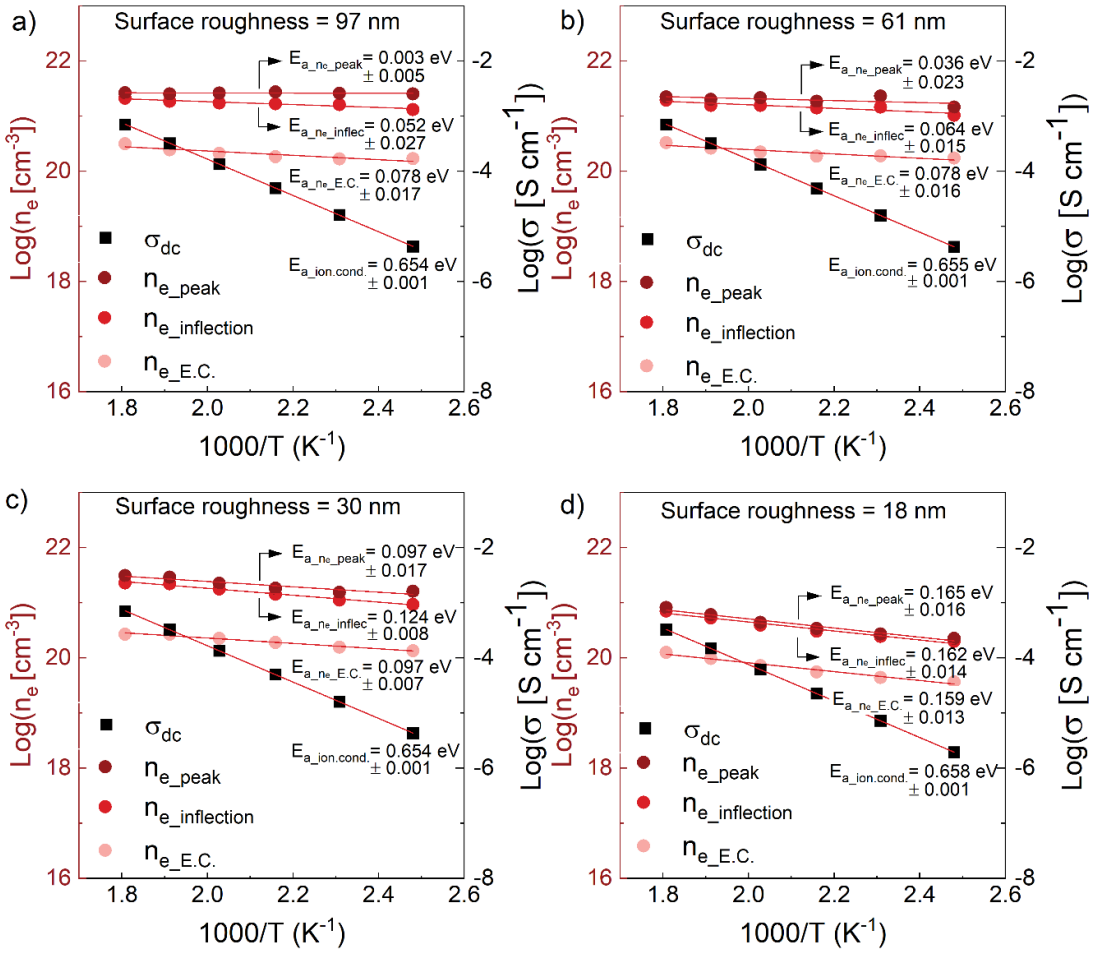

Figure 3-13. Arrhenius plot for LS_2 glass with surface roughness a) 97 nm; b) 61 nm; c) 30 nm; d) 18 nm (polishing with cerium oxide). The conductivity is represented in black while the charge carrier density is shown in hues of red. The effective charge carrier density was calculated from equivalent circuit fit (E.C.), inflection, and peak frequency of complex permittivity, as indicated.

Figure 3-13 shows that all n_e values obtained with mechanical polishing remain in the same order of magnitude (~10^{21} at_{Li^+} cm^{-3}), if compared to values obtained by CeO_2 polishing (Figure 3-13d), which are one order of magnitude lower (~10^{20} at_{Li^+} cm^{-3}). It is worth mentioning that the activation energy due to the charge carrier formation increases from 0.052 to 0.165 eV with decreasing surface roughness. This means that the temperature affects more the measured capacitance, and thus, n_e , when samples have smaller roughness (R_a). On the

other hand, the overall activation energy from ionic conductivity is not affected by surface roughness, remaining constant at 0.65 eV, consistent with previously published values for lithium disilicate glass [49–51].

Moreover, a careful evaluation of Figure 3-13, which provides the activation energy along with the inaccuracies, reveals low relative errors in the activation energy, such as for surface roughness of 30 and 18 nm (error as low as 6.5%). However, when surface roughness is 97 nm, this error is larger than the result itself (error >100%), as in the case of n_e calculated by the peak frequency (Figure 3-13a). As a result, samples with higher surface roughness do not yield similar activation energy values within acceptable error for all three approaches. Thus, a minimum surface roughness of 30 nm should be achieved when the space charge polarization method is employed to estimate the number of effective charge carriers in lithium disilicate glasses. Additionally, despite excellent surface roughness (Ra) produced by the CeO_2 (18 nm) and activation energy agreement between all three approaches (Figure 3-13d), it produced an activation energy error larger than that observed in the 30 nm sample. This large error is attributed to the presence of Ce as discussed earlier.

Another important finding worth emphasizing is the experimental estimation of the total number of charge carriers (n_t). According to the fittings in Figure 3-13, the total number of charge carrier (n_t) can be estimated at the intersection of the curve with the log (n_e) axis when 1000/T tends to zero. For the inflection frequency approach of 30 nm roughness (Figure 3-13c), the total number of charge carriers ($n_{t\_inflection}$) is 3.23 x 10^{22} [at_{Li^+} cm^{-3}], which notably matches the theoretical value calculated through density ($n_t = \frac{d_{LS2}N_A}{MM_{LS2}}$, where d_{LS2} and MM_{LS2} is the lithium disilicate density and molar mass, and N_A is the avogrado number) measurements (1.92 x 10^{22} [at_{Li^+} cm^{-3}]). On the other hand, the equivalent circuit approach estimation of $n_{t\_E.C.}$ is about an order of magnitude lower, at 2.13 x 10^{21} [at_{Li^+} cm^{-3}], which reflects the lower capacitance values estimated through this method.

In summary, the optimal condition for measuring ne in lithium disilicate glass may be achieved by taking data measured at a second impedance cycle, 60 mV as applied voltage, temperature between 130 and 280 °C, and a

frequency range from 10^7 to 5 x 10^{-2} Hz. The sample should be treated by mechanical polishing (minimum 9 nm diamond suspension soaked in velvet fabric – Ra ≤ 30 nm). The effective number of charge carriers should be estimated using the inflection frequency, as described by Equation (2). In these conditions, it is demonstrated that the ratio $\frac{n_e}{n_t}$ is in the range of 5 to 12% (between 130 and 280 °C). At the same time, the activation energy of charger carrier formation is 0.124 eV, which corresponds to about 20% of the overall activation energy related to the ionic conduction process (0.655 eV). Extrapolating the linear fit to lower temperatures, the fraction $\frac{n_e}{n_t}$ is 1% at 25 °C, which means that, at a certain time, a fraction of 1% of the charge carriers participate on the ionic conductivity. Almond, Duncan, and West [30] estimated the percentage of effective charge carriers for an $Ag_7I_4AsO_4$ glass and K/Ca nitrate glass, being 1.1% and 0.1%, respectively. It is worth mentioning that data collected for $Ag_7I_4AsO_4$ glass is in cryogenic temperatures. In the same way, A.K. Landry et al. [74], found that this ratio is around 0.1% for LIPON amorphous electrolyte. Finally, it is worth mentioning that the estimated value of n_t from the linear fit of this work is consistent with that calculated by density, which validates both, the model and the methodology applied

3.4 Conclusion

The effect of surface treatment applied voltage and number of impedance cycles on the frequency-dependent formation of interfacial capacitance due to electrode polarization at the solid-solid lithium disilicate glass/gold electrode interface was systematically examined in this work. First, an input voltage of 60 mV proved suitable for minimizing potential electrochemical processes during electrode polarization experiments. Secondly, reproducibility in electrode polarization data was achieved from the second impedance cycle onward. Additionally, our results indicated that smoother surfaces closely approximate ideal electrode spike behavior, while surface roughness had a minor impact on capacitance values when mechanically polished with diamond suspension.

Conversely, chemical-mechanical polishing using cerium oxide led to interfacial capacitance values approximately two to four times lower. Concerning estimating the number of charge carriers, we employed the inflection frequency of the ε' vs. Log(f) curve to circumvent the frequency-dependent nature of EDL formation. With this strategy, the number of effective charge carriers remained consistent across different roughness levels within mechanical polishing, mirroring the trends observed in capacitance measurements. However, chemical-mechanical polishing with cerium oxide yielded values approximately half an order of magnitude lower. It is worth mentioning that a significant result is the experimental estimation of the total number of charge carriers (n_t), which noticeably agrees with the theoretical value, calculated by density, when using the inflection approach. In this way, under optimal experimental conditions, we established that the ratio $\frac{n_e}{n_t}$ falls within the range of 5 to 12% between 130 and 280 °C and approximately 1% at 25 °C for lithium disilicate glass electrolyte.

CHAPTER 4 – EFFECTIVE CHARGE CARRIER DENSITY AS A FUNCTION OF LITHIUM OXIDE CONCENTRATION

4.1 Introduction

The ionic conductivity in glasses is strongly related to the type and concentration of charge carriers. Figure 2-4 illustrates the dependence of conductivity on alkali oxide content for lithium (a) and sodium (b) silicate glasses. In both cases, an abrupt rise in conductivity occurs at alkali concentrations below 10 mol%, followed by a slower, monotonic increase at higher concentrations. The logarithmic conductivity scale emphasizes non-linear behavior, particularly at low concentrations.

For concentrations below 10 mol%, Varshneya [5] attributes the sharp conductivity to a percolation threshold. Due to liquid phase separation, the formation of lithium-rich droplets occurs, which grow and connect as alkali content increases. These interconnections may create continuous conduction paths, even though direct experimental evidence is limited. Above 10%, Ravaine & Souquet's weak electrolyte theory [75] explains that only a fraction of Li^+ ions act as charge carriers, with mobility largely independent of composition. In this way, the less pronounced increase in conductivity with alkali concentration would be related to the increase in charge carrier concentration.

Research on ionic transport in glass is limited and complex, with no agreement on conduction mechanisms or measurement methods. Building on the findings of Chapter 3, where the effective charge carrier density in lithium disilicate (LS_2) glass was independently determined, Chapter 4 explores how variations in lithium concentration and glass composition affect both carrier density and mobility, motivating further investigation into the factors that govern this fraction.

To this end, a series of lithium-containing glasses — xLi_2O – (1-x) SiO_2 (x = 0.33, 0.40 and 0.50) and yLi_2O – (1-y) P_2O_5 (y = 0.55, 0.60 and 0.645) —

were selected. These compositions enable an analysis of the effects of network connectivity and alkali concentration on ionic transport properties.

4.2 Methodology

4.2.1 Glass Synthesis

Lithium silicate glasses were prepared in 15 g batches, in the same way as described in Chapter 3. Stoichiometric amounts of Li_2CO_3 (Sigma Aldrich, ≥99,0%) and SiO_2 (Vitrovita, ≥99,9%) were homogenized in a high-speed mixer (FlackTek™) for 3 times 3 minutes at 1700 RPM, with 2 minutes interval between cycles. The mixture was melted in a platinum crucible using an electric furnace (Deltech DT-33-RS-812-C) between 1000 and 1400 °C for 3h with intermittent, slow, and circular stirring with a silica rod, every hour to remove air bubbles. After the melting time, the molten glass was splat cooled, which involves pressing the material between two copper plates to allow a faster cooling rate. The glass was annealed at Tg (glass transition temperature) - 50°C, for 2h.

Lithium phosphate glass (y Li_2O – [1–y] P_2O_5, y = 55, 60 and 64.5) was obtained through the melt and quench technique in a 15 g batch. Stoichiometric amounts of Li_2CO_3 (Sigma Aldrich, ≥99,0%) and $NH_4H_2PO_4$ (Sigma Aldrich, 98%) were homogenized in a high-speed mixer (FlackTek™) for 3 times 3 minutes at 1700 RPM, with 2 minutes interval between cycles. The homogenized material was placed in a platinum crucible and heat treated at 800 °C for 1 h using an electric furnace (Deltech DT-33-RS-812-C) to release volatiles such as ammonia, water, and carbon dioxide from the starting reagents. Because at 800 °C, the mixture had already melted and presented low viscosity, the temperature was lowered to 600 °C for another hour to reduce the viscosity and then the melt was splat-cooled between two stainless steel plates. Due to the difficulty to obtain a fully amorphous composition with 50 Li_2O mol% (for SiO_2) and 64.5 Li_2O mol% (for P_2O_5), which tended to exhibit partial crystallization during melt and quench technique, only the transparent glassy fragments were selected for further characterization.

4.2.2 Sample Preparation

The samples for impedance spectroscopy analysis were prepared in a parallelepipedal shape in a room with controlled relative humidity of 30%. Sample were dry polished up to SiC #5000. According to the FEPA (Federation of European Producers of Abrasives) standard 43-2:2017 which establish the standards of grain size for coated abrasives, the D_{50} of P5000 is 5 µm. Compared to our previous work [64], a particle size of 9 µm is enough to assure adequate roughness for interfacial capacitance measurements. To assure parallelism between both faces during polishing, the samples were embedded into a homemade device. After that, gold electrodes were deposited on both parallel sides of the samples using Quorum Q150R ES sputtering.

It is important to note that, unlike in our previous work, a diamond suspension was not employed in this study due to its chemically aggressive interaction with phosphate glass. Instead, dry polishing was selected for both compositions. One of the silicate compositions investigated here was also examined in earlier work using diamond suspension. By subjecting the same composition to dry polishing in this work, we enable a direct comparison between the two polishing methods, thus validating the polishing method.

4.2.3 Glass Characterization

The characteristic temperatures of the glass (the glass transition, Tg, and the crystallization peak temperature, Tp) were determined by differential scanning calorimetry (DSC) in air using a DSC-Netzsch 404 equipment at 10 K/min in a platinum crucible with a lid.

Electrical characterization was carried out in a two-point cell in the air using complex impedance spectroscopy with a Novocontrol Alpha-A High-Performance Frequency Analyzer. Measurements were taken in the frequency range of 10^7 to 5 x 10^{-2} Hz at a.c. input voltage of 60 mV. As demonstrated in the previous chapter, the reproducibility of space charge formation is achieved

from the second cycle onwards, as a result, all the measurements presented in this chapter are from the second cycle.

Ionic conductivity was obtained from the resistance at the intercept of the semicircle with real-axis from the Nyquist plot, combined with the sample geometry listed in Table 4-1, using Equation (1) as follows:

$$\sigma_{d.c.} = \frac{1}{R_{bulk}} \frac{L}{A} \quad (1)$$

where σ_{dc} is the ionic conductivity of the sample (S cm^{-1}), L is the thickness and A is the area of the sample, whose area was fully coated with gold electrodes.

Because of the difference in ionic conductivity across the different compositions and to maintain the same range of frequency for all composition, enabling measurements in the same time scale, different temperature range were employed for each composition as shown in Table 4-1. The lower value represents the temperature at which the inflection frequency (see chapter 3) can be reached, and the upper temperature represents the maximum temperature to avoid loss of charge carrier due combination due to possible electrochemical reaction in electrode interface polarization (see chapter 3).

Table 4-1. Sample geometry and temperature windows for impedance analysis. To keep spectra in the same frequency/time range despite differing ionic conductivities, measurement temperatures were adjusted for each composition.

Composition [%mol]	Area [cm^2]	Thickness [cm]	Geometric Factor [cm^{-1}]	Temperature Range [°C]
33 Li_2O – 67 SiO_2	0.29	0.09	0.32	160 – 250
40 Li_2O – 60 SiO_2	0.42	0.09	0.21	130 – 250
50 Li_2O – 50 SiO_2	0.10	0.05	0.54	100 – 180
55 Li_2O – 50 P_2O_5	0.35	0.10	0.27	120 – 200
60 Li_2O – 60 P_2O_5	0.39	0.09	0.22	100 – 180
64.5 Li_2O – 35.5 P_2O_5	0.23	0.06	0.27	60 - 110

4.2.4 Ideal versus Non-ideal Behavior

To better expose and comment on our results, it is convenient to differentiate an ideal from a non-ideal behavior of electrode polarization. Figure 1 presents simulated data of Nyquist plot (Figure 4-1a) and Complex permittivity (Figure 4-1b), where the ideal behavior (black symbols) is defined by three main characteristics, as follows: i) the electrode spike in Nyquist plot (Figure 4-1a) exhibits an straight, vertical line forming 90° angle with the real axis. ii) on the real part of complex permittivity (Figure 4-1b) there is a frequency-independent plateau at lower frequencies corresponding to the space charge polarization. iii) the imaginary part of complex permittivity yields a symmetrical, bell-shaped, peak (Figure 4-1b) whose maximum coincides with the inflection point of ε'.

Figure 4-1 shows the change in the graphs when deviation of ideality occurs, where the non-ideal behavior is often represented by a constant-phase element (CPE), as represented by the equivalent circuit. The CPE is defined by two parameters: the coefficient Q and an exponent α, where α quantifies the non-ideality. As α tends to 1, the response approaches that of an ideal capacitor. This can also be seen in the Equation (2) below that estimates the effective capacitance (C_{eff}) of a CPE [67]. Note that, when $\alpha = 1$, the CPE acts as an ideal capacitor, thus $C_{eff} = Q$.

$$C_{eff} = Q^{\frac{1}{\alpha}} R^{\frac{1-\alpha}{\alpha}}, \qquad (2)$$

where R is the global ohmic resistance (in our case, the bulk glass resistance). To show the effect of non-ideality, Figure 4-1 displays simulations (geometric factor 0.21 cm^{-1}) in which the electrode CPE exponent α varies from 1.0 to 0.8 while glass bulk resistance, glass bulk capacitance and the coefficient Q of electrode's CPE are held constant. All three characteristics of ideality are affected. For instance, on Nyquist plot this deviation is translated as an inclination of the spike rather than a perfect vertical line, forming angles smaller than 90° with the real axis. Lowering the α parameter (and increasing the non-ideality), the real part of complex permittivity (Figure 4-1b) no longer exhibits a perfectly flat low-frequency plateau; instead, its magnitude becomes frequency-dependent. Additionally, the imaginary part evolves from a symmetric, bell-

shaped peak, to a broader, asymmetric and shallow shape. With still lower α values the broader bell-shaped curve evolves and the imaginary part starts to increase at lower frequencies.

Table 4-2 shows all parameters used to simulate Figure 4-1.

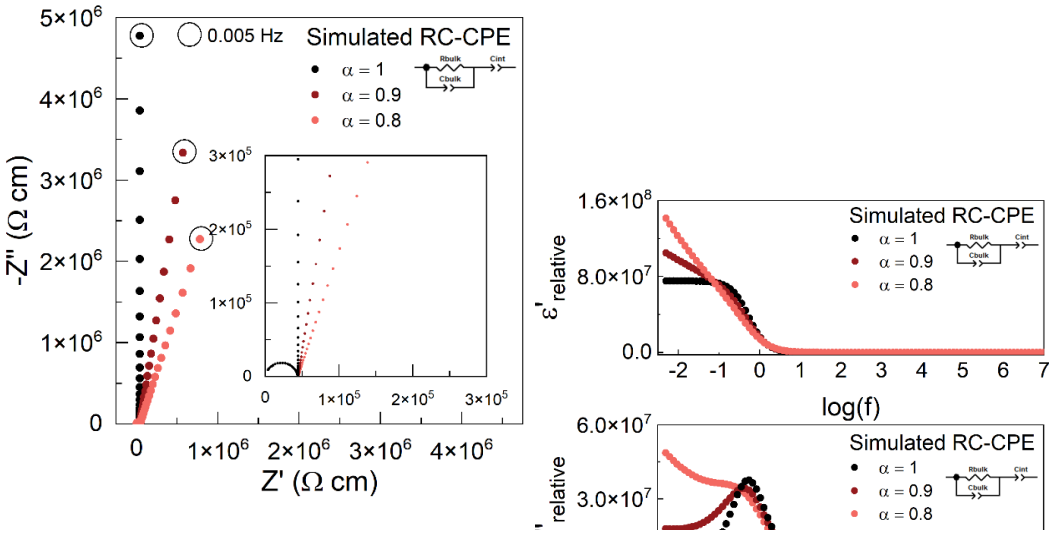

Figure 4-1. (a) Nyquist plot and (b) Complex Permittivity for a simulated $(R_{bulk} \parallel CPE_{bulk})$ – $CPE_{interface}$ equivalent circuit. $R_{bulk} \parallel CPE_{bulk}$ and $Q_{interface}$ were held constant while for the CPE representing the gold electrode, the exponent α is varied from 1.0 to 0.8. Geometric factor is 0.21 cm^{-1}.

Table 4-2. Equivalent circuit parameters used in the simulations of Figure 1. The model is $(R_{bulk} \parallel CPE_{bulk})$ – $CPE_{interface}$, where R_{bulk} and CPE_{bulk} are bulk resistance and capacitance, and $CPE_{interface}$ represents interfacial capacitance due to electrode polarization. R_{bulk}, CPE_{bulk}, and $Q_{interface}$ were held constant while $\alpha_{interface}$ was varied to demonstrate non-ideality. The resistivity of sample 40Li-60Si was used as reference, thus the geometric factor used in calculation is 0.21 cm^{-1}.

Parameter	Symbol	Value	Unit
Bulk Resistance	R_{bulk}	9.941	kΩ
CPE element of bulk capacitance	Q_{bulk}	5.11 x 10^{-11}	F $s^{\alpha-1}$
CPE element of bulk capacitance	α_{bulk}	0.89	adm
CPE element of interfacial polarization	$Q_{interface}$	3.14 x 10^{-5}	F $s^{\alpha-1}$
CPE element of interfacial polarization	$\alpha_{interface}$	1 to 0.8	adm

It is interesting to note that when all parameters are held constant except for $\alpha_{interface}$, the effective capacitance (C_{eff}) computed from equation (2) is lower than in the ideal case ($\alpha = 1$). For example, with $\alpha = 0.8$ the interfacial capacitance is about 23.5 μF, whereas for $\alpha = 1$ it is 31.5 μF. Thus, when $\alpha < 1$, C_{eff} is reduced relative to the ideal behavior, reflecting the phenomenon known as capacitance dispersion - discussed in Chapter 3 that can originate from interfacial heterogeneity, surface roughness, or distributed transport pathways.

4.2.5 Data analysis

The data analysis was simplified in comparison to that described in Chapter 3. In fact, in this Chapter the challenging aspect of measuring non-ideal capacitive behavior of electrode polarization was shown. Thus, we will employ the equation proposed by Tomozawa, which avoids determining the electrode capacitance by using the inflection frequency. This approach, validated for lithium disilicate (Chapter 3), is applied here to determine the charge carrier concentration across different Li_2O concentration in both silicate and phosphate glasses.

The raw data acquired on the impedance equipment, i.e, is the real (Z') and imaginary (Z'') part of impedance were translated into the permittivity formalism using the relationship shown below:

$$\varepsilon'(\omega) = \frac{-Z''}{\omega\, \varepsilon_0\, [(z')^2 + (z'')^2]}\, \frac{L}{A}, \qquad (3)$$

$$\varepsilon''(\omega) = \frac{Z'}{\omega\, \varepsilon_0\, [(z')^2 + (z'')^2]}\, \frac{L}{A}, \qquad (4)$$

where L/A is the sample geometric factor (cm^{-1}), ε_0 is the vacuum permitivity , $\omega = 2\pi f$) , and f is the frequency.

Once the values of ε' and ε'' were obtained as a function of frequency, this data was further processed by plotting the graph of the second and first

derivatives ($\frac{d^2\varepsilon'}{df^2}$ and $\frac{d\varepsilon''}{df}$), respectively, to determine graphically the inflection and peak frequency at the intersection with y=0, as exemplified in Figure 3-2.

Then, the estimation of charge carrier concentration (n_e) was determined by employing a rearranged version (Equation 5) of equation (9) of Chapter 3:

$$n_e = \left(\frac{2\sigma_{dc}(2+\rho)}{L\,\omega_{inflection}}\right)^2 \frac{kT}{e^2\varepsilon_0\varepsilon_\infty} \qquad (5)$$

where T the temperature, k is the Boltzmann constant, ε_∞ is the relative permittivity at high frequency estimated by the apparent (or geometrical) capacitance of the bulk glass at high frequency, ρ is the blocking factor (ρ=0 for blocking electrodes and > 0 for partially blocking), $\omega_{inflection} = 2\pi f_{inflection}$) is related to the inflection frequency ($f_{inflection}$) on the graph of real part of complex permittivity (ε') vs log(f) , where f is the applied frequency.

Finally, mobility was calculated based on equation (1) of Chapter 1, which rearranged for lithium-ion mobility turns into Equation (6):

$$\mu_{Li^+} = \frac{\sigma_{d.c.}}{n_e\ e}, \qquad (6)$$

Regarding the data fitted by Zview software using an equivalent circuit (($R_{bulk} \parallel CPE_{bulk}$) – CPE$_{interface}$), the results extracted from the fit were only the bulk glass resistance used to calculate the ionic conductivity and the $\alpha_{interface}$ from electrode's CPE to estimate the degree of deviation from ideality. In this analysis, the goal was not to achieve an exact interfacial fit, but to gauge the extent of non-ideal behavior; accordingly, a single CPE was used to represent interfacial polarization. Figure 4-2 presents representative fits illustrating three cases: the closest response to an ideal behavior, an intermediate case, and the most pronounced deviation observed in this study. Note that, for all three examples, Figure 4-2 show a good fit up to the inflection frequency of ε', which will be used to calculate the effective number of charge carriers. Also, to better fit a lower frequency, it should be added additional elements to the equivalent circuits.

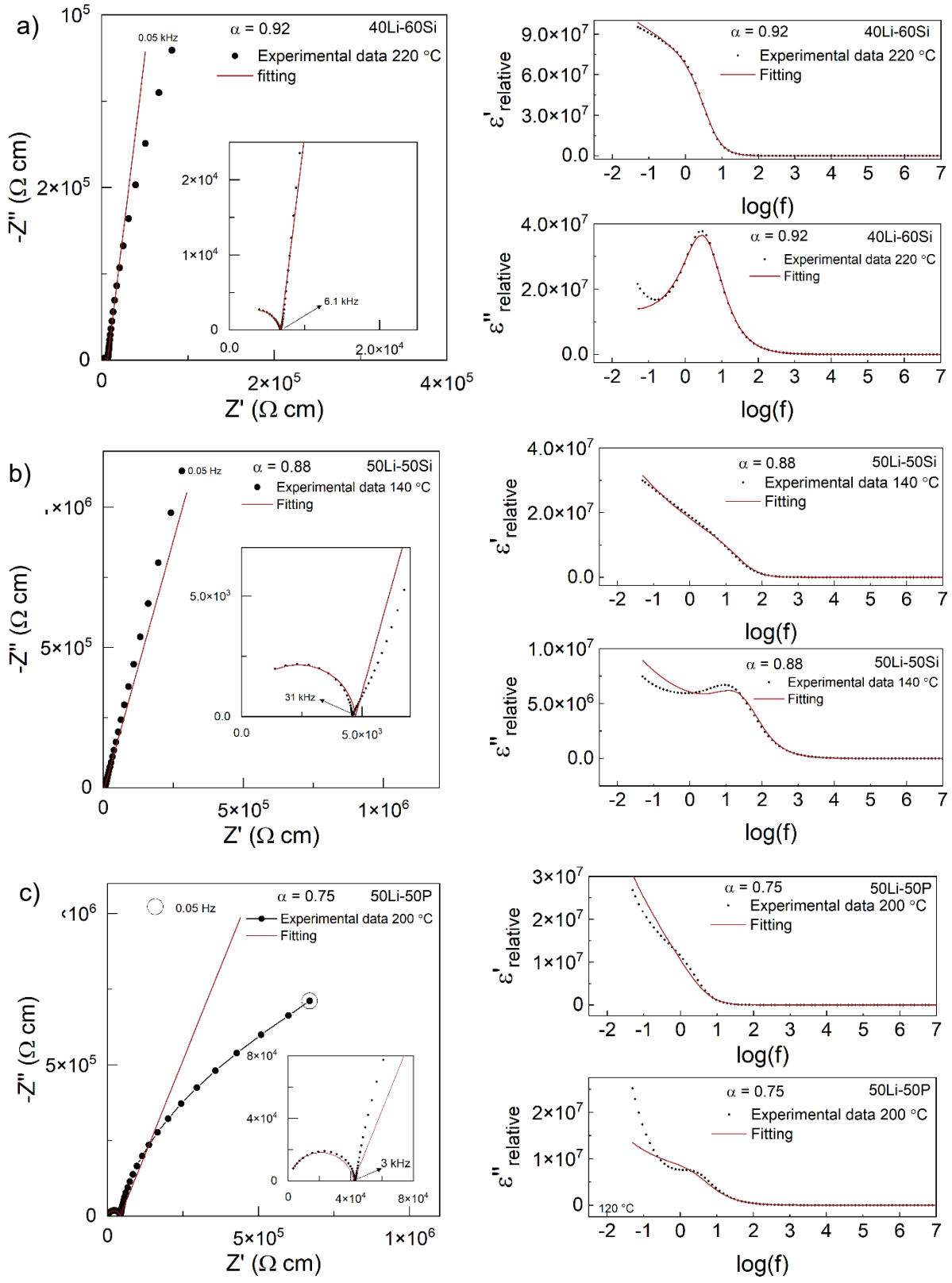
a)
α = 0.92
40Li-60Si
Experimental data 220 °C
fitting
0.05 kHz
6.1 kHz
-Z'' (Ω cm)
Z' (Ω cm)
Fitting
log(f)
b)
α = 0.88
50Li-50Si
Experimental data 140 °C
31 kHz
c)
α = 0.75
50Li-50P
Experimental data 200 °C
3 kHz
120 °C

Figure 4-2. Representative scenarios of fitting the interfacial capacitance with a CPE for three values of $\alpha_{interface}$ (a) 0.92, (b) 0.88 and (c) 0.75. The goal is not to get a perfect fit, but rather to estimate the deviation from ideality. Note that, in all three cases there is a good fit up to the inflection frequency, which validates our approach.

4.3 Results

4.3.1 Glass Thermal Characterization

Thermal characterization of the Li_2O – SiO_2 and Li_2O – P_2O_5 glass system was conducted as shown in Figure 4-3. For lithium silicate system (Figure 4-3a), the glass transition temperature found is comparable to previous reports [68–70,76]. As expected, it is observed a decrease in T_g with increasing Li_2O content. On the other hand, for phosphate system, Figure 4-3b and Figure 4-4 reveals that Tg remains relatively constant across the x Li_2O – (1-x) P_2O_5 series, with a slightly tendency to decrease with increasing Li_2O, also consistent with literature [24,77,78]. However, it is important to note that the literature on phosphate glasses presents a wide variation in T_g values. For example, T_g for 50% mol lithium composition ranges from 310 °C [79] to 329 °C [22], for 60% it ranges from 312 °C [79] to 322 °C [22]; while 64.5% data is lacking, values for 65–70% Li_2O range from 302 °C to 340 °C [79,80].

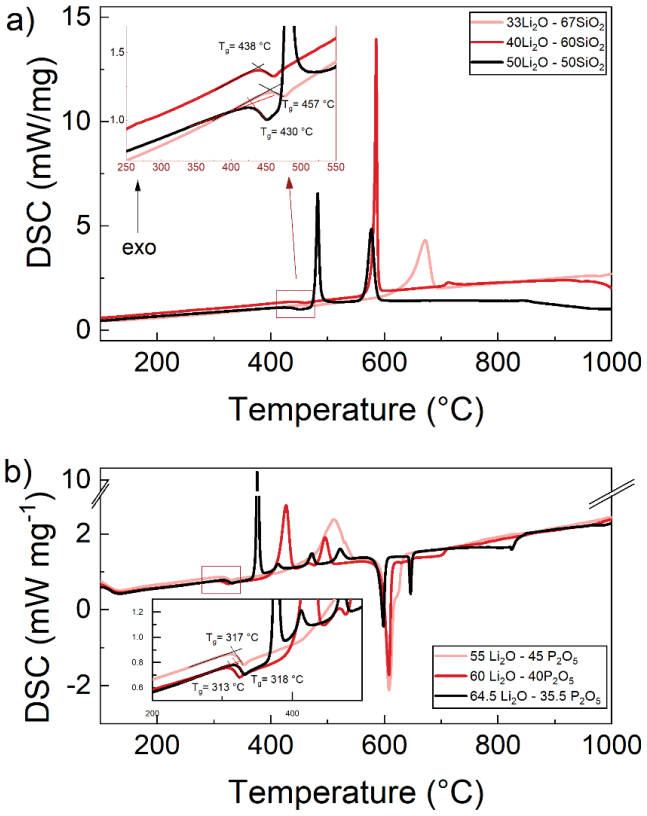

Figure 4-3. Differential scanning calorimetry curve for as quenched lithium silicate glasses (a) and lithium phosphate glasses (b). Data were acquired on bulk glass at a heating rate of 10 °C min^{-1} in platinum crucible with lid.

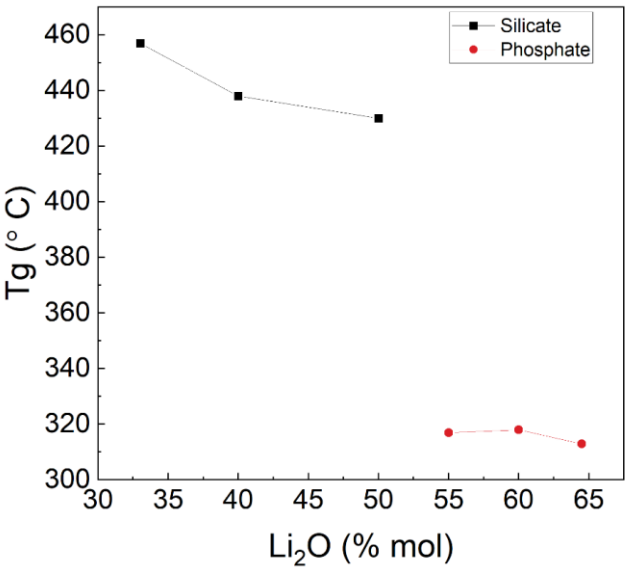

Figure 4-4. Glass transition temperature as a function of Li_2O concentration for silicate and phosphate systems. Lines are guide to the eyes.

4.3.2 Electrical Measurements

4.3.2.1 Lithium Silicate System

Figure 4-5 exhibits the Nyquist plots for the Li_2O – SiO_2 glass system at various temperatures for each composition. It is observed that for the first three temperatures for each composition, the electrode spikes are nearly parallel to each other, while for the last two temperatures, a slight bent of the electrode can be seen. For the 33 mol% and 40 mol% Li_2O compositions (Figure 4-5 a,b), the electrode response approaches an ideal behavior at lower temperatures. Specifically, $\alpha_{interface}$ ranges from 0.87 to 0.90 for the 33 mol% sample, and from 0.84 to 0.92 for the 40 mol% sample across all temperatures. Interestingly, further increasing the Li_2O content to 50 mol% (Figure 4-5c) resulted in $\alpha_{interface}$ varying between 0.78 to 0.84. It is noteworthy that, at lower temperatures, and for the analyzed frequency range the electrode spike approaches a straight line; consequently, a smaller $\alpha_{interface}$ manifests as a more tilted electrode spike, rather than a curved electrode spike. At higher temperatures, the non-ideality becomes more evident, with a more pronounced curvature in the response.

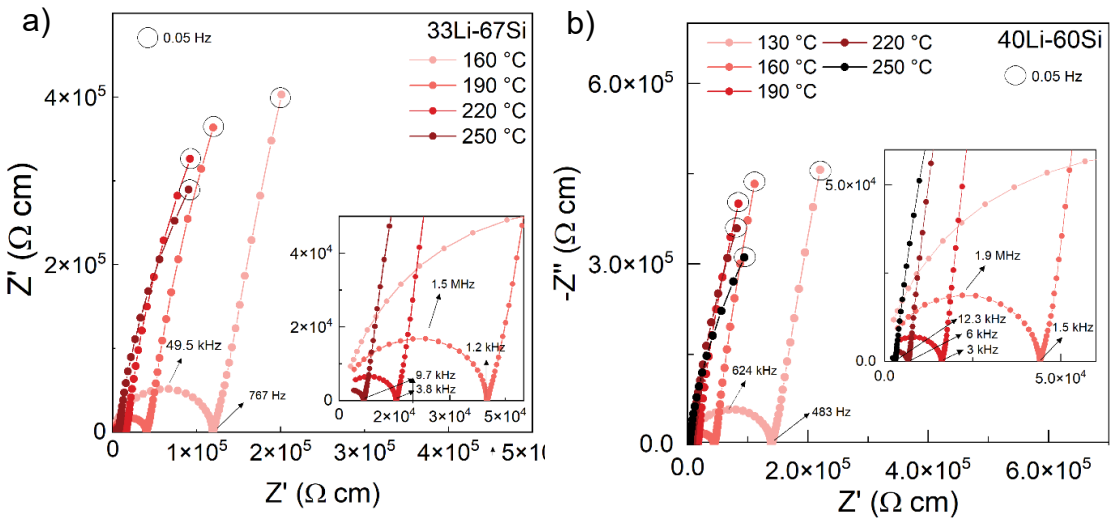

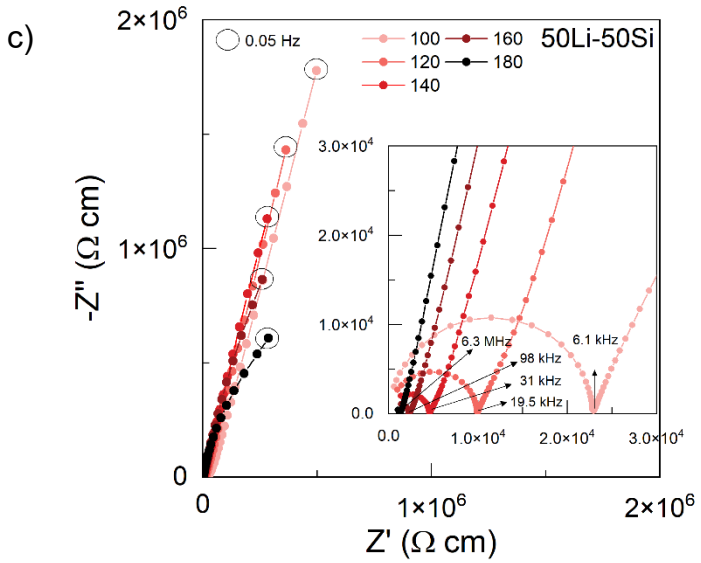

Figure 4-5. Nyquist plot for glasses from the Li_2O – SiO_2 system in every temperature according to Table 4-1 for Li_2O concentration of (a) 33%, (b) 40% and (c) 50% mol.

The non-ideality can also be seen in Figure 4-6, which shows the frequency dependence of the complex permittivity plotted at various temperatures. In fact, Figure 4-6a,b, corresponding to the 33 mol% and 40 mol% Li_2O compositions, show a clear inflection point in the real part of the permittivity (ε'), which corresponds to a well defined peak frequency in the respective plot of the imaginary part (ε'') of permittivity. The more inclined electrode spike seen on Nyquist plot (Figure 4-6c) translates as considerably less pronounced features for the 50 mol% Li_2O composition. Observe that the real part of permittivity exhibits nearly a straight line upon polarization, and the imaginary part display shallow peaks when compared to 33 and 40 mol%. This degree of non-ideality may have an impact on the value of interfacial capacitance, since the capacitance dispersion can be related to the discharge of the electric double layer.

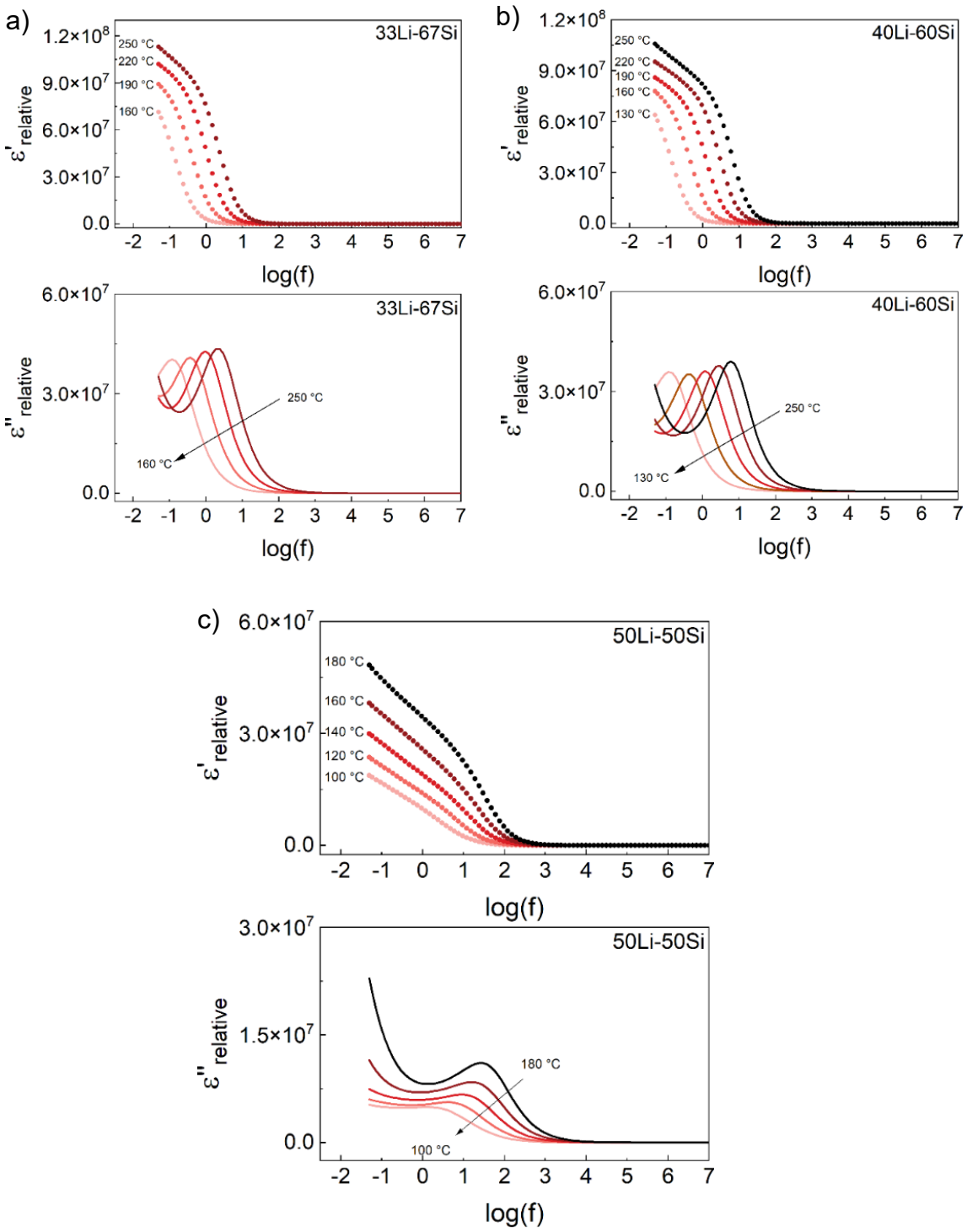

Figure 4-6. Real (ε') and imaginary (ε'') part of complex permittivity vs log (f) for silicate glasses with different Li_2O concentration: a) 33 mol%, b) 40 mol% and c) 50 mol%.

Using the bulk resistivity extracted from Nyquist diagrams (Figure 4-5) at different temperatures, we constructed Arrhenius plots for glasses with varying Li_2O concentration. In parallel, the inflection frequency, the high-frequency permittivity (ε_∞) and the measured conductivity were combined to compute the effective number of charge carriers at each temperature according to Equation (5). Thus, Figure 4-7 presents the temperature dependence of ionic conductivity and charge carrier density for the three investigated glasses in the Li_2O–SiO_2 system, displayed in an Arrhenius plot. As expected and consistent with the literature [76,81], ionic conductivity increases with rising alkali content. Notably, the conductivity enhancement from 33 to 40 mol% Li_2O is accompanied by a significant increase in the measured charge carrier density (n_e) with a nearly constant mobility (calculated from Equation (6)), as shown in Table 3. For example, at 160 °C, n_e increases from 1.25×10^{21} cm^{-3} to 1.51×10^{22} cm^{-3}, while the calculated mobility is 3.9 x 10^{-8} and 9.3 x 10^{-9} cm^2 $V^{-1}s^{-1}$, respectively. Further increase in Li_2O concentration to 50 mol%, despite exhibiting the highest conductivity, shows a lower n_e value of 2.34×10^{21} cm^{-3} compared to the 40 %mol Li_2O glass. As discussed before, this behavior can be associated with the discharge of the interface due to its stronger deviation from ideality. As a result, a smaller density of charge carriers is reflected in a sudden increase in mobility by two orders of magnitude, as shown in Table 4-3. Even if you consider a “saturation” of charge carrier, that is, considering the charge carrier density of 50 mol% as the same of 40 mol%, this mobility at 50 mol% would be 1.74 x 10^{-7} cm^2 $V^{-1}s^{-1}$, which is still one order of magnitude higher than 40 mol%. It is worth mentioning that the total number of charge carriers, obtained at the intersection of the n_e Arrhenius curve with the log (ne) axis when 1000/T tends to zero (N_{t_exp}), are in the same order of magnitude to the theoretical ones calculated from density measurements (N_{t_the}), as shown in Table 4-3. This result validates our approach.

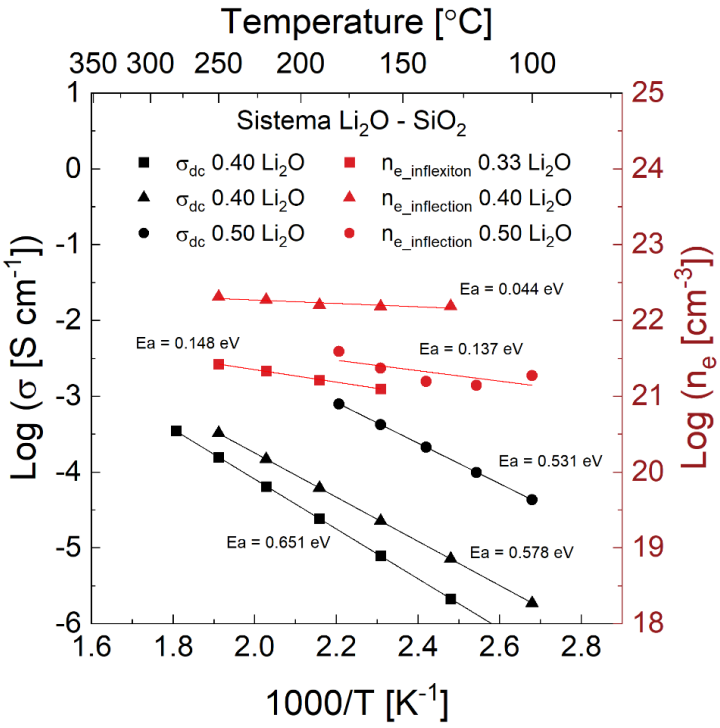

Figure 4-7. Arrhenius plot of ionic conductivity and concentration of effective charge carriers for silicate glasses with three different Li_2O concentrations, indicated in mol%. The conductivity is represented in black while the effective charge carrier density is shown in red. The effective charge carrier density was calculated from the inflection frequency of the real part of complex permittivity.

Table 4-3. Ionic conductivity, activation energies, charger carrier density and mobility estimated for the Li_2O - SiO_2 system at 160 °C, Log (σ_0), total number of charge carriers obtained from the extrapolation to infinite temperature of Arrhenius plot in Figure 4-7 (Nt_exp), and the theoretical number of charge carriers calculated from density measurements (Nt_the).

Li_2O (%mol)	$\sigma_{160\,°C}$ (Ω^{-1} cm^{-1})	$n_{e\,160\,°C}$ (at cm^{-3})	$\mu_{160\,°C}$ (cm^2 V^{-1}s^{-1})	Log σ_0	N_{t_exp} (cm^{-3})	N_{t_theo} (cm^{-3})	Ea σ (eV)	Ea n_e (eV)	Ea μ (eV)
33	8.8E-06	1.3E+21	3.9E-08	2.48	6.8E+22	1.9E+22	0.652 (0.001)	0.15 (0.01)	0.50 (0.01)
33*	1.62E-05	1.1E+21	9.2E-08	2.81	3.2E+22	1.9E+22	0.654 (0.001)	0.12 (0.01)	0.53 (0.01)
40	2.3E-05	1.5E+22	9.3E-09	2.08	5.2E+22	2.4E+22	0.578 (0.001)	0.04 (0.01)	0.53 (0.01)

50	4.2E-04	2.3E+21	1.1E-06	2.80	9.8E+22	3.1E+22	0.531 (0.001)	0.14 (0.07)	0.39 (0.07)

*Results from Chapter 3 for lithium disilicate.

Table 4-3 also highlights the influence of Li_2O content on activation energies. From 33 to 40 mol% Li_2O, the activation energy for ionic conductivity, Ea(σ), decreases in parallel with a drop in the charge-carrier activation energy, Ea(n), while activation energy for the mobility, Ea(μ), remains approximately unchanged. As a result, this provides an additional perspective supporting the view that the rise in ionic conductivity is driven by an increase in charge-carrier density. In contrast, between 40 and 50 mol%, Ea(n) increases slightly, whereas Ea(μ) presents a more pronounced decrease. Consequently, although charge-carrier dissociation energy increases, the activation energy of mobility appears to be the dominant factor enhancing ionic conductivity for this alkali concentration. It is evident that the interplay of these two factors fundamentally governs ionic conductivity.

4.3.2.2 Phosphate System

Figure 4-8 brings the Nyquist plots of the Li_2O – P_2O_5 system. For the composition with 55 mol% Li_2O, it is possible to see that even for intermediary temperatures (160 °C), there is a significant deviation from ideality, with $\alpha_{interface}$ = 0.82 up to $\alpha_{interface}$ = 0.75 at 200 °C, if we consider an equivalent circuit with only a CPE representing the electrode, as shown in Figure 4-2. Note that at 200 °C and lower frequencies (Figure 4-8a), there is a significamt bend of the electrode spike. On the other hand, composition 60 and 64.5 Li %mol shows straight lines of electrode spike, with $\alpha_{interface}$ varying from 0.86 to 0.88 and from 0.80 to 0.85, respectively across all temperatures. However, in this case, the lower $\alpha_{interface}$ reflects a more inclined polarization spike rather than significative curvature, as can be seen in Figure 4-8c. Comparing the $\alpha_{interface}$ parameter, the deviation from ideality is more pronounced for phosphate system than to silicate system.

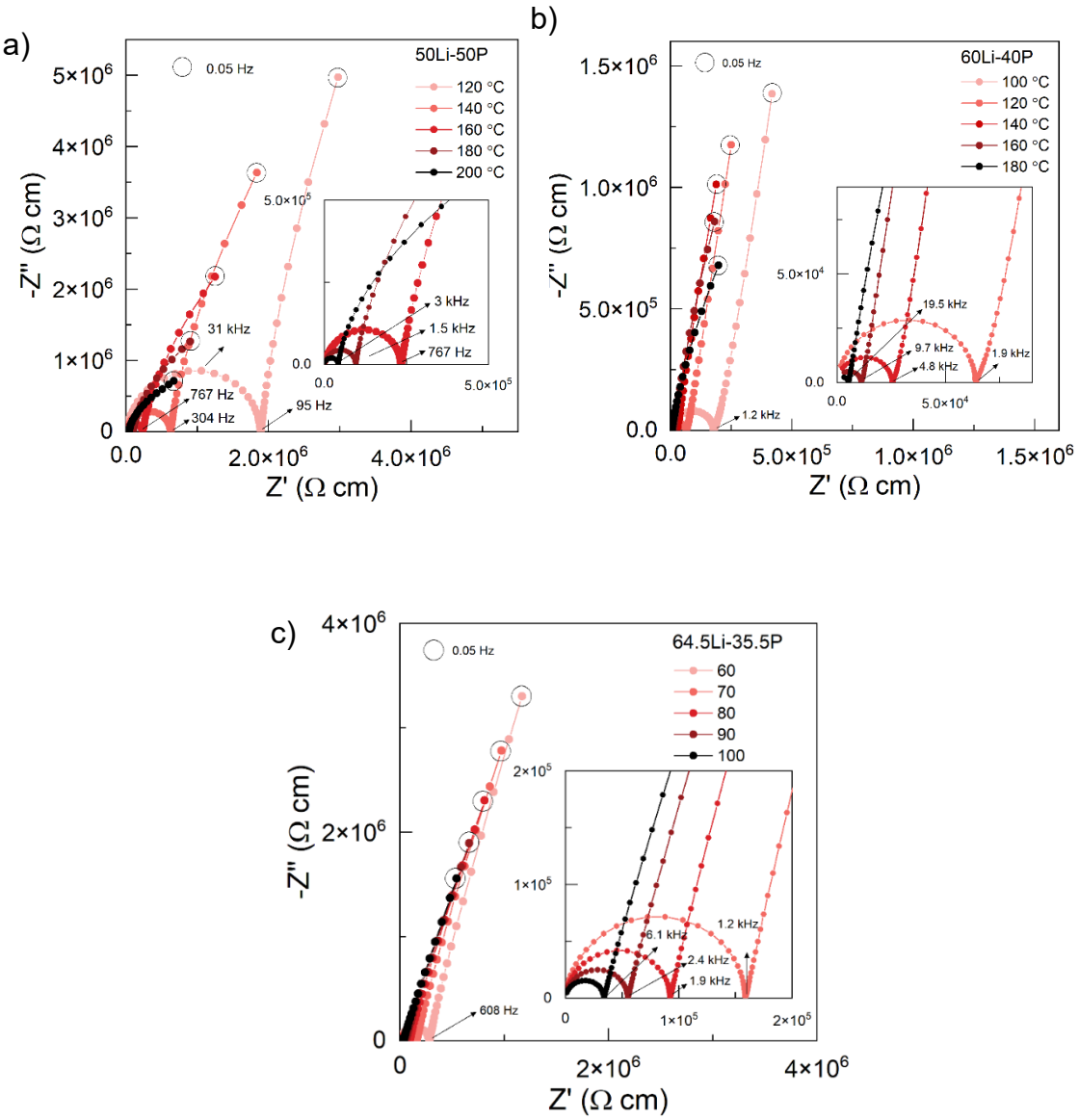

Figure 4-8. Nyquist plot for glasses from the Li_2O - P_2O_5 system in across all temperatures for Li_2O concentration (mol %) of (a) 55%, (b) 60% and (c) 64.5%.

The non-ideality is also displayed in the frequency dependence of the complex permittivity for the Li_2O – P_2O_5 glass system at various temperatures, shown in Figure 4-9. In Figure 4-9a, the three characteristics of ideality are less pronounced for 55%, reflecting the smaller values of $\alpha_{interface}$ for this sample. Figure 9b, corresponding to 60 mol% Li_2O composition, exhibits better defined expected characteristics, that is, a clear inflection points on the real part of the permittivity (ε'), with a corresponding narrow peak of the inflection frequency in

the imaginary part (ε''). This composition exhibits the closest from ideal behavior within the phosphate series. Even though, at high temperatures and low frequencies, it may be observed that there is a non-ideal behavior of the frequency-dependent formation of the space charge layer. Similarly for silicate system, for the highest Li_2O content, in this case, 64.5 mol% Li_2O, it is shown in Figure 4-9c that the non-ideal features are also more pronounced.

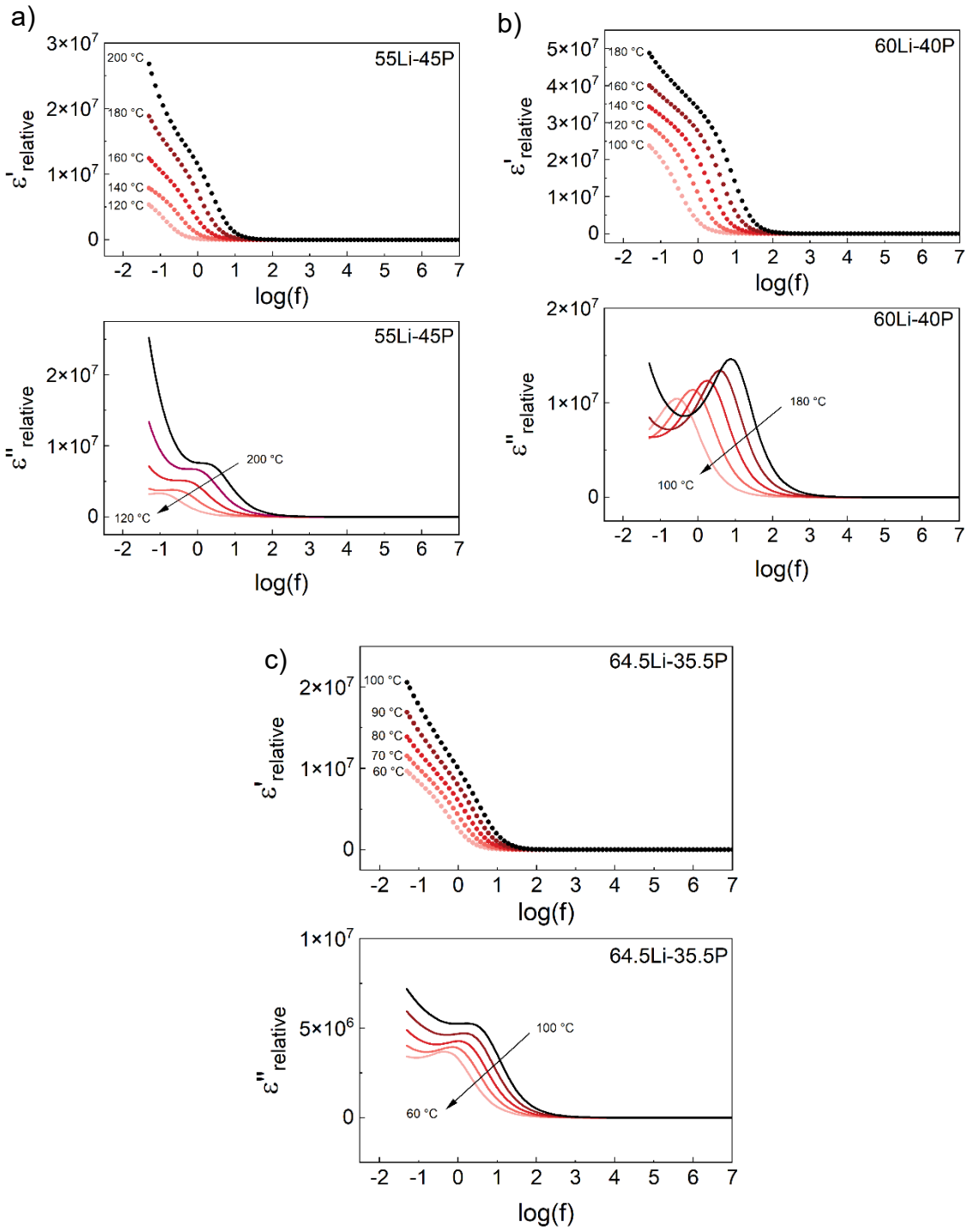

Figure 4-9. Real (ε') and imaginary (ε'') part of complex permittivity vs log (f) for glasses from the Li_2O-P_2O_5 system, for different Li_2O concentration. a) 55 mol%, b) 60 mol% and c) 64.5 mol%.

The Arrhenius plots in Figure 4-10 show the ionic conductivity and the density of charge carrier, calculated from equation (5). The same behavior is found for phosphates system, that is, it may be observed that, from 55 to 60 %mol of Li_2O, the increase in ionic conductivity is followed by an increase in charge carrier density. Moreover, Table 4-4 shows that this increase in conductivity occurs at rather comparable mobilities, reinforcing that the improvement is primarily driven by an increase in carrier concentration rather than changes in mobility.

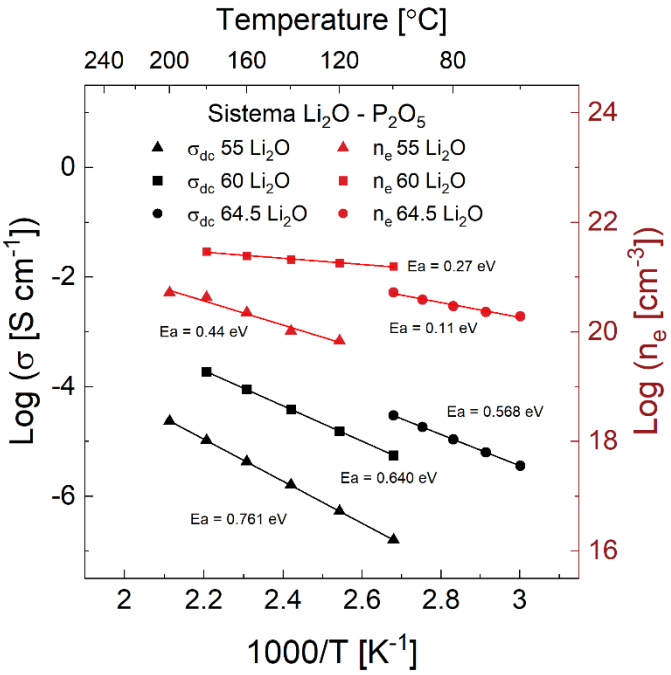

Figure 4-10. Arrhenius plot of ionic conductivity and of density of charge carrier, for glasses with different Li_2O concentration, from the Li2O-P_2O_5 system. The conductivity is represented in black while the charge carrier density is shown in in red. The effective charge carrier density was calculated from the inflection frequency of the real part of complex permittivity.

Table 4-4. Ionic conductivity, activation energies, charger carrier density and mobility estimated at 100 ℃ for the Li_2O – P_2O_5 system, Log (σ_0), total number of charge carriers obtained from the extrapolation to infinite temperature of Arrhenius plot in Figure 4-10, and the theoretical number of charge carriers calculated from density measurements (Nt_the).

Li_2O (%mol)	$\sigma_{100\,℃}$ (Ω^{-1} cm^{-1})	$n_{e\,100\,℃}$ (at cm^{-3})	$\mu_{100\,℃}$ (cm^2 V^{-1}s^{-1})	Log σ_0	N_{t_exp} (cm^{-3})	N_{t_theo} (cm^{-3})	Ea σ (eV)	Ea n_e (eV)	Ea μ (eV)
55	1.58E-07	3.25E+19	3.05E-08	3.47	2.64E+25	1.58E+22	0.761	0.44	0.32
60	5.55E-06	1.56E+21	2.22E-08	3.39	4.91E+22	2.24E+22	0.640	0.11	0.53
64.5	2.95E-05	5.24E+20	3.52E-07	3.15	2.10E+24	2.44E+22	0.568	0.27	0.30

Note that, even though the charge carrier's density of 60 Li_2O mol% glass is about two orders of magnitude higher than for sample with 55 Li_2O mol%, the variation in mobility is small, at 3.1 x 10^{-8} and 2.2 x 10^{-8} cm^2 V^{-1}s^{-1}, respectively. Further increase of Li_2O in the glass up to 64.5mol% lead to a slight decrease in the charge carrier's density and yet display the highest conductivity. In the same way of silicate system, the rise in ionic conductivity for the composition with highest Li_2O content is related to a significant increase in mobility. The experimentally determined total charge carrier density ($N_{t,\mathrm{exp}}$) from the extrapolation of data on Figure 4-10 closely matches the theoretical value (obtained by density data) for the composition with 60 mol% Li_2O. However, for 50 and 64.5 mol% this value deviates from that calculated from density by two orders of magnitude. Even if the absolute values of n_e may deviate from the true charge carrier density — owing to differences between $N_{t,\mathrm{exp}}$ and $N_{t,\mathrm{the}}$ for the 55 and 64.5 mol% compositions, it is still possible to analyze the activation energy, since a possible error on the determination of effective charge carrier will not affect its temperature dependence.

Table 4-4 highlights the influence of Li_2O content on activation energies for the phosphate system. From 55 to 60 mol% Li_2O, the activation energy for ionic conductivity, Ea(σ), decreases in parallel with a reduction in the charge-carrier activation energy, Ea(n_e). This trend indicates a lower dissociation barrier, yielding a larger density of free ions available for conduction. Conversely, between 60 and 64.5 mol%, Ea(n) increases, whereas Ea(μ)

decreases, which is the same behavior observed in vitrification limit for silicate system (50 mol% of Li_2O).

4.3.3 Charge Carrier Density and Mobility

Figure 4-11 presents the calculated charge carrier density (n_e) and mobility (μ) as a function of Li_2O concentration (mol%) for the two investigated: glass systems Li_2O–SiO_2 and Li_2O – P_2O_5. Interestingly, both systems displayed similar behavior, that is, the first two data points for each system (33 and 40 mol% for SiO_2 and 55 and 60 mol% for P_2O_5) show that mobility varies to a low extent in comparison to the increase in n_e. In other words, the increase in n_e with rising Li_2O content is the driving factor for rising ionic conductivity. Further increasing the alkali concentration (50 mol% for SiO_2 and 64.5 mol% for P_2O_5) lead to a slight reduction in charge carrier density, yet the total conductivity continues to improve. As described hereinbefore, the non-ideal behavior decreases the electrode capacitance compared to an ideal behavior. Thus, even if we consider that the charge carrier density for composition near vitrification limit are underestimated — and even if one assumes carrier saturation, as suggested in Figure 4-11b, an enhancement in ion mobility is still evident. In this high-alkali regime, the conductivity enhancement is driven by faster ion kinetics rather than a higher carrier density. This behavior suggests a shift in the dominant transport mechanism at elevated alkali contents and aligns with the tendency of compositions beyond this range to crystallize upon cooling, likely facilitated by the high mobilities.

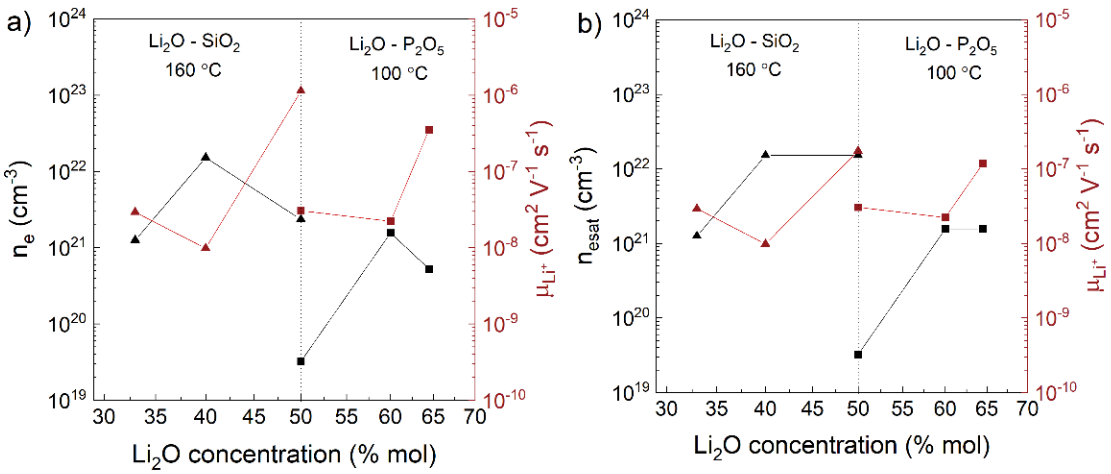

Figure 4-11. Charge carrier density for silicate and phosphate system as function of Li_2O alkali concentration estimated from inflection point. The corresponding mobility was calculated from conductivity and charge carrier density as shown in Equation XX for (a) measured data and (b) considering a saturation of charge carrier.

Near the vitrification limit, it is observed an increase in charge carrier activation energy from 0.04 to 0.14 eV on silicate and 0.11 to 0.27 eV on phosphate glasses, along with a respective decrease in the activation energy for mobility. Regarding the decrease in Ea μ, we hypothesize that the reduction in molar volume with increasing Li_2O concentration may contribute to higher mobility by reducing the jump distance and, thus, increasing the attempt frequency. In other words, this means more successful jumps and thus contributing faster long-range displacement. Regarding the charge carrier density, the increase in charge carrier formation energy suggests new interaction. For example, carbon retention due to high content on carbonates used in these high Li_2O composition is known to happen primarily in glasses with high alkali oxide content [82–85]. MAS-NMR studies [84] have demonstrated that in high alkali sodium borate glass, carbon retention (CO_2 or CO_3^{2-}) is surrounded by Na^+ ions. As a result, new ion-CO_3^{2-} interactions can also contribute for the increase in charge carrier formation activation energy, besides possibly providing new path for lithium migration with high mobility.

As a result, we identified two different behaviors in both systems. The first is, where ionic conduction is largely carrier-density controlled, which is in alignment with Ravaine and Souquet model, where mobility should be composition independent [1,75]. Also, it is observed that in these glasses the modifiers are weakly dissociated, with low number of charge carriers available for conduction (around 1% at ambient temperature); The second behavior, near the vitrification limit, the mobility becomes dominant. Further experimental and theoretical investigations should focus on the transitional concentration range between 40 and 50 mol% Li_2O for silicate and 60 to 65 mol% for phosphate

systems to deepen the understanding of the underlying change in conduction mechanisms.

4.4 Conclusion

This chapter determined how the effective charge-carrier density, n_e, and the mobility, μ, varies with Li_2O content in Li_2O–SiO_2 and Li_2O–P_2O_5 glasses. Across both systems a common, two-regime behavior emerges. At moderate alkali concentration, conductivity increases are driven primarily by a rise in n_e while μ remains nearly composition-independent, consistent with a weak-electrolyte picture. This is a result of a reduction of dissociation energy (Ea_{ne}), which increases concentration of free mobile ions for the same temperature, while the activation energy variation for mobility is less expressive. Near vitrification limits (50 mol% SiO_2; 64.5 mol% P_2O_5), a decrease in the mobility activation energy which may indicate a mobility-controlled increase of ionic conductivity at high alkali concentration. Additionally, only a fraction of Li^+ $(\text{around } 1\%)$ is thermodynamically free at room temperature, also in agreement with the weak electrolyte model. Electrode responses deviate from ideal blocking at higher Li_2O concentration (lower α of the CPE), especially in phosphate glasses. To conclude, the mechanism governing ionic conductivity transition from carrier-density control at moderate Li_2O concentration to mobility control as the glass approaches its alkali solubility limit of the studied systems.

CHAPTER 5 – IMPACT OF CHLORINE ON THE CONDUCTIVITY IN LI20 – P2O5 – ALCL3 GLASSES REVEALED BY SOLID STATE NMR AND IMPEDANCE SPECTROSCOPY

Based on a paper submitted to Journal of Alloys and Compounds

5.1 Introduction

In the previous chapters we could understand that the dissociation energy between charge carrier and its compensating pair may be the dominant part of improving the conductivity in the glassy region for the compositions under study. In this chapter we pretend to take one step further in designing a new composition based on the knowledge acquired so far.

The effect of Cl^- incorporation within the glass structure to enhance ionic conductivity was first reported by Levasseur et al. [18], Malugani and Robert [17], and Doreau et al. [22] which showed the potential of optimizing the ionic conductivity by introducing halides in lithium-conducting glasses for improved solid-state electrolyte performance. It was later demonstrated that halogens do not participate in the network formation and are decoupled from the network [17–19,22,26]. Additionally, a few works demonstrate that ionic conductivity can be significantly improved through partial substitution of Li_2O with Li_2X_2, even without increasing the overall concentration of charge carriers [19,20,25]. Furthermore, it is known that the larger the halogen radius the greater the improvement in ionic conductivity [22]. For instance, for the same salt concentration it is shown that LiI incorporation in Li_2O-P_2O_5 system can provide higher conductivity than LiBr, which is higher than LiCl [22].

Based on this context, the use of complex anions larger than single-atom anions was proposed as a strategy to achieve even greater enhancements in ionic conductivity. As a result, $AlCl_3$ is expected to decompose in $AlCl_4^-$ [86,87]

when thermally decomposed, and was proposed to be used as additive in Li_2O-P_2O_5 glass system.

In this work, we propose a novel glass composition not previously reported in the literature, aiming to enhance the ionic conductivity by introducing chlorine ions through $AlCl_3$ into lithium phosphate glass. We investigated both the structural effects arising from the mixed former effect between Al_2O_3 and P_2O_5 [13,14], and the effect of halogen incorporation, assessing their synergic impact on the enhancement of ionic conductivity.

5.2 Material and Methods

5.2.1 Glass Synthesis

Binary lithium phosphate glasses ($y$$Li_2O$–[100–$y$]$P_2O_5$, with y={55, 60, and 64.5}) were obtained through the melt and quench technique in final 20 g batches. Stoichiometric amounts of Li_2CO_3 (Sigma Aldrich, ≥99,0%) and $NH_4H_2PO_4$ (Sigma Aldrich, 98%) were homogenized in a high-speed mixer (FlackTek™) for 3 rounds of 3 minutes at 1700 RPM, with 2 minutes intervals between cycles. The homogenized material was placed in a platinum crucible at 800 °C for 1 h using an electric furnace (Deltech DT-33-RS-812-C) to release volatiles such as ammonia, water, and carbon dioxide from the starting reagents. Subsequently, the temperature of the melt was lowered to 600 °C for another hour to reduce the viscosity before casting and splat-cooling the melt between two stainless steel plates.

For synthesis of the ternary glasses with general formula (100–x)[$y$$Li_2O$–(100–$y$)$P_2O_5$)]–$x$$AlCl_3$, with x = {5, 10, and 15}, the obtained base glasses, 55Li_2O–45P_2O_5 (labeled 55Li), 60Li_2O–40P_2O_5 (labeled 60Li), and 64.5Li_2O–34.5P_2O_5 (labeled 64.5Li), were ground to a fine powder using an agate mortar and mixed with $AlCl_3$ (Sigma Aldrich, 99%) in appropriate proportions and homogenized in an agate mortar. The mixtures were then melted in porcelain crucibles covered with lids to avoid halogen volatilization [88], at 800 to 1200 °C depending on the composition (see Table 5-1) for 10 minutes to yield final 5 g batches. Some fuming was observed during melting.

Table 5-1. Summary of the samples label, nominal composition (mol%) and the experimental melting temperature of the glass series studied in this work.

Sample Label	Nominal Composition	T_m (°C)
55Li	$55Li_2O–45P_2O_5$	600
55Li-A	$95(55Li_2O–45P_2O_5)–5AlCl_3$	800
55Li-B	$90(55Li_2O–45P_2O_5)–10AlCl_3$	900
55Li-C	$85(55Li_2O–45P_2O_5)–15AlCl_3$	1000
60Li	$0.60Li_2O–0.40P_2O_5$	600
60Li-A	$95(60Li_2O–40P_2O_5)–5AlCl_3$	850
60Li-B	$90(60Li_2O–40P_2O_5)–10AlCl_3$	900
60Li-C	$85(60Li_2O–40P_2O_5)–15AlCl_3$	1050
65Li	$64.5Li_2O–34.5P_2O_5$	600
64.5Li-A	$95(64.5Li_2O–34.5P_2O_5)–5\ AlCl_3$	900
64.5Li-B	$90(64.5Li_2O–34.5P_2O_5)–10\ AlCl_3$	950
64.5Li-C	$85(64.5Li_2O–34.5P_2O_5)–15\ AlCl_3$	1200

5.2.2 Glass Characterization

All glasses were subjected to chemical analysis. The content of Li, P, and Al was determined by Inductively Coupled Plasma Optical Emission Spectroscopy (ICP-OES), while the Chlorine content was determined by the Schöniger method. Table 5-2 summarizes the measured and nominal contents of the elements present on each investigated glass studied.

Table 5-2. Experimental and nominal elemental composition (in mol%) of the three-glass series (oxygen was calculated from difference of other elements). Errors of experimental composition were obtained from triplicates' standard deviation and are in the first decimal place.

Sample	Experimental (and Nominal) elemental composition (mol%)				
	Al	Li	P	Cl	O
55Li	0.0 (0.0)	22.5 (22.9)	21.2 (18.7)	0.0 (0.00)	56.4 (58.3)
55Li-A	1.2 (1.1)	21.5 (21.9)	19.3 (17.9)	1.1 (3.2)	56.9 (55.9)
55Li-B	2.0 (2.1)	18.9 (20.9)	16.9 (17.1)	1.3 (6.4)	60.8 (53.4)
55Li-C	3.6(3.2)	17.9 (19.9)	16.8 (16.4)	0.6 (9.6)	61.1 (50.9)
60Li	0.0 (0.0)	25.7 (26.1)	18.3 (17.4)	0.0 (0.0)	55.9 (56.5)
60Li-A	1.3 (1.1)	24.4 (24.9)	17.1 (16.6)	1.5 (3.3)	55.8 (54.1)
60Li-B	1.9 (2.2)	24.1 (23.8)	16.7 (15.9)	1.4 (6.6)	55.9 (51.5)
60Li-C	2.4 (3.3)	22.2 (22.6)	15.8 (15.1)	1.6 (10.0)	58.0 (49.0)
64.5Li	0.0 (0.0)	27.8 (29.2)	16.5 (16.1)	0.0 (0.0)	55.7 (54.8)
64.5Li-A	1.2 (1.1)	26.2 (27.8)	15.6 (15.3)	0.8 (3.4)	56.3 (52.3)
64.5Li-B	2.0 (2.3)	26.1 (26.5)	15.2 (14.6)	4.0 (6.9)	52.8 (49.8)

64.5Li-C	5.2 (3.4)	17.5 (25.2)	13.2 (13.9)	0.1*(10.3)	64.0 (47.2)

*Below detection limit.

The density (ρ) of the samples was measured via Archimedes' principle, using a Mettler Toledo analytical balance equipped with a density kit for solid samples. The immersion liquid was isopropyl alcohol (Sigma Aldrich, 99.9%) with a residual water content below 0.1%. The molar volume (M_V) of the samples was calculated by applying $M_V = M/\rho$, where M is the molar mass of the glass calculated from the experimental compositions.

The glass transition (T_g) temperatures were determined by differential scanning calorimetry using a DSC-Netzsch 404, at a heating rate of 10 °C min^{-1}, and platinum crucibles with lids. The glass forming ability was estimated from Hrubý's glass forming parameter (K_H) [89], according to the following equation:

$$K_H = \frac{T_x - T_g}{T_m - T_x} \quad (1)$$

where, T_x, T_g and T_m are the onset of crystallization, onset of glass transition and crystallization peak temperatures, respectively.

Multinuclear ^{31}P and ^{27}Al solid-state NMR experiments were performed on an Agilent DD2 and a Bruker Avance 600 Neo spectrometer, respectively. ^{31}P MAS NMR spectra were recorded at 5.7 T. Magic angle spinning (MAS) experiments were performed at a resonance frequency of 98.24 MHz using a 3.2 mm MAS NMR probe operated at a spinning rate of 20.0 kHz. 64 scans were acquired with 90° pulses of 2.5 µs length at a recycle delay of 200 s, which produced quantitative spectra as inferred from the lack of further spectral changes when using higher values. BPO_4 was used as a secondary reference at –29.3 ppm vs 85% H_3PO_4 (0 ppm). ^{27}Al central transition MAS NMR experiments were performed at 14.10 T (Larmor frequency of 156.4 MHz) in a 2.5 mm triple-resonance probe at υ_{MAS} = 20 kHz. Short 0.8 µs pulses corresponding to a 25° tip angle were used for excitation and 256 transients were collected at recycle delays of 0.5 – 1 s. ^{27}Al chemical shifts are reported relative to a 0.1 M $Al(NO_3)_3$ solution (0 ppm) using AlF_3 as a secondary reference (–16 ppm). All NMR data were analyzed using the ssNake software [90].

Electrical characterization of the samples was carried out by complex impedance spectroscopy (Novocontrol Alpha-A High Performance Frequency Analyzer) in a two-point cell in air. From 40 to 140 °C, measurements were taken every 20 °C in the frequency range of 10^7 to 10^1 Hz with a voltage amplitude of 300 mV. Before measurements, the samples were dry polished, and gold electrodes were sputtered on both parallel sides using a Quorum Q150R ES equipment.

5.3 Results

5.3.1 Chemical Analysis and Macroscopic Properties

Table 5-2 shows the experimentally determined compositions of the glass samples under study. The measured Li, P, and Al content show good agreement with the nominal values, with deviations of less than 2.0, 1.3, and 0.4 mol%, respectively. The Li/P ratio within each series of glasses are nearly constant at 1.1, 1.4, and 1.7 for the series 55Li, 60Li, and 64.5Li, respectively. More pronounced differences can be observed for the 64.5-C sample which required melting at higher temperatures, which may have led to increased chlorine and lithium volatilization.

Markedly, for samples x = 10 (55Li-B, 60Li-B, and 64.5Li-B), higher Li/P ratios allowed more Cl^- to be incorporated in the glass. For example, the Cl^- concentration for Li/P = 1.1 (55Li-B), Li/P = 1.4 (60Li-B), and Li/P = 1.7 (64.5Li-B) are respectively 1.3, 1.6, and 4.0 mol%. This result suggests that either the amount of Cl^- incorporated into the glass network or chlorine volatilization is composition dependent. For most compositions, the measured chlorine content ranged from 1 to 4 mol%, whereas the theoretical content was expected to be between 3 to 10 mol%.

Table 5-3 further lists the densities and molar volumes of the glasses under study. It can be observed that densities increase as a function of Li/P ratio which can be attributed to Li occupying interstitial spaces, thereby increasing the packing of the structure. For example, the addition of Li and Na in

phosphate glasses increases the density [91–93] because the modifier cations interact with oxygen, decreasing the size of the interstitial spaces causing a shrinkage of the structure [9]. In addition, the presence of Al^{3+} and Cl^{-} may also contribute to the reduction of the density of the glasses under study. For example, studies on the Li_2O–P_2O_5–LiCl ternary system [94–96] report a decrease in the density upon doping the binary system with LiCl. A similar trend is observed in the Li_2O–Al_2O_3–P_2O_5 system, where six-coordinated Al^{3+} also contributes to a reduction in molar volume [13,14]. Interestingly, sample 64.5-C shows an increase in molar volume, which may be related to Li^{+} and Cl^{-} losses.

Table 5-3. Measured density (ρ) and molar volume (M_v) calculated from the experimental chemical composition for the Li_2O–P_2O_5–$AlCl_3$ glass system.

Sample	ρ (g cm^{-3})	M_v (cm^3 mol^{-1})
55Li	2.26	37.30
55Li-A	2.37	34.91
55Li-B	2.38	34.81
55Li-C	2.47	34.53
60Li	2.32	32.96
60Li-A	2.38	31.94
60Li-B	2.39	31.90
60Li-C	2.47	31.21
64.5Li	2.35	30.46
64.5Li-A	2.38	30.31
64.5Li-B	2.40	29.64
64.5Li-C	2.46	33.08

5.3.2 Differential Scanning Calorimetry

Thermal characterization of the glass system Li_2O–P_2O_5–$AlCl_3$ was carried out, and the obtained T_g values are shown in Figure 5-1, while DSC curves are presented in Figure 5-2. For the base glasses the glass transition temperature (T_g) does not vary significantly between 55Li, 60Li, and 64.5Li, being 315, 311, and 319°C, respectively. Moreover, the values agree well with data reported elsewhere. [24,77,78]. For instance, in the series Li_2O – P_2O_5, T_g values for 55Li have been reported to range from 310°C [79] to 329°C [22], while for 60Li, the values vary from 312°C [79] to 322°C [22]. Although specific data for the 64.5Li composition are unavailable, T_g values of 340°C for a binary

phosphate glass containing 65% Li_2O [79], and 309°C and 302°C for 67% and 70% Li_2O [80], respectively, have been reported. The incorporation of aluminum results in higher T_g values in all series, which is attributed to the replacement of P-O-P for P-O-Al linkages [14].

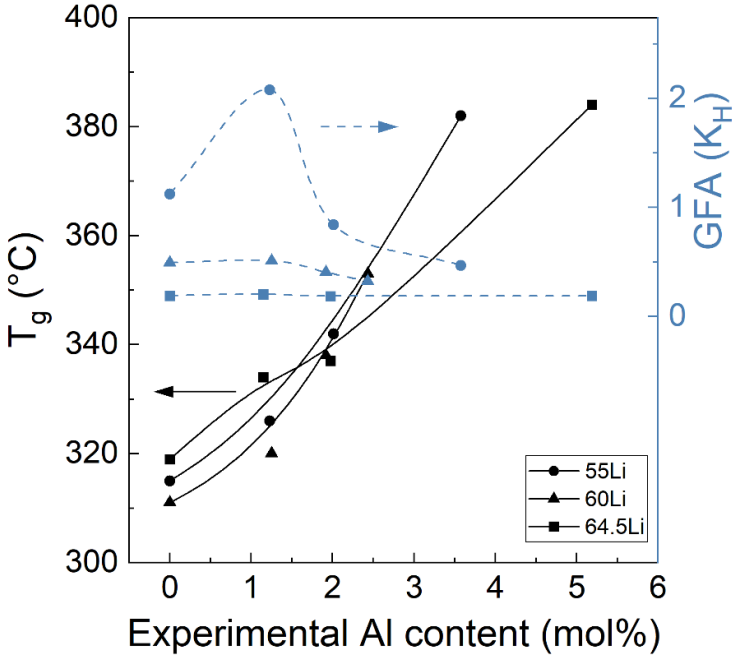

Figure 5-1. The glass transition temperature (T_g) as a function of experimental aluminum content (mol%) (shown in Table 5-2), for all investigated glasses. The Hruby's parameter (H_k) was calculated to evaluate the glass-forming ability (GFA) of the system. The lines are provided only as guides to the eye.

The glass forming ability (GFA) of the present series was evaluated using Hrubý's parameter (K_H), see Figure 5-1. It can be observed that for the base glasses, Hrubý's parameter expectedly decreases as the lithium oxide content increases, indicating a decrease in GFA. Interestingly, the addition of 1.2 mol% of Al increases the GFA of all base glasses. The most significant increase occurred for the 55Li-A composition: Figure 5-2 shows a shift of the crystallization peak to higher temperatures and a broadening (blue curve) compared to the base glass 55Li (red curve). This effect is visually evident for the 64.5Li base glass, which partially crystallizes upon splat cooling, while 64.5Li-A remains entirely glassy. Further increase in Al content led to a

decrease in GFA for all glasses, with values falling below those of the parent base glass.

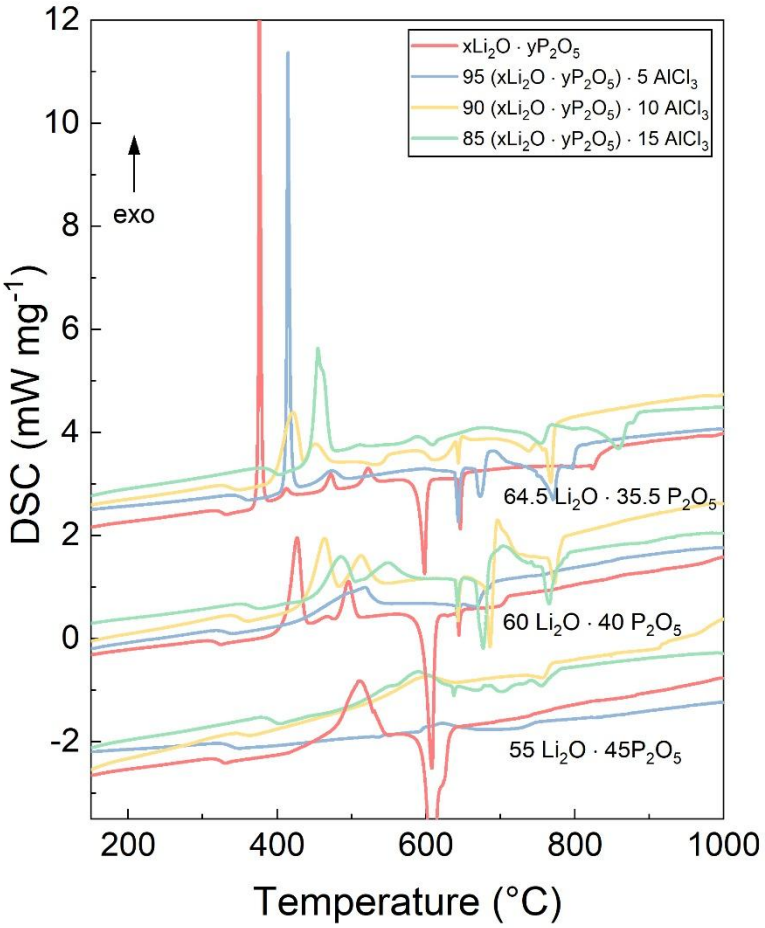

Figure 5-2. Differential scanning calorimetry curves for (100-x) (yLi_2O - zP_2O_5) · x $AlCl_3$ glass series, where x = 0, 5, 10, and 15. The values of y and z are provided in the graph. Curves were taken at a heating rate of 10 °C min^{-1} in a platinum crucible with a lid.

5.3.3 Solid-State NMR

The ^{31}P MAS NMR spectra of the samples under study are shown in Figure 5-3. The $AlCl_3$-free samples can be well fitted using two Gaussian peaks centered at about –4 and –20 ppm, corresponding to Q^1 and Q^2 species [97,98], respectively. In the Q^n_m nomenclature, the superscript *n* denotes the number of P-O-P bridges the quaternary (phosphorus) ion is involved in, and the subscript

m denotes the number of bridging oxygen atoms to elements other than P. In the P^n_m nomenclature, the superscript *n* denotes the total number of P-O-X bridges, while *m* has the same meaning. The relative intensity of both peaks varies expectedly as a function of the Li/P ratio: For the base glass $55Li_2O$-$45P_2O_5$, the experimental (and nominal) Li/P ratio of 1.22 predicts an <*n*> value of 1.94±0.05 (where <*n*> is the average number of bridging oxygen atoms over all P^n units of a glass), which stands in very good agreement with the experimental value of 1.81±0.05. For the other two base glasses, the calculated values of <*n*> = 1.60±0.05 and 1.32±0.05 also stand in good agreement with the experimental values of 1.54±0.5 and 1.26±0.05, respectively, and indicate the prevalence of pyrophosphate units.

In all glass series, the introduction of Al produces new lineshape features centered at about –10 and –30 ppm, which are not straightforward to attribute to P^n_m/Q^n_m units without additional information [97]. Problematic for the fitting and interpretation of the experimental ^{31}P NMR spectra is that both, the depolymerization of the phosphate units and the substitution of P-O-P for P-O-Al linages has a deshielding effect (signal shift towards higher frequencies). Therefore, a strong overlap of ^{31}P signals is expected, which cannot be resolved without more advanced NMR experimentation.

For the sake of the discussion, we have fitted the spectral differences between the base glasses and those doped with $AlCl_3$ by a minimum number of Gaussian contributions, arriving at a final fit shown in Figure 5-3 (see also Table S1 in appendix A).

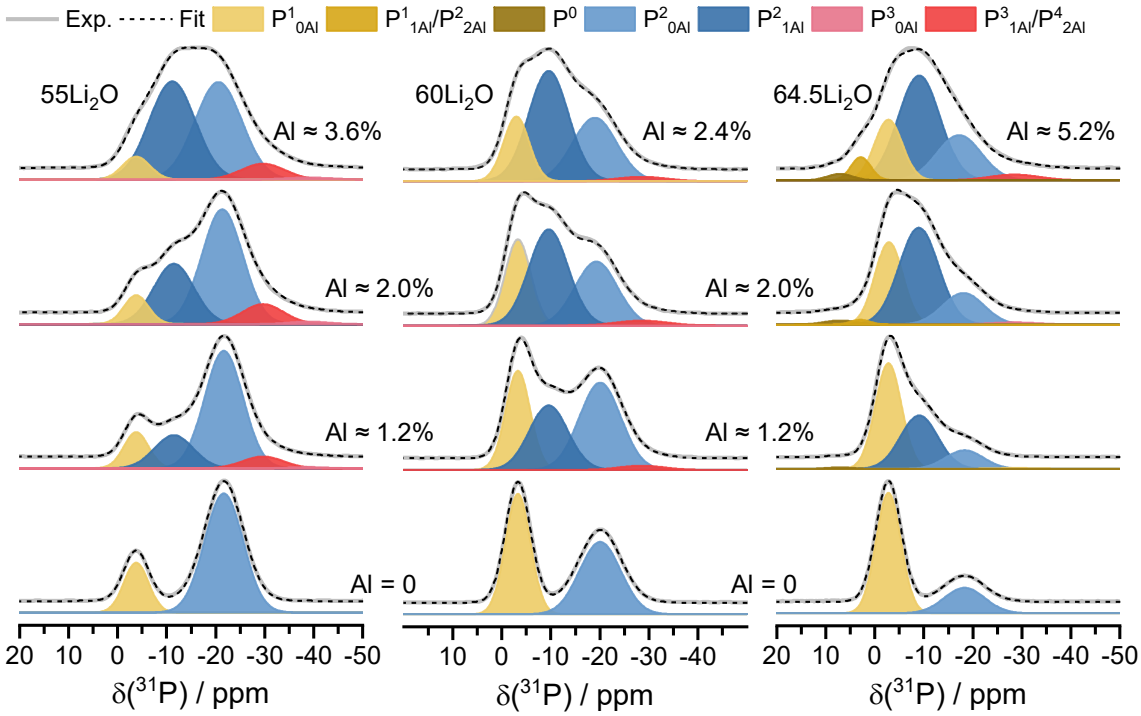

Figure 5-3. ^{31}P MAS NMR spectra of the glasses under study and line shape deconvolutions. The thick gray line corresponds to experimental data, the color-shaded solid curves are Gaussian fit components, and the dashed black line is the sum of the fit components, as indicated in the legend.

Figure 5-4 shows that the incorporation of $AlCl_3$ results in a continuous transformation of P^2 units into $P^2{}_{1Al}$ units across all compositions. At the same time, some signal intensity can be observed at lower chemical shifts of about –30 ppm and beyond for the two glass series $55Li_2O$ and $60Li_2O$. The signals over this region stem from higher polymerized P-species like $P^3{}_{1Al}$ or $P^4{}_{2Al}$ units, and their formation is an expected consequence of the demand for charge compensation of the produced $AlO_{4/2}^-$ species (compare with Figure 5-6). Interestingly, $AlCl_3$ addition seems not to lead to the formation of pyrophosphate species involved in P-O-Al linkages, i.e., $P^1{}_{1Al}$ units. Such species can only be observed for the glasses with the highest Al substitution degree within the $64.5Li_2O$ series. Overall, the degree of network polymerization <*n*> increases significantly when $AlCl_3$ is first added to the base glass, and then slightly as a function of $AlCl_3$ content for all three glass-series: by 0.2, 0.3, and 0.5, for the 55Li, 60Li and 64.5Li series, respectively. Especially noteworthy is the

pronounced increase by 0.2 from x = 5 to x = 10 in the 64.5Li_2O series, while for the other glasses, the increase in <*n*> value is roughly four times smaller (≤0.06). The effect of chlorine addition to the glass network could, in principle, be studied using $^{35/37}Cl$ NMR, but in addition to the rather unfavorable nuclear properties of the two active isotopes, the obtained spectra in glasses are typically too broad and, therefore, of little information content [98].

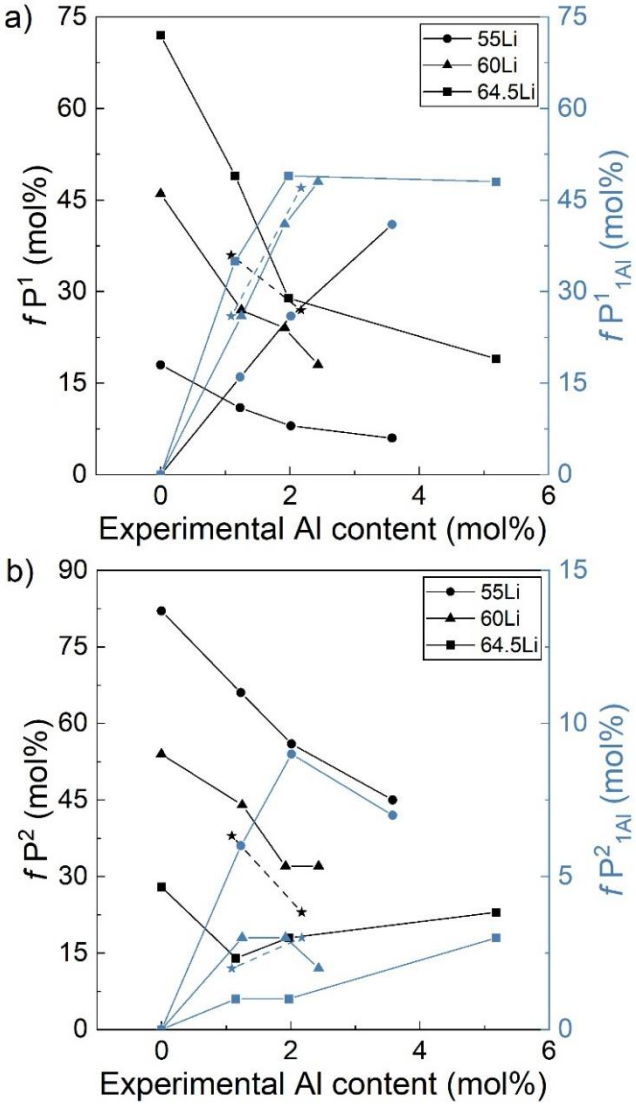

Figure 5-4. Structural unit fraction (f) as a function of experimental Al content for (a) P^1 and $P^1{}_{1Al}$ and (b) P^2 and $P^2{}_{1Al}$. The stars with dashed line correspond to de 60Li glass doped with Al_2O_3 instead of $AlCl_3$. The data were obtained from the deconvolution model shown in Figure 5-2, with parameters listed in Table S1. The lines are provided only as guides to the eye.

In an attempt to indirectly measure the consequences of Cl^- addition, we prepared an additional set of samples, starting from Al_2O_3 instead of $AlCl_3$. The resulting ^{31}P MAS NMR spectra, shown in Figure 5-5, are quite similar for both starting reagents, suggesting that Cl^- may not significantly affect the structure as much as Al^{3+} does. Minor variations in the amounts of $P^2{}_{1Al}$ can be observed; however, they are close to the limit of uncertainty. In light of the varying ionic conductivities of the Al_2O_3 and $AlCl_3$-containing samples, this observed invariance in the populations of the phosphorus short-range structural units suggests that the origin of the increased ionic-conductivity may lie in the medium-range order.

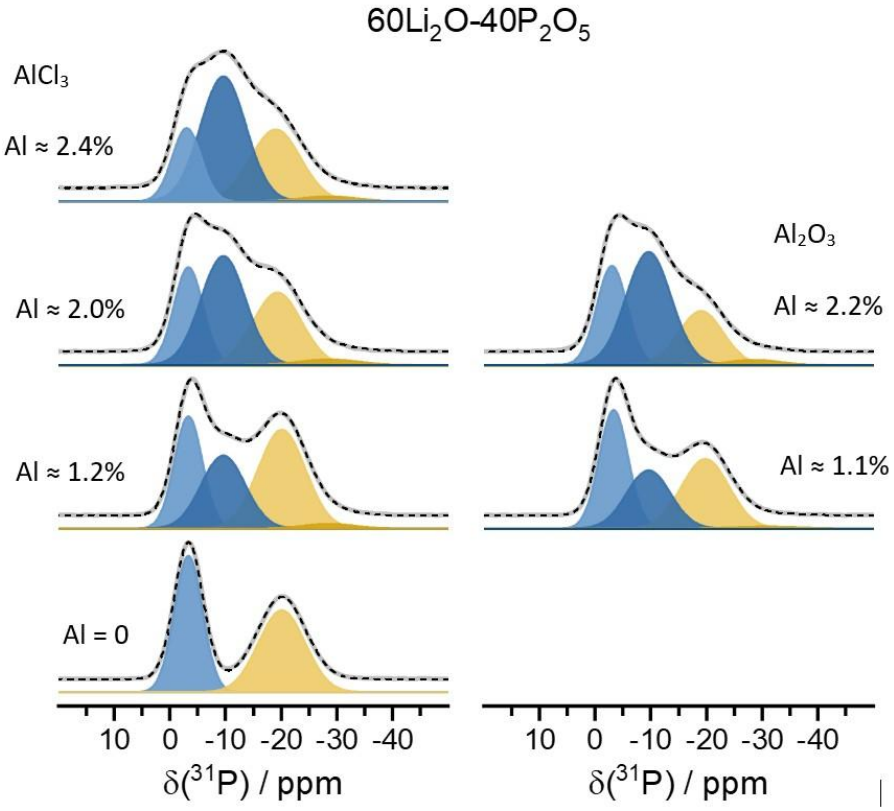

Figure 5-5. ^{31}P MAS NMR center band spectra comparison between the 60Li glass doped with AlCl3 and Al2O3. The thick gray line are experimental data, the colored solid curves are Gaussian fit components, and the black dashed line is the sum of fit components.

Figure 5-6 shows the ^{27}Al MAS NMR spectra for the glass samples in the $Li_2O–P_2O_5–AlCl_3$ system. The spectra consist of three readily discernible resonance peaks, which can be straightforwardly simulated using the Czjzek distribution model [99]. The peak at $\delta \approx 43$ ppm is attributed to four-coordinated AlO_4 units, while those near $\delta \approx 16.4$ ppm and $\delta \approx -9.2$ ppm correspond to five and six-coordinated AlO_5 and AlO_6 units [13,14], respectively. Upon closer inspection, some intensity close to the chemical shift of 66 pm can be observed, which we attribute to signals from somewhat rare $Al^4–O–Al^4$ connectivity [100,101]. The employed simulation parameters are listed in

Table S2 in appendix A.

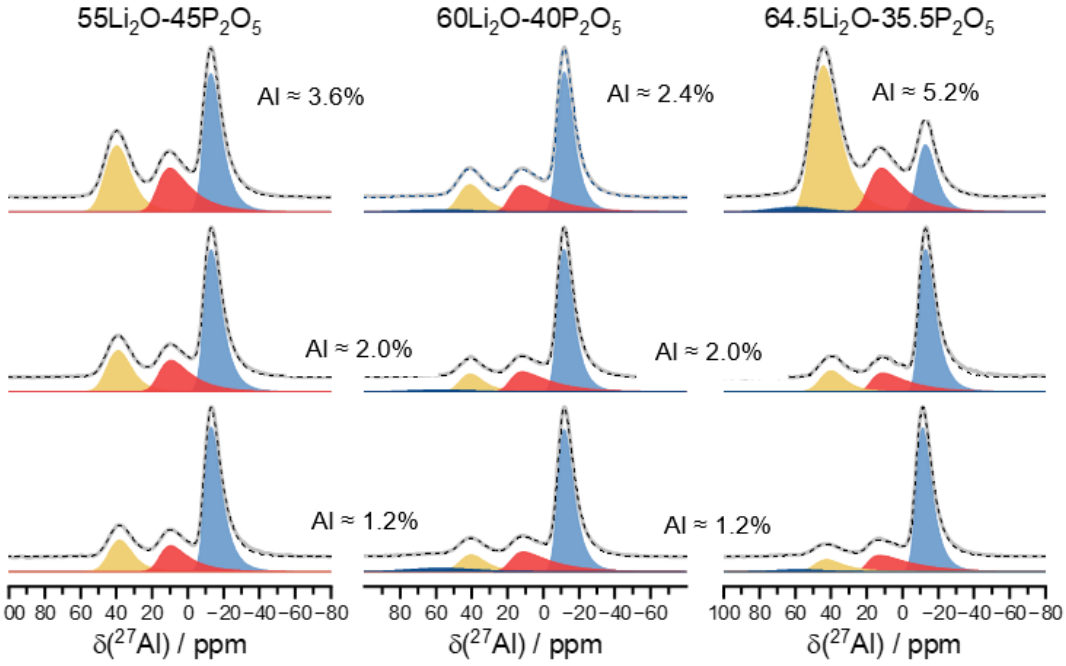

Figure 5-6. ^{27}Al MAS NMR center band spectra of the glasses under study and line shape simulations using the Czjzek model [102]. The thick gray lines are experimental data, the colored solid curves are Gaussian fit components, and the black dashed line is the sum of fit components.

Based on the Gaussian fits illustrated, Figure 5-7 shows that the fraction of aluminum species is somewhat composition-dependent: Overall, six-coordination prevails (≈ 60%), and values peak in the x = 5 compositions. On the other hand, a continuous increase of AlO_4 and AlO_5 units is observed for all

compositions as the aluminum content increases, which is a well-documented effect in the ternary Li_2O–Al_2O_3–P_2O_5 system [13,14].

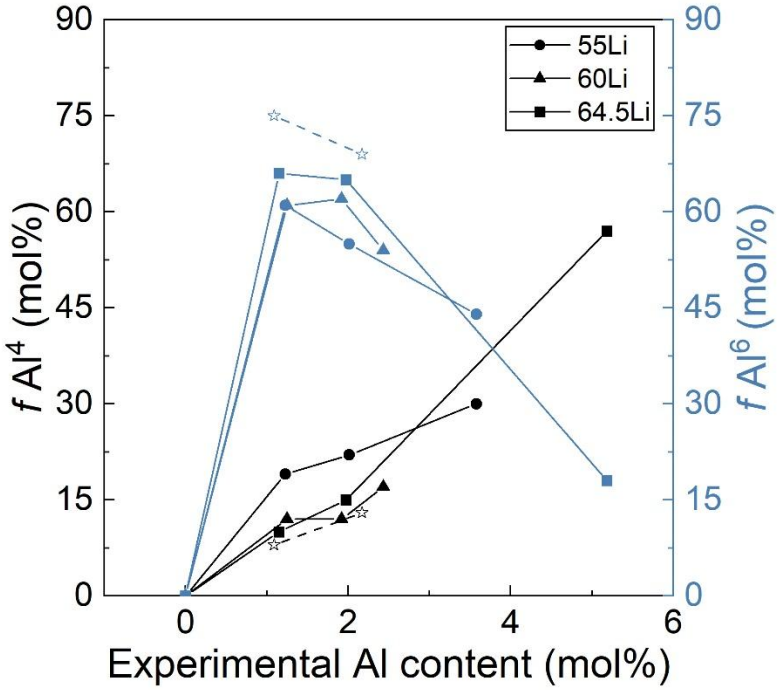

Figure 5-7. Structural unit fraction (f) as a function of experimental Al content for Al^{3+} four and six-coordinated. The open stars with dashed lines correspond to 60Li glass doped with Al_2O_3 instead of $AlCl_3$. The data were obtained from the deconvolution model shown n Figure 5-4 with parameters listed in Table S2. The solid lines are provided only as guides to the eye

5.3.4 Ionic Conductivity

The temperature dependence of the ionic conductivity for the glasses under study is shown in Figure 5-8. As expected, the Arrhenius plots reveal that the ionic conductivity directly correlates with the Li^+ concentration, and the highest ionic conductivities are observed for the glasses with the highest lithium content (64.5Li series). Within this series, however, the glass 64.5 Li-C exhibits about one order of magnitude lower ionic conductivity than the other glasses in the system, which can be attributed to partial lithium loss and the complete loss of chlorine ions, as mentioned before (see Table 5-2).

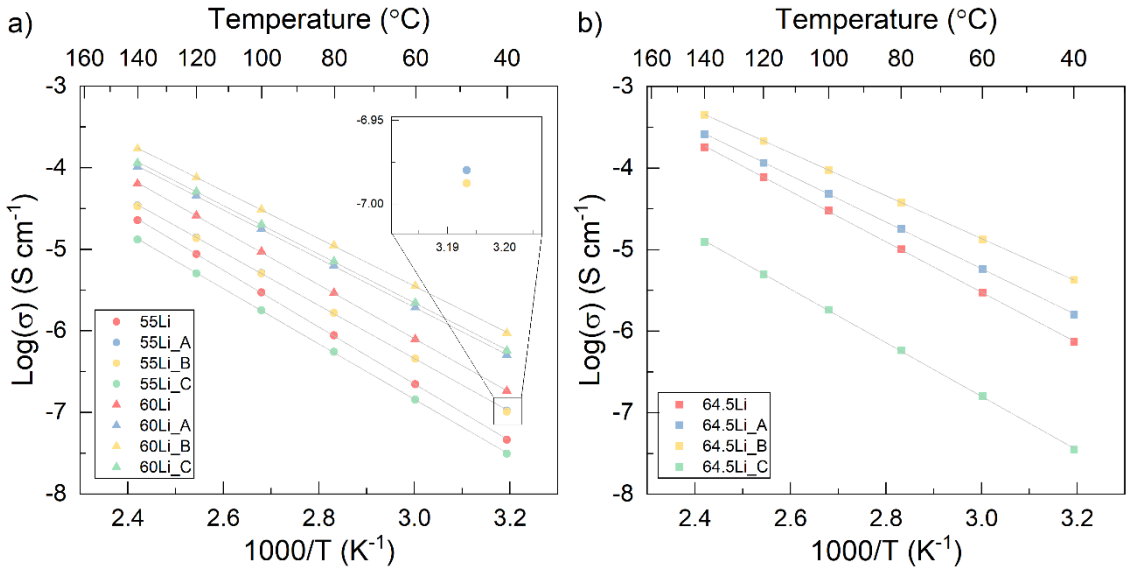

Figure 5-8. Arrhenius plots of ionic conductivity for samples from the three glass series. Solid lines are linear fits to the data following the Arrhenius equation. Left: Series 55Li and 60Li. Right: Series 64.5Li. The inset shows an expansion of the plot indicated by black lines.

To highlight the influence of Cl^- on the electrical properties of the glasses under study, Figure 7 presents, as a function of experimental chlorine content, the ionic conductivity (σ) at 100 °C, activation energy (E_a), and pre-exponential term (σ_0) of the Arrhenius equation.

$$\sigma = \sigma_0 \exp\frac{-E_a}{kT} \qquad \text{Eq. (1)}$$

The data presented in Figure 5-9 is derived from the fitting in Figure 5-8. Figure 5-9a shows a consistent increase in ionic conductivity across all three glass series with rising chlorine content. The effect is especially pronounced at higher Li/P ratios and is particularly significant given that the addition of $AlCl_3$ does not increase the Li^+ concentration. In fact, $AlCl_3$ incorporation leads to a slight reduction in the overall charge carrier density, and yet ionic conductivity improvement is seen.

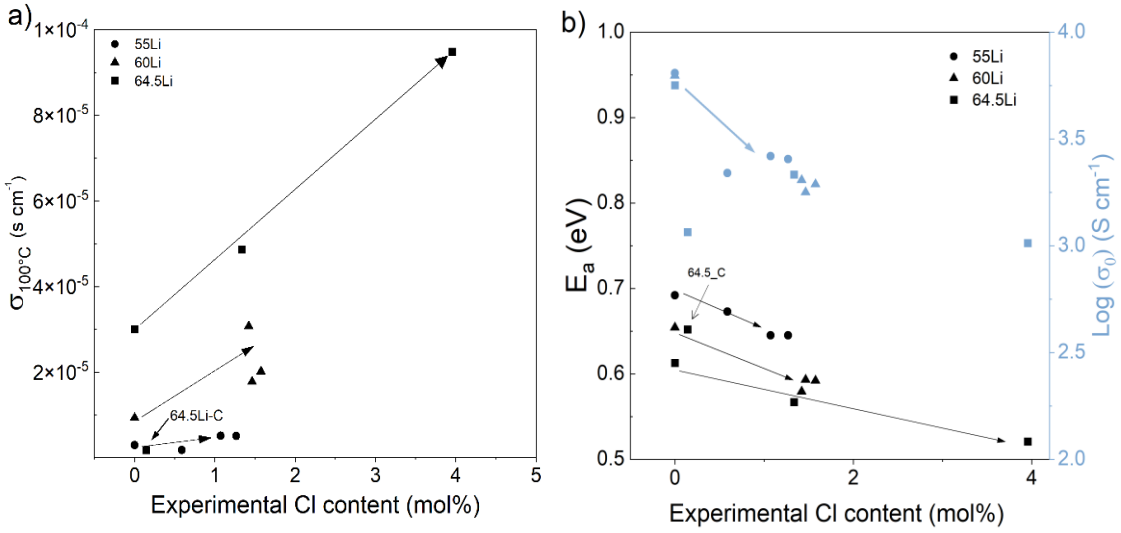

Figure 5-9. a) Ionic conductivity at 100 °C, and b) activation energy and pre-exponential factor of the Arrhenius expression, as a function of the experimental chlorine content for the investigated phosphate glasses series, with different lithium content. The arrows are presented to guide the reader's eyes.

Similarly, the incorporation of Cl^- in the base glass resulted in the reduction of the activation energy for all three series (Figure 5-9b). The lowest E_a-value observed is 0.52 eV for the glass composition 64.5-B, with the highest lithium and chlorine contents. Notably, this value is even lower than that of 0.58 eV reported for the glass $55Li_2O–15Nb_2O_5–30P_2O_5$, with a corresponding electrical conductivity of 2.7×10^{-6} S cm^{-1} at 25 °C [16], which is, to the best of our knowledge, the highest ionic conductivity reported in literature for an oxide glass.

Concerning the effect of halide ions, it is known that glasses doped with lithium halide salts, such as LiCl, LiBr, and LiI, show improved conductivity due to the change in the local ionic field through the formation of weaker Li-Cl, Li-Br, and Li-I bonds, compared to stronger Li-O bonds [21]. Results on the $Li_2O–B_2O_3–Li_2X_2$ (X = F, Cl and Br) [19] system show that in terms of the Anderson-Stuart model [28], the incorporation of Cl^- and Br^- in the glass network decreases the electrostatic and strain energy related to the activation energy, implying that both the formation of charge carrier (electrostatic) and mobility (strain) of the charge carrier is facilitated. Another work evaluating glasses in the system $Li_2X–B_2O_3–SiO_2$ (X = O, Cl_2) [20] has concluded that coulomb

interactions between charge carriers and their charge-compensating pair determines the ionic conductivity, in the sense that dilatation or size of interstitial volume is of minor importance. In light of this discussion, the observed increase in ionic conductivity suggests that even small amounts of Cl^- significantly affect the ionic environment, altering the potential energy landscape and promoting increased ionic conductivity, likely provided by lowering the binding energy, thus favoring enhancement of charge carrier density by lowering dissociation energy as proposed by the weak-electrolyte approach [10].

Additionally, the effect of chlorine loss in the 64.5Li-C sample is reflected in Figure 5-10, which shows that this glass exhibits similar ionic conductivity but has a slightly lower activation energy than that of the 55Li-C sample. Typically, lower activation energy leads to an increase in ionic conductivity. However, the pre-exponential factor of sample 64.5-C is lower than that of sample 55 Li-C (Figure 5-9b), resulting in similar ionic conductivity for both glasses. It is interesting to note that the pre-exponential factor of all three series of glasses shows a reducing trend as the chlorine content increases.

The pre-exponential factor may be written as [103]:

$$\sigma_0 = n_t \frac{e^2 \lambda^2 \nu}{6 k_b T} \exp\left(\frac{\frac{\Delta S_f}{2} + \Delta S_m}{k_b}\right), \qquad \text{Eq. (2)}$$

where n_t is the density of the total charge carriers, λ is the hopping distance, n is the jump attempt frequency, ΔS_f and ΔS_m are the contributions from the formation and migration entropy, k_b and T have their usual meanings.

Given that the glasses 55Li-C and 64.5Li-C exhibit comparable lithium and chlorine content, as well as similar densities, it is reasonable to assume that parameters such as n_t, λ, and ν remain approximately constant between the two compositions. Therefore, the observed difference in σ_0 between these samples can be attributed to entropic contributions.

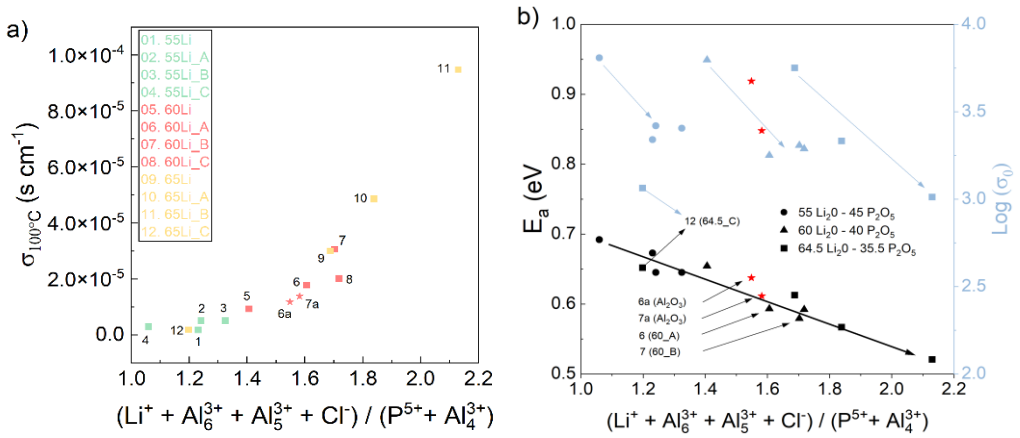

Figure 5-10. The ionic conductivity of the glass series Li_2O–$AlCl_3$–P_2O_5 at 100 °C as a function of the ratio of Li^+, AlO_6, AlO_5, and Cl^- over P_2O_5 and AlO_4. The red stars correspond to the glasses made from Al_2O_3 precursor and composition (100-*x*)(6 Li_2O–40P_2O_5)*x*$AlO_{1/2}$, (with *x*=5 and 10), which correspond to the same aluminum content as glass compositions 6 and 7.

It is also important to consider the positive mixed former effect between Al_2O_3 and P_2O_5 [14,27]. It is known that glass modifiers introduce non-bridging oxygen into the glass network, which may improve ionic conductivity, allowing alkali ions to jump from one non-bridging oxygen to another. To account for the combined effect of all network species and chlorine, we investigated several correlations of the ionic conductivity versus different ratios of the network species. Figure 5-10 depicts the result of our best effort, namely the correlation of the ionic conductivity at 100 °C, as well as the activation energy and the pre-exponential factor log σ_0, with the ratio of the sum of Li^+, Cl^-, as well as AlO_5 and AlO_6 divided by the sum of the concentration of P_2O_5 and AlO_4. Also, to differentiate the influence of Al^{3+} from that of Cl^- on the glass behavior, glasses with Al_2O_3 instead of $AlCl_3$ were also displayed. In this case, Al_2O_3 is written as $AlO_{3/2}$ to ensure the same final Al/P ratio. Comparatively, glasses containing $AlO_{3/2}$ showed only a modest (1.5×) increase in their ionic conductivity, against a 3.2× increase with $AlCl_3$. This fact confirms that Cl^- anions play a more significant role in enhancing ionic conductivity, likely by weakening Li–O bonds, than the structural effects from the mixed former (Al_2O_3/P_2O_5) environment.

These findings support the view that halide doping promotes more favorable conduction pathways for Li^+ in the glass matrix.

5.4 Conclusion

Glasses were synthesized in the $Li_2O–P_2O_5–AlCl_3$ system under ambient conditions, revealing that higher Li_2O/P_2O_5 ratios enable greater incorporation of $Cl^–$ into the glass. An increase in *T*g values was observed with the addition of $AlCl_3$, attributed to the incorporation of cross linking $AlO_{4/5/6}$ species. Solid-state NMR spectroscopy also reveals that aluminum incorporation leads to the introduction of Al-O-P bonds. It was observed that the presence of chloride anions provokes a clear decrease in the activation energy for ionic conduction, resulting in an increase in the ionic conductivity for all three series of glass. The highest conductivity, 1.6 × 10-6 S.cm-1 at 25 °C, was obtained for the 64.5-B sample and is among the highest ones reported for oxide glasses. In fact, chlorine-free glasses with nearly the same lithium and aluminum content as some chlorine-containing glasses exhibited lower ionic conductivity and higher activation energy, despite having a slightly more depolymerized structure. It is worth noting that the addition of $AlCl_3$ to the base glass does not introduce new cationic charge carriers, such as Li^+. Thus, the observed increase in conductivity stems from a synergistic effect between chlorine anions and glass network rather than from a simpler addition of charge carriers or a positive-mix glass-former effect. Overall, these findings demonstrate that the incorporation of different anions can effectively decouple ionic conductivity from both charge carrier concentration and degree of glass polymerization, presenting study offers new insights into the design of solid electrolytes.

CHAPTER 6 – SOLVENT-FREE PHOTO-CROSS-LINKED GLASS-POLYMER ELECTROLYTE FOR SOLID-STATE BATTERIES

6.1 Introduction

The global energy transition has pushed many areas to address sustainability in their chain, such as energy generation by incorporating increasingly more renewable energy generation in their portfolio, as well as transportation by the electrification of mobility. In this way, energy accumulators, such as batteries, are key technologies. The next generation of batteries, called all solid-state batteries (ASSB), are promising technologies in terms of safety and energy density [104]. As a result, much attention has been given to solid-state electrolytes, which lie at the heart of the solid-state battery concept.

Polyethylene Oxide (PEO) based solid polymer electrolytes have been extensively studied because they are lightweight, easy shaping, have good processability and mechanical flexibility [105]. This last advantage is important to accommodate volume change from electrodes upon cycling and retention of interfacial contact. However, their ionic conductivity around 10^{-7} to 10^{-5} S cm^{-1} at room temperature has been their major drawback [106]. Inorganic solid electrolytes can achieve up to 10^{-2} S cm^{-1} for sulfides [107] and halides [108], which is comparable to liquid systems. However, they usually lack stability with Li and are highly sensituve to air and may decompose into toxic gases [109]. On the other hand, oxides solid electrolytes like LLZO, LAGP and LATP [110], are much more electrochemically stable and can reach up to 10^{-4} to 10^{-3} S cm^{-1} [111]. However, due to their brittle nature, high interfacial contact resistance and inability to accommodate volume expansion they are not suitable for practical application [104].

Therefore, composite solution (polymer + ceramic filler) has shown great results by combining the advantages of each material and mitigating its disadvantages [112]. For instance, ceramic fillers have shown an improvement in electrochemical stability when compared to bare PEO [113]. The plating and

striping behavior of composite materials are more stable and withstand higher currents until failure [114]. The ionic conductivity can also be improved by the incorporation of solid electrolytes, the most used is LLZO based solid electrolytes [115,116], although this property is still controversial [114,117]. All these effects when combined result in overall increase in cell performance. Glassy solid electrolytes have some advantages such as processing, chemical tunning, absence of grain boundaries and their lighter weight compared to crystalline state.

The classical route of making such composite materials is usually casting method, that is dissolving polymer matrix in toxic solvents (usually acetonitrile), with cation salt and inorganic filler. Greener solution was already proposed such as dry mixing and hot calendering [118,119]. Another interesting solution is by UV polymerization, commonly used for gel polymer electrolytes [120–122], but also employed in solid polymer electrolytes [122–124], where a monomer is used as liquid phase to homogenize all materials and then polymerized by UV radiation.

In this work we explored a solvent-free UV photopolymerization synthesis of composite solid electrolyte based on PEGDA polymer, LiTFSI and three different ceramic fillers: glassy 64.5 Li_2O – 35.5 P_2O_5 (LP) and 50 Li_2O – 30 Nb_2O_5 – 20 P_2O_5 (LNbP), and amorphous LiPON (LPN – $Li_9P_3O_9N_2$). Additionally, solid state batteries based on $LiFePO_4$ cathodes were also assembled to evaluate the electrochemical performance of the composite electrolytes synthesized.

6.2 Material and Methods

6.2.1 Glass Synthesis and Preparation

Lithium conductive glasses from 64.5 Li_2O – 35.5 P_2O_5 (LP) and 50 Li_2O – 30 Nb_2O_5 – 20 P_2O_5 (LNbP) were obtained through the melt and quench technique in a 20 g batch. Proper amounts of Li_2CO_3 (Sigma Aldrich, ≥99,0%), Nb_2O5 (CBMM, ≥99.99%) and $NH_4H_2PO_4$ (Sigma Aldrich, ≥98%) were mixed in a high-speed mixer (FlackTek™) for 3 times 3 minutes at 1700 RPM. The mixture was calcinated at 800 °C for 1 h using an electric furnace (Deltech DT-33-RS-812-C) to release volatiles such as ammonia, water, and carbon dioxide from the starting reagents. After calcination, the temperature was raised to 1100 °C for melting compositions with Nb_2O_5 , while for binary system the temperature was lowered to 600 °C in order to reduce the viscosity for quenching. After 1 hour of dwell time, the melt was splat-cooled between two stainless steel plates. The glass was not annealed because it shreds on cooling.

Glassy samples were sorted out from the batch, because these glass compositions are in the limits of the glass forming ability using melt and quench technique, and, as a result, devitrified parts were present and removed. The fully glass pieces were further dry milled in planetary mill (Pulverisette 7 premium line, Fritsch), using an airtight zirconia jar with 5mm zirconia balls as grinding media that was enclosed inside a glove box with O_2 and H_2O < 1ppm (UNILab Pro, MBRAUN). A total of 6 cycles of 5 minutes at 300 RPM with 5 minutes rest between cycles and 20:1 loading (ball weight: glass weight) were used, totalizing 1h of milling process. Since Nb-doped composition exhibits glass transition temperature (T_g) about 190 °C higher than LP compositions, and thus increasing its resistance to possible crystallization due to heat produced through dry grinding process. For the Nb-doped samples ball milling process, only the glass that adhered to the jar wall was collected through gently scratching with a Teflon spatula. After that, more glass flakes were added to account for weight difference, and the jar was sealed and transferred to

pulverize once again. This process was done 8 times until 2g of LNbP powder was obtained.

LiPON (LPN – $Li_9P_3O_9N_2$) was prepared by amorphization of 3 $LiPO_3$ – 2 Li_3N via ball milling process using a FRITSCH Mini-Mill PULVERISETTE 23, that, instead of grinding through rotation and revolution as planetary mill, its grinding bowl performs vertically oscillating movements. For this synthesis, it was used 50 oscillations per minute during 6 hours at 9 mm oscillating amplitude four times, adding up to 24 hours milling process [125]. After synthesis process, the powder was grounded in agate mortar to break major agglomerates due to its high reactivity and screened in a 20 μm mesh for further use.

6.2.2 Composite Electrolyte Synthesis

The composite solid electrolyte (CSE) synthesized in this work was prepared by overnight mixing in a magnetic stirring polyethylene glycol diacrylate (PEG600DA) (Sartomer, 708 g/mol), lithium salt (Lithium bis(trifluoromethanesulfonyl)imide - LiTFSI, Solvionic ≥99.9%) in different molar concentration (EO:Li = 10:1, 20:1, 25:1, 30:1 and 40:1) and glass powder in different weight percentage (2.5, 5 and 10%wt). After that, 2,2-dimethoxy-2-phenylacetophenone (DMPA) (Sigma-Aldrich, ≥99%) was added as a photoinitiator, mixed four another hour and then the solution was transferred to centrifugal planetary mixer (Kakuhunter, SK-300SII) for 10 minutes at 1500 RPM, followed by 5 minutes at 1000 RPM to break agglomerates and degas the solution to eliminate bubbles. The solution was then transferred back to the glovebox, where it was dispersed in stainless steel mold with 200 μm thickness and polymerized by UV photopolymerization using K-ILU 2 UV lamp (KLOÉ) at 365 nm with UV-LED with a collimated beam in continuous mode for 10 seconds. The solid polymer electrolyte (SPE) was prepared the same way but without any addition of glass powder filler for comparison.

The flowchart in Figure 6-1 summarizes the synthesis methodology for the solid electrolyte developed in this study. Route A corresponds to the

preparation of the glassy material, Route B to the synthesis of amorphous LiPON, and Route C to the combined processing of all reagents to produce free-standing solid-electrolyte membranes, which were punched into 7 mm discs for characterization.

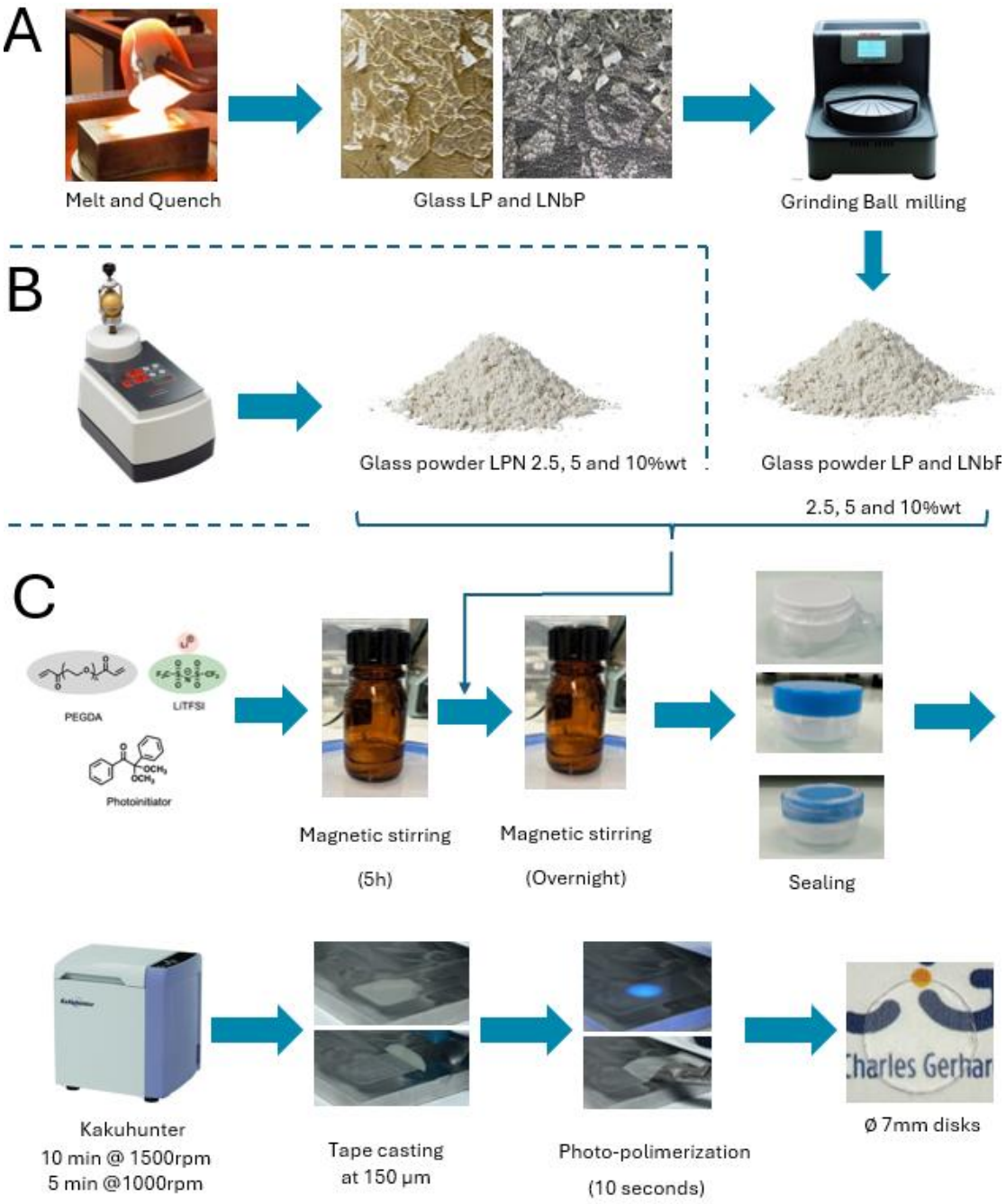

Figure 6-1. Flowchart of the methodology used in the work to synthesize the composite solid electrolytes under study.

6.2.3 Composite Electrode Synthesis

The solid-state cathode was prepared using lithium iron phosphate ($LiFePO_4$, MTI Corporation), solid polymer electrolyte (PEO 5,000,000 g/mol – Sigma-Aldrich and LiTFSI in 20:1 EO ratio), and a carbon black Super-P (Alfa Aesar, ≥99%) in a ration 70:25:5 weight%. Firstly, LiTFSI were dissolved in anhydrous acetonitrile (ACT) by magnetic stirring for 2h. After, PEO was slowly and gradually introduced to for a viscous paste. Then, stoichiometric amounts of LFP and Super-P were ground in an agate mortar and transferred to kakuhunter cups containing PEO-LiTFSI solution. A centrifugal planetary mixer (Kakuhunter, SK-300SII) was used for 10 minutes at 1500 RPM, followed by 5 minutes at 1000 RPM for slurry homogenization. After mixing, the slurry was tape cast onto an aluminum foil and dried at 40 °C under dynamic vacuum overnight. Finally, the cathodes were punched with 6mm diameter and dried again at 40 °C under dynamic vacuum overnight to be transferred to a glove box for solid-state coin cell (CR3200) assembly. The active material loading is 2.3 mg cm^{-2}, with a theoretical capacity of 119 mAh/g.

6.3 Characterization

6.3.1 Optical and Scanning Electron Microscopy

Optical microscopy images were obtained using a Keyence VHX-S770E to analyze particle distribution. Scanning Electron Microscopy (SEM) and Energy Dispersive Spectroscopy (EDS) were performed using a Hitachi S-2600N to evaluate the dispersion and homogeneity of LiTFSI and other elements related to the glass.

6.3.2 Infrared Spectroscopy

Fourier Transform Infrared (FTIR) spectroscopy was carried out using a Nicolet iS50 FT-IR Spectrometer to identify interactions between the glass and the solid polymer electrolyte components. The shift in characteristic absorption bands was analyzed to assess possible bonding or coordination effects between these materials.

6.3.3 Differential Scanning Calorimetry

Thermal properties were investigated using DSC-Netzsch 404 at a heating rate of 10 K/min in a platinum crucible with a lid to determine characteristic temperatures of the glass composition used.

6.3.4 X-ray diffraction

X-ray diffraction (XRD) was performed to assess the non-crystalline state of the glass before and after processing: Rigaku Ultima IV X-ray Diffractometer (Cu Kα, 2θ range: 10°–65°, 40 kV, 20 mA, LaMaV) was used to verify the samples´s amorphous nature after sorting out the fully amorphous glass pieces; Malvern Panalytical X-Pert (Cu Kα, 2θ range: 10°–65°, ICGM) was used to confirm that ball milling did not induce crystallization due to temperature rise during dry milling, since the glass transition temperature of theses glasses are under 300 °C.

6.3.5 Electrochemical Performance

Impedance Spectroscopy was used to analyze the ionic conductivity of glass, solid polymer electrolyte, and composite polymer electrolyte. Measurements were conducted using Novocontrol Alpha-A High-Performance Frequency Analyzer for glass samples and BioLogic VSP potentiostat (ICGM) was used to evaluate ionic conductivity of polymer and composite electrolyte using an airtight sample holder that was enclosed inside the glovebox. Data fitting was performed using ZView software.

Linear Sweep Voltammetry (LSV) was performed using a BioLogic VSP potentiostat (ICGM) to determine the electrochemical stability window at a scan rate of 0.1 mV s^{-1} at 60°C. For each composition two cells (Li/CSE/SS) were assembled to independently measure the cathodic and anodic sweep from open circuit potential.

Plating and stripping measurements were conducted in half-cell Li/CSE/Li configurations at 60°C using Neware BTS4000. The experiments included a current step increase method to determine the critical current density (CCD) for dendrite penetration, as well as constant current cycling to evaluate the long-term stability of lithium electro deposition and dissolution.

Solid-State cell cycling was performed in Li/CSE/LFP cells at 60°C with cycling rates of 0.01C, 0.02C, 0.5C, and 1C using Neware equipment.

6.4 Results

6.4.1 Glass Thermal Properties and Non-Crystalline State

The DSC curves and Diffractograms for glass samples are shown in Figure 6-2. For the lithium phosphate glass 64.5 Li_2O – 35.5 P_2O_5 (LP), a clear glass transition temperature (T_g) appears at T_g = 320 °C, followed by a crystallization peak at T_p = 369 °C and a melting point at T_m = 647 °C. Meanwhile for the lithium niobium phosphate glass 50 Li_2O – 30 Nb_2O_5 – 20 P_2O_5 (LNbP), the characteristic temperatures shifts to higher temperature due to niobium incorporation in the glass matrix, resulting in a T_g = 510 °C, T_p = 579 °C, and T_m = 871 °C. The characteristic temperatures are consistent with literature for binary [79,80] and Nb-doped glasses [15,16,23]. The “after milling” XRD were performed because the heat produced by the dry milling of the glass could trigger crystallization on the glass samples, which did not occur.

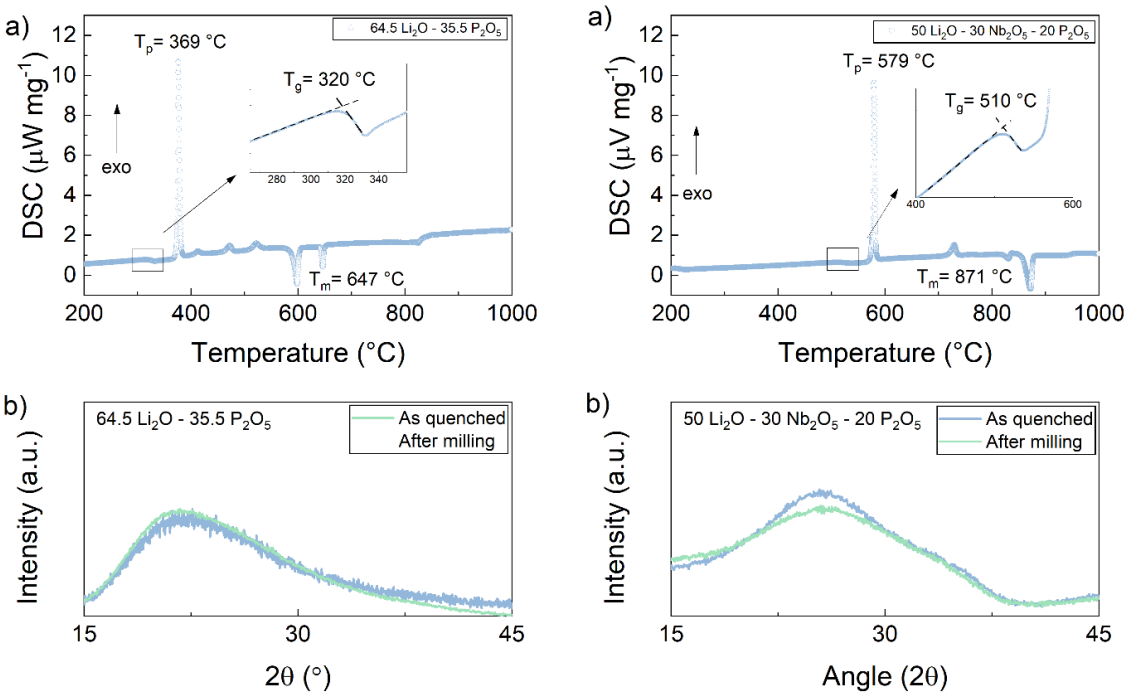

Figure 6-2. Differential Scanning Calorimetry (DSC) of bulk samples curves and XRD profile for (a) Li_2O - P_2O_5 and (b) Li_2O – Nb_2O_5 – P_2O_5

The LiPON powder was not subject to calorimetry measurements because it does not display glass transition temperature, since it was synthesized via amorphization. However, its amorphous structure can be well seen in Figure 6-3, where the XRD patterns also shows a broad diffuse halo (15–45° 2θ), characteristic of this type of material.

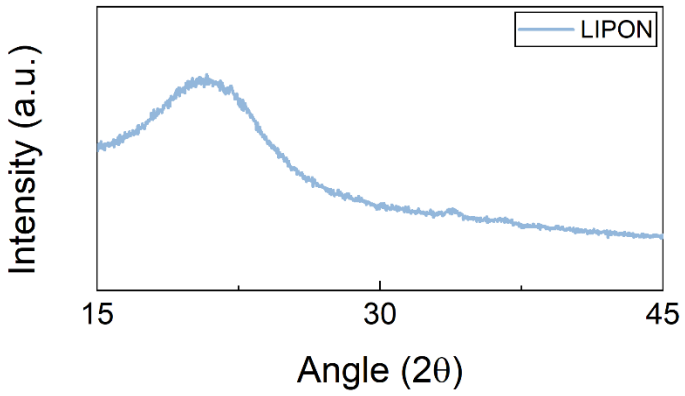

Figure 6-3. XRD profile for amorphous LIPON.

6.4.2 Macroscopic Properties

The glassy flakes (LP and LNbP) were first processed via ball milling to reduce the particle size as described hereinbefore. The LP shown in Figure 6-4a exhibits a fairly fine powder, with a tight, unimodal peak around 5–6 μm, with the width varying between 2 and 20 μm, and only a faint shoulder below 1 μm. The substantially increase in time-energy for Nb-doped sample compared to LP samples resulted in particle size for LNbP (Figure 6-4b) around 1–2 μm, with a finer particle majority between 0.5 and 9 μm. Finally, the LPN samples shown in Figure 6-4c, also exhibited particle size in the same order of magnitude at D_{50} = 3.8 μm. Note that, despite different processing methods, the D_{50} of all ceramic powders are in the same order of magnitude.

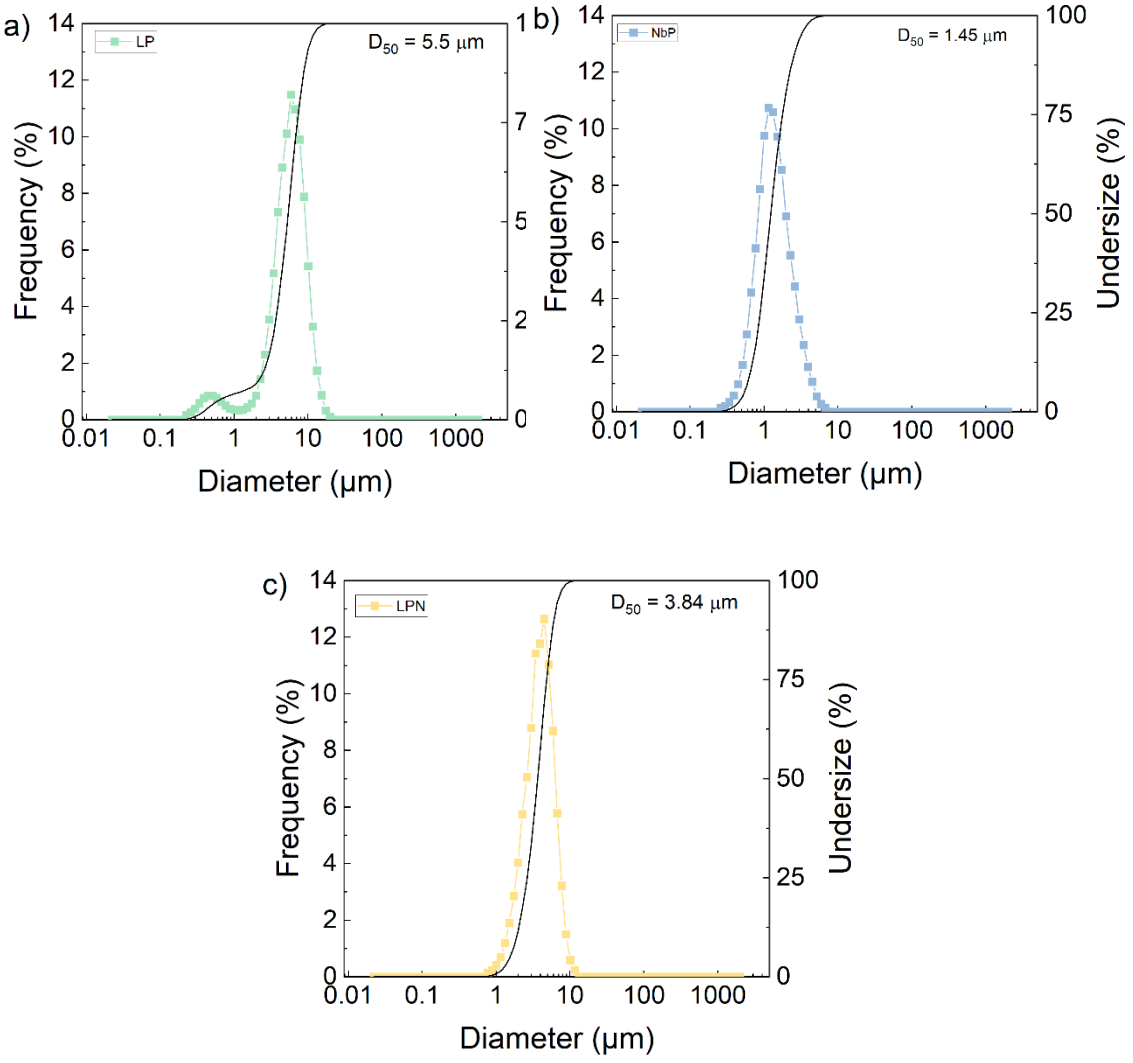

Figure 6-4. Particle-size distribution of the solid electrolytes used as ceramic filler: (a) LP, (b) LNbP and (c) LPN. The frequency and cumulative undersize versus equivalent spherical diameter. The median particle size is D_{50} is also displayed.

Figure 6-5 depicts the photograph of a free-standing solid electrolyte that was punched into 10mm diameter discs for three compositions (LP, LPN, LNbP) at increasing additive loads (0, 2.5, 5, 10%). It is observed that LP remains largely transparent across loadings, while LPN shows increasing opacity with loading and LNbP becomes progressively opaquer, appearing nearly opaque at 10%. The thickness of the membrane varied between 120 to 140 μm. The membranes exhibited good flexibility as indicated by the figure on the right, which shows that the electrolyte can be bent without cracking or breaking.

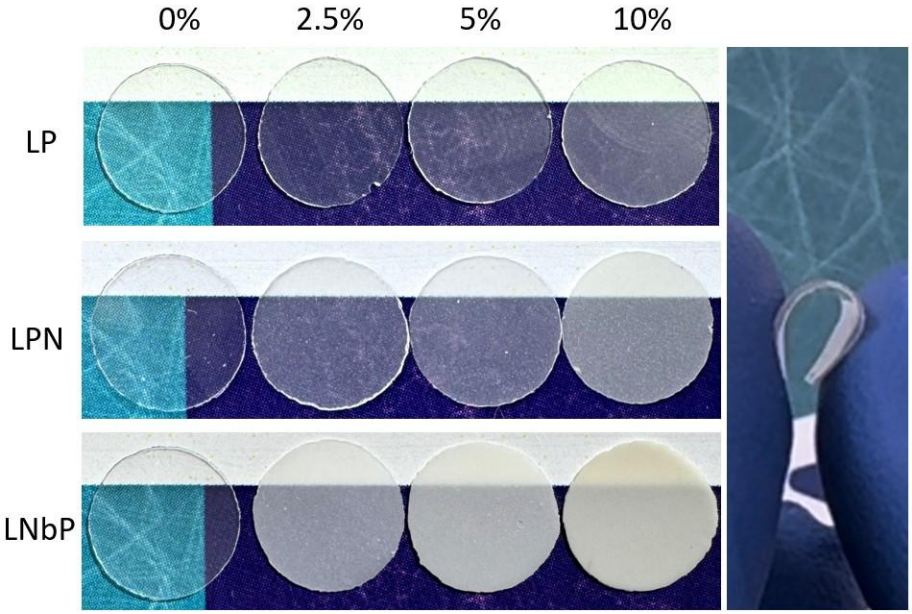

Figure 6-5. Representative 10 mm membrane discs for the three formulations (LP, LPN, LNbP) at the indicated additive load (0, 2.5, 5, and 10%). Right: example illustrating membrane flexibility under bending.

Representative optical micrographs were obtained to evaluate the particle dispersion and homogeneity of the membranes, as shown in Figure 6-6. It is possible to observe uniformly dispersed particles at all loadings for LP composition, with a size distribution as depicted by the particle size distribution (Figure 6-4). It can also be seen a few particles at about 20 μm, which was the mesh sized used for sieving the powder before mixture. Regarding the LNbP samples, there is a finer glass size distribution as compared to LP, with a few agglomerates' inclusions as can be seen in Figure 6-6. The LPN samples also exhibit clusters of agglomeration, which may be related to higher surface reactivity of LiPON compositions that adds additional challenge for breaking particles. This could be achieved by wet ball milling process, although organic solvent management should be considered [126].

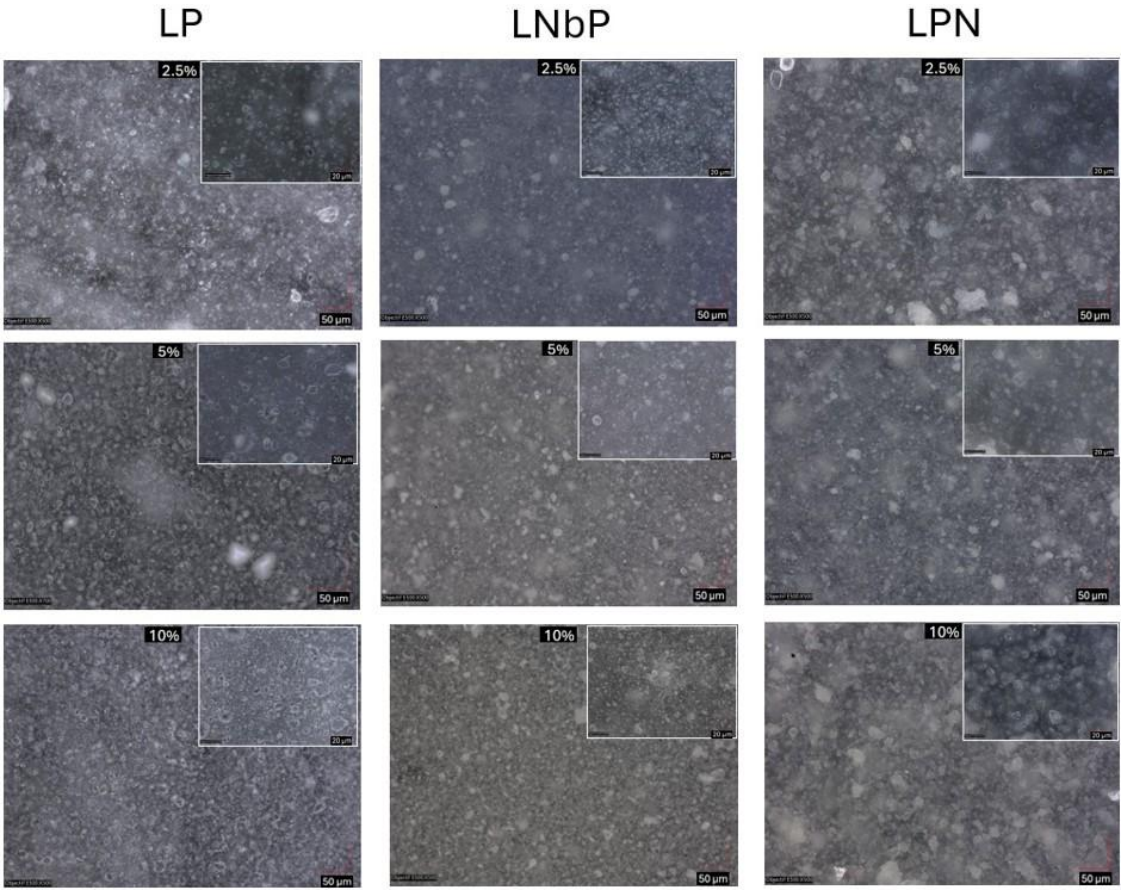

Figure 6-6. Optical micrograph of photo-cross-linked membranes as a function of glass loading. (main panels: 50 μm scale; insets: 20 μm).

Particle dispersion was also investigated by EDS mapping of S, P and Nb. Sulfur (S) is being used as reference for LiTFSI salt distribution. As can be seen in Figure 6-7, the S distribution seems homogenous indicating good solvation of LiTFSI. With respect to the P and Nb (Figure 6-0-8), the same features as described in Figure 6-6 an be observed, that is, good dispersion of Li_2O – P_2O_5 system with absence of agglomeration, while samples doped with Nb exhibit a few agglomerates. Regarding the Nb, the higher agglomeration can be related to the finer powder that naturally tends to agglomerate as well as for LPN powder.

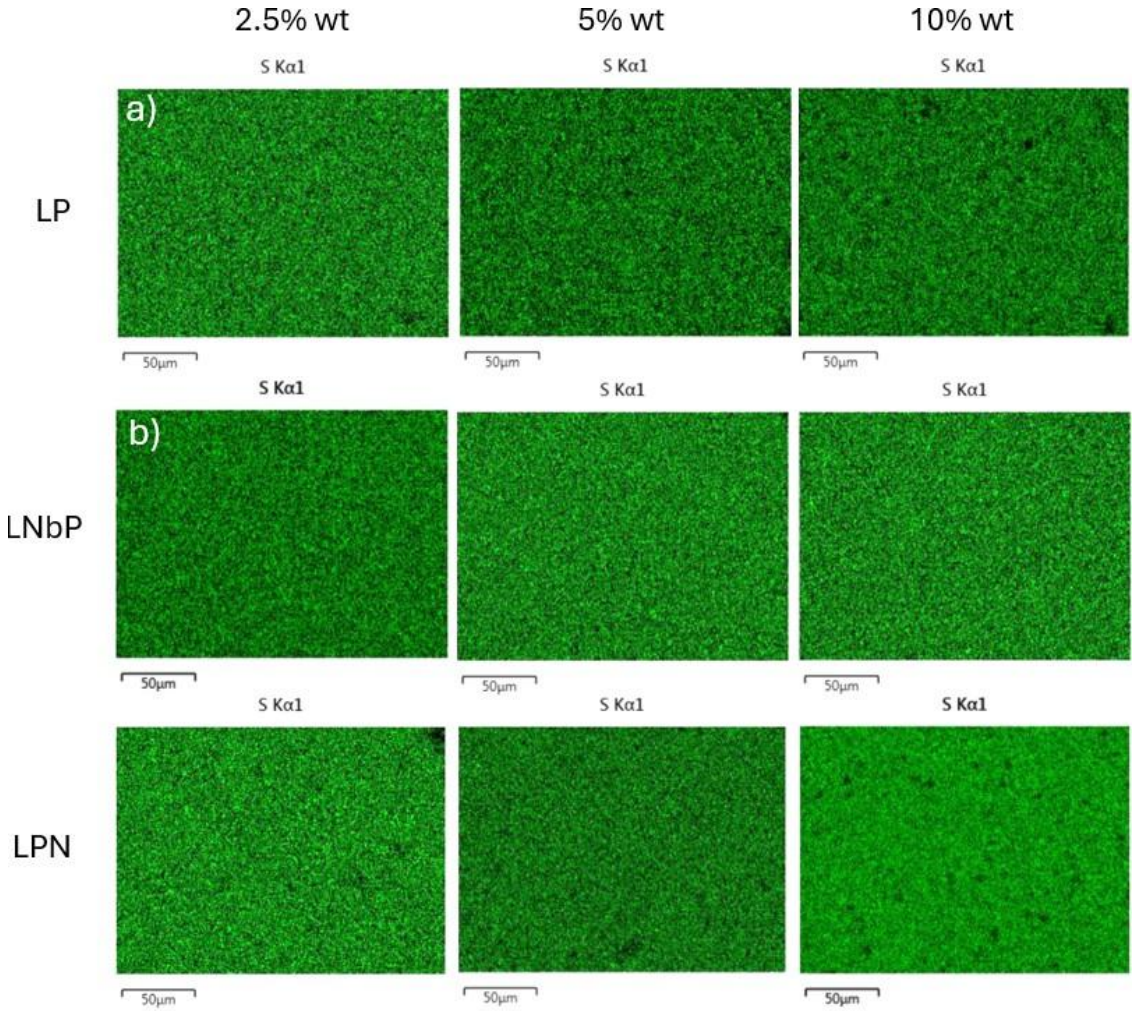

Figure 6-7. Energy-dispersive X-ray spectroscopy (EDS) elemental mapping of sulfur (S Kα1) for polymer matrices with different filler loadings. (a) LP-based composites and (b) LNbP-based composites and (c) LPN-based composites containing 2.5 wt%, 5 wt%, and 10 wt% of ceramic filler as indicated on the left side. The green contrast represents the distribution of sulfur within the samples.

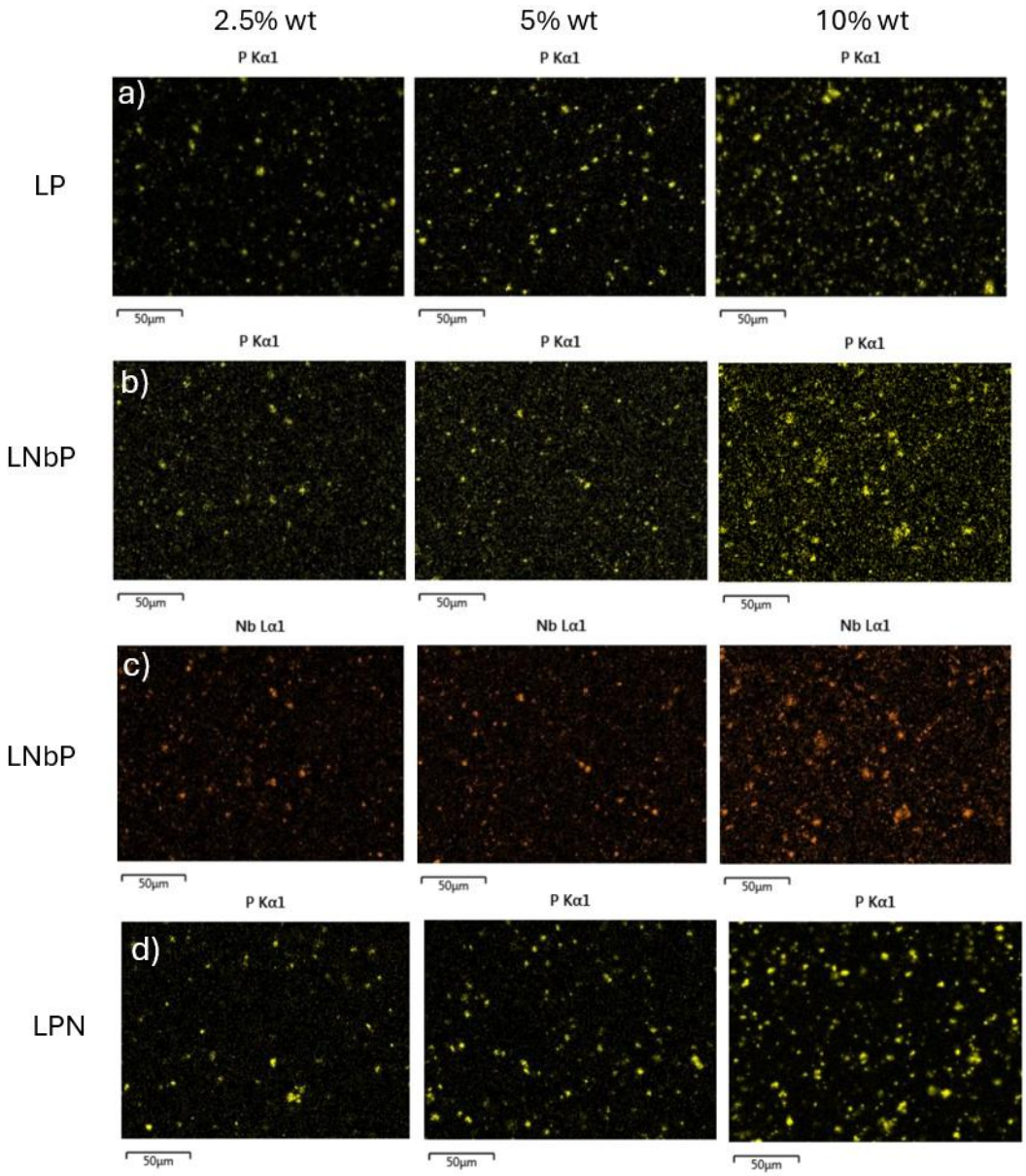

Figure 6-0-8. Energy-dispersive X-ray spectroscopy (EDS) elemental mapping of phosphorus (P Kα1) and niobium (Nb Lα1) for polymer composites with different additive loadings. (a) P-element distribution in LP-based composites and (b) P-element distribution in LNbP-based composites, (c) Nb-element distribution in LNbP-based and (c) P-element distribution in LPN-based composites, composites at 2.5 wt%, 5 wt%, and 10 wt% concentrations. The bright spots correspond to localized elemental presence, indicating dispersion of P- and Nb-containing species within the polymer matrices.

6.4.3 Fourier Transform Infrared Spectroscopy

The spectroscopic characteristics of the composite solid electrolyte were analyzed with an FTIR spectrometer in attenuated total reflection (ATR) mode, as shown in Figure 6-9. The spectra are normalized and compared to highlight chemical interactions between the polymer matrix and inorganic powders. The polymerization of the monomer during UV photopolymerization can be followed by the vanishing of the C=C peaks at around 1640 cm^{-1} and 1407 cm^{-1} [120,127], becoming a band as shown. Importantly, the FTIR spectra of all CSE samples overlap with that of the SPE, regardless of the type (LP, LPN, or LNbP) or concentration of the powder. No peak shift, peak broadening, or new absorption bands are observed, particularly in the region where the ceramic powder displays its peaks (1200–900 cm^{-1}). This suggests the absence of chemical interaction between ceramic fillers and PEGDA polymer matrix.

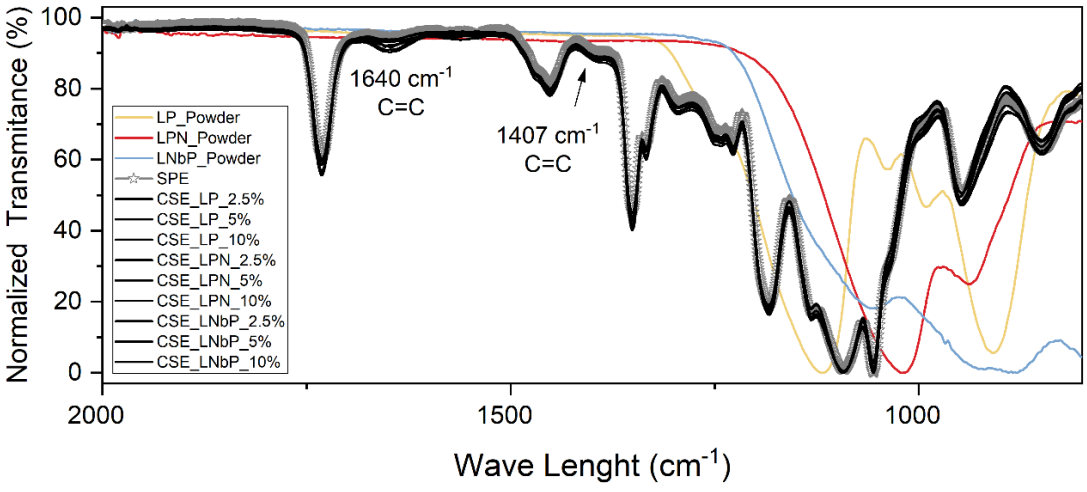

Figure 6-9. ATR − FTIR spectra of the of composite solid electrolytes under study. [120,127].

6.4.4 Ionic Conductivity

The optimal EO:Li ratio was determined, as shown in Figure 6-10a. The ionic conductivity of the solid polymer electrolyte (SPE) membrane shows the expected non-monotonic dependence on salt concentration. Conductivity rises from 6 x 10^{-6} S cm^{-1} for EO:Li = 10:1 to a maximum of 1,8 x 10^{-5} S cm^{-1} at EO:Li = 20:1, then gradually decreases as the salt concentration decreases. This trend reflects the strong LiTFSI salt interaction at higher salt concentration, promoting ion paring and clustering formation [128] that hinders conductivity until an optimal point is obtained. Afterward, at lower salt concentration, the reduction of charge carriers is responsible for the decrease in conductivity. Additionally, Figure 6-10b displays the Arrhenius plot of ionic conductivity for the bulk glasses reference and polymer electrolyte at different salt concentrations. It can be seen that glasses obey Arrhenius behavior, while polymer electrolytes display non-Arrhenius behavior consistent with chain mobility restriction at lower temperatures. This difference in thermal dependence of ionic conductivity highlights different mechanisms for each material. Finally, Figure 6-10c shows the ionic conductivity at 60 °C at fixed EO:Li = 20:1 of the PEO:LiTFSI based composite electrolyte (CSE) with different fillers composition and content. The SPE starts at $\sigma \approx 2 \times 10^{-5}$ S cm^{-1}. The incorporation of 2.5% of LP do not produce significant change in conductivity, while further doping from 5% produces a monotonic decline of conductivity, approaching the “LP–bulk glass” reference. In contrast, the conductivity of LPN composition remains roughly constant with overlapping error bars across the entire range. Similarly, LNbP delivers the highest values at all loading and is slightly beneficial with a modest

upward trend. Overall, ionic conductivity degrades with increasing LP but is essentially unchanged with LPN and LNbP.

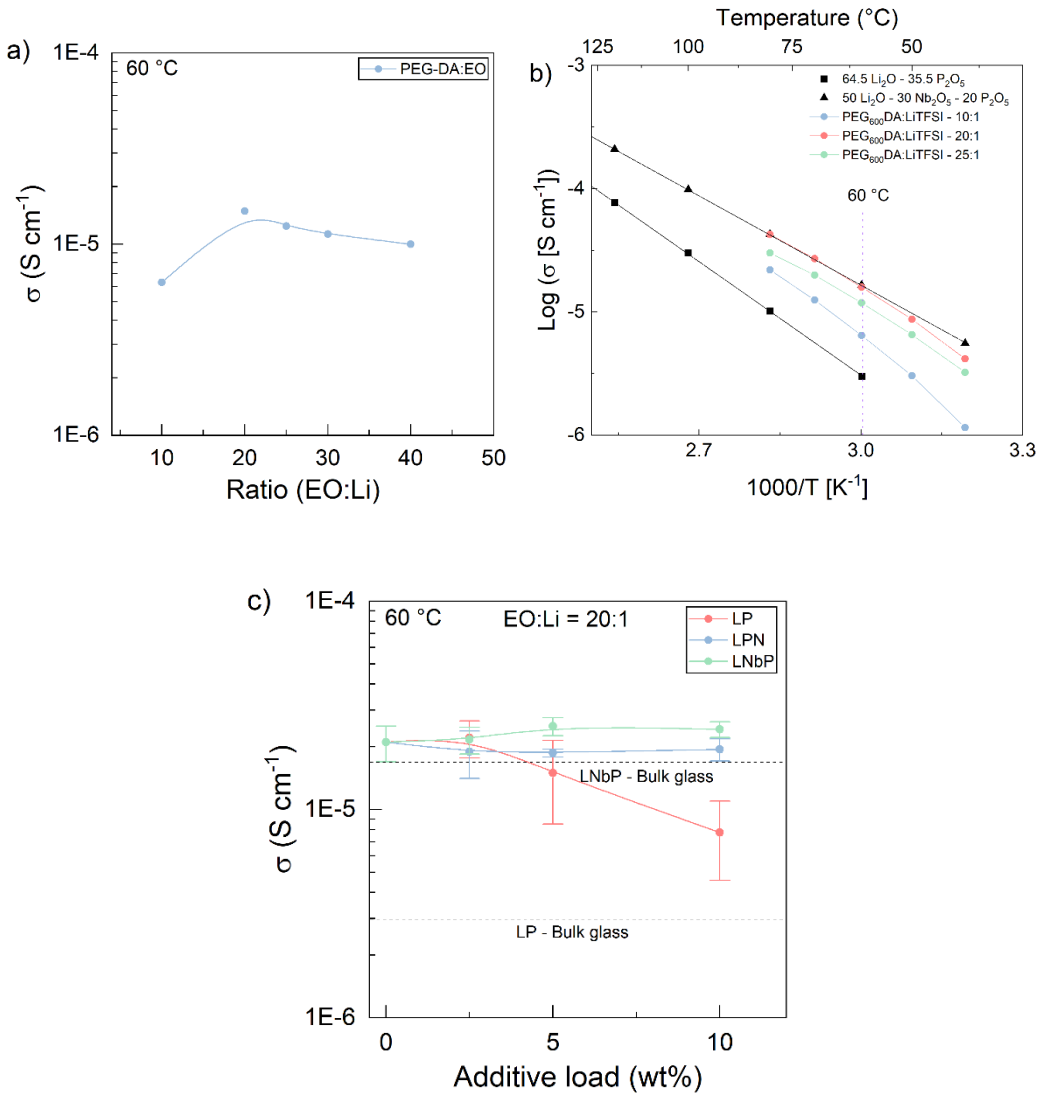

Figure 6-10. (a) Ionic conductivity at 60 °C of polymer electrolytes as a function of EO:Li ratio. (b) Arrhenius plots of ionic conductivity for PEG-based systems with varying EO:Li ratios and comparing reference of lithium phosphate and niobium-phosphate glass electrolytes. (c) Ionic conductivity at 60 °C versus inorganic additive load (0–10 wt%) for LP, LPN, and LNbP containing PEG-based electrolytes at fixed EO:Li = 20:1. Lines are guide to the eyes.

It is worth mentioning that the overall ionic conductivity of this system can be improved by employing plasticizers such as succinitrile [124]. Additionally, further studies are needed to understand better the effect of ceramic fillers and processing methods effect on the ionic conductivity. For instance, in the case of PEO based solid electrolytes, one can find articles on very similar systems in which increases [115] and decreases [114] in ionic conductivity were reported. Furthermore, although there is no consensus on the mechanism, a few studies attribute the enhancement of ionic conductivity to increased amorphous region in composite films [129], creation of new Li pathways through ceramic phase [130], increased free volume for PEO segmental motion [115], and interfacial conduction between polymer and ceramic filler [113].

6.4.5 Chemical Stability

Impedance plots at 25°C on Li||Li symmetric cells, as shown in Figure 6-11, reveal differences in interfacial aging behaviors across compositions. Indeed, the evolution of semicircle size reveals differences in the growth of the interfacial resistance, indicating composition-dependent stabilization or degradation of the Li/electrolyte interface during rest. The SPE shows (Figure 6-11a) a rapid growth of the low-frequency semicircle with time (Day 1 to day 45), in other words, monotonic increase of the interfacial resistance. The introduction of LP fillers changes the interfacial behavior. At 2.5 wt% of LP (Figure 6-11b), day 1 starts with an exceptionally large initial impedance, but the impedance reduces over time, suggesting formation/relaxation of a more conductive passivation layer. The 5 wt% LP CSE (Figure 6-11c) is the most stable, starting with small impedance, remaining nearly stationary over time. At 10 wt% LP (Figure 6-11c) behaves similarly, with initial low impedance and decreasing slightly over time. Overall, LP fillers suppress the time-dependent rise of interfacial resistance seen in the SPE, delivering an chemically stable Li interfaces most likely enable by Li_3P formation [131].

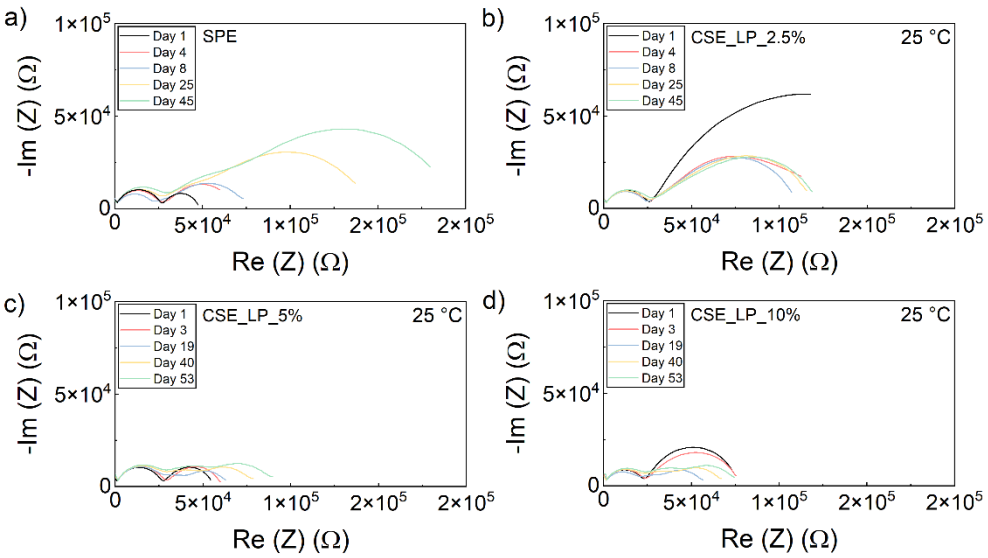

Figure 6-11. Nyquist plot of electrochemical impedance data of Li||Li symmetric cells at 25 °C showing interfacial aging behavior for (a) solid polymer electrolyte (SPE) and composite solid electrolytes (CSE) containing lithium-phosphate glass (LP) filler at (b) 2.5 wt% LP, (c) 5 wt% LP, and (d) 10 wt%.

Similarly, Li||Li symmetric cells with LPN-filled electrolytes were investigated and results are shown in Figure 6-12. At 2.5 and 5 wt% of LPN, the interface shows a more important increase in impedance in the first 10 days, then remains relatively constant, demonstrating chemical stability. Meanwhile at 10 wt% of LPN, the interfacial resistance remains nearly stationary, with a small increase over time. This stability is also expected for LiPON composition since the formation of Li_3N [131] is expected, which is known to be highly effective for interface engineering with lithium.

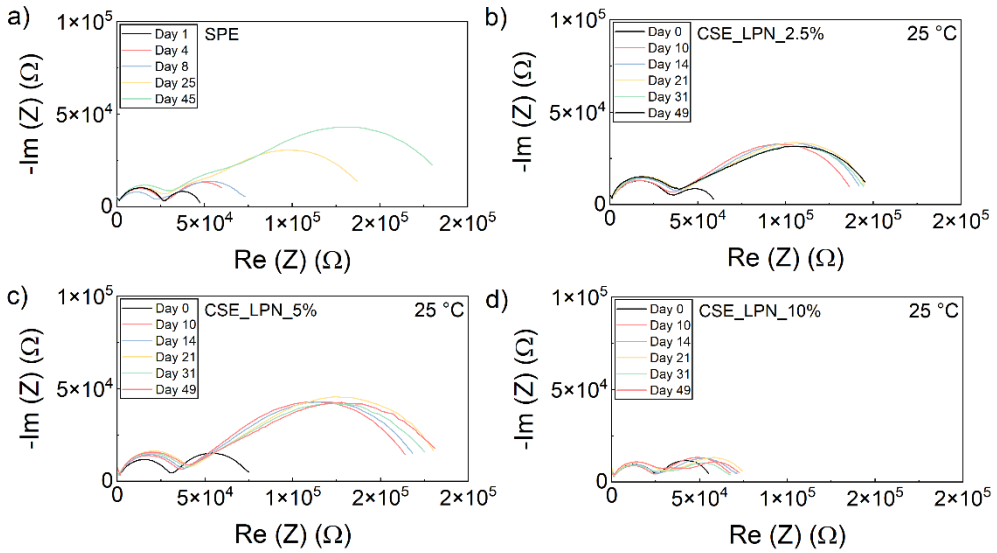

Figure 6-12. Nyquist plot of electrochemical impedance spectra of Li||Li symmetric cells at 25 °C showing interfacial aging behavior for (a) solid polymer electrolyte (SPE) and composite polymer electrolytes (SPE) containing amorphous LiPON (LPN) filler at (b) 2.5 wt% LP, (c) 5 wt% LP, and (d) 10 wt%.

In the same way, Li||Li symmetric cells with LNbP-filled electrolytes show the most benign interfacial aging of all sets, as shown in Figure 6-13. With 2.5 wt% of LNbP (Figure 6-13b), the cell displays an interfacial impedance that decreases over time. The 5 wt% LNbP CSE (Figure 6-13c) semicircles are small at the initial measurements and essentially stationary over 21 days, implying a low interfacial resistance. At 10 wt% LNbP (Figure 6-13c), the interface is initially highly resistive but decreases quickly with time.

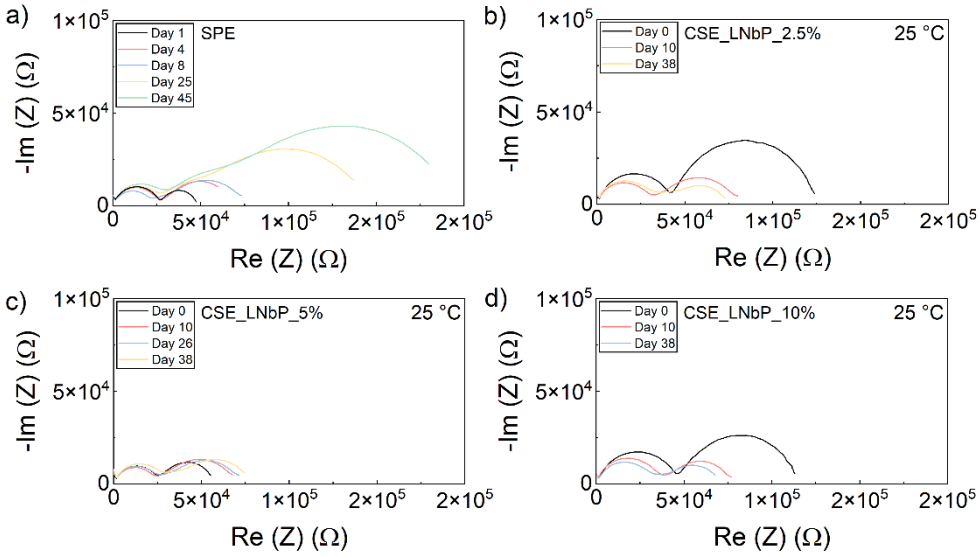

Figure 6-13. Nyquist plot of electrochemical impedance spectra of LilLi symmetric cells at 25 °C showing interfacial aging behavior for (a) solid polymer electrolyte (SPE) and composite polymer electrolytes (SPE) containing niobium-phosphate glass (LNbP) filler at (b) 2.5 wt% LP, (c) 5 wt% LP, and (d) 10 wt%.

The interfacial evolution of resistance displayed in Figures 6-11, 6-12 and 6-13 during symmetric LilLi cell aging was further analyzed using an equivalent-circuit model to decouple the individual contributions from SEI formation and charge-transfer processes, as illustrated in Figure 6-14. The impedance spectra were fit using the circuit $(R_{bulk} \parallel CPE_{bulk}) - (R_{SEI} \parallel CPE_{SEI}) - (R_{ct} \parallel CPE_{ct})$, enabling isolation of the solid–electrolyte interphase resistance (R_{SEI}) and charge-transfer resistance (R_{ct}). Figure 6-14 shows that SPE exhibits continuous increases in both R_{SEI} and R_{ct}, indicative of ongoing SEI thickening and increasing interfacial polarization during prolonged contact with Li metal up to 60 days. In contrast, composite polymer electrolytes incorporating lithium-phosphate-based fillers display a stabilization of SEI formation, as well as promoted a decrease in charge transfer resistance, especially sample CSE_LPN_10%, highlighting the stabilized interfacial chemistry provided by ceramic fillers. These results suggest that the inorganic glass phases contribute to enhanced interfacial stability, likely through improved Li-ion transport

pathways and modified interphase composition, thereby reducing uncontrolled passivation and preserving efficient Li plating/stripping over extended storage.

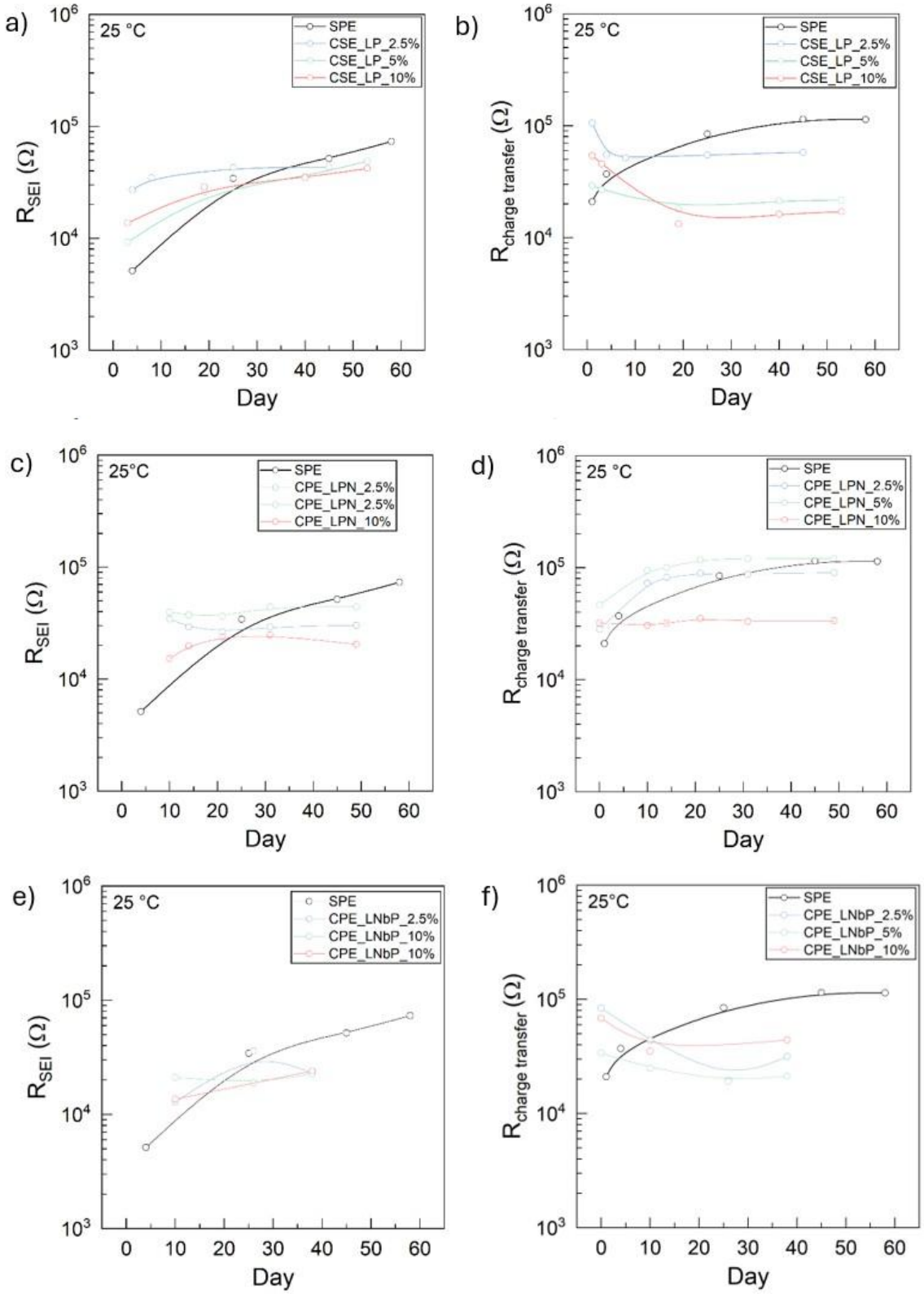

Figure 6-14. Interfacial resistance evolution in Li‖Li symmetric cells at 60 °C for solid polymer electrolyte (SPE) and composite polymer electrolytes containing inorganic fillers. Panels (a), (c), and (e) show the evolution of solid electrolyte interphase resistance (R_{SEI}) over aging time, respectively for LP, LPN and LNbP samples, while panels (b), (d), and (f) show corresponding charge-transfer resistance (R_{ct}).

6.4.6 Electrochemical Analysis

6.4.6.1 Electrochemical Stability Window

The electrochemical stability of electrolytes under study was also evaluated by linear sweep voltammetry. Results are shown in Figure 6-15. It is widely known that ceramic filler in polymer matrix results in improved oxidation potential when compared to bare polymer [113]. This behavior can also be seen in this study. For example, in Figure 6-15a the SPE exhibits oxidation potential at around 4 V vs Li/Li^+, which is the same potential where PEO is reported to be decomposed [115,116]. However, the addition of ceramic filler gradually decreases the oxidation currents and pushes the potential to higher values at 4.2, 5.25 and 5.4 V vs Li/Li^+ for 2.5, 5 and 10 wt% of LP glass, respectively. Regarding the Nb doped glass Figure 6-15b, small onset oxidation currents can be seen at around 4 V vs Li/Li^+ for CSE, indicating possible oxidation of oxygen although it is significant less pronounced than that of SPE. Similarly for LPN doped samples Figure 6-15c, it is possible to observe that ceramic filler mitigates the oxidation currents compared to SPE, pushing the potential up to 5V vs Li/Li^+ for 10 wt% of LPN. On the other hand, common behavior can be seen for all compositions regarding the reduction potential. While a peak shoulder can be seen at 0.7 V vs Li/Li^+ for SPE, which is related to the decomposition of LiTFSI, there is the appearance of a new peak at 1.5 V vs Li/Li^+ for all compositions. This can be related to the decomposition of phosphorus in the glassy matrix which is expected to form stable SEI based on Li_3P [131]. The formation of a stable SEI is the reason for choosing phosphate-based glass matrixes. It is also expected

for LPN CSE to also form Li_3N [131], since nitrates are widely known to help the formation of SEI layers that contribute for homogenous lithium plating and striping stability.

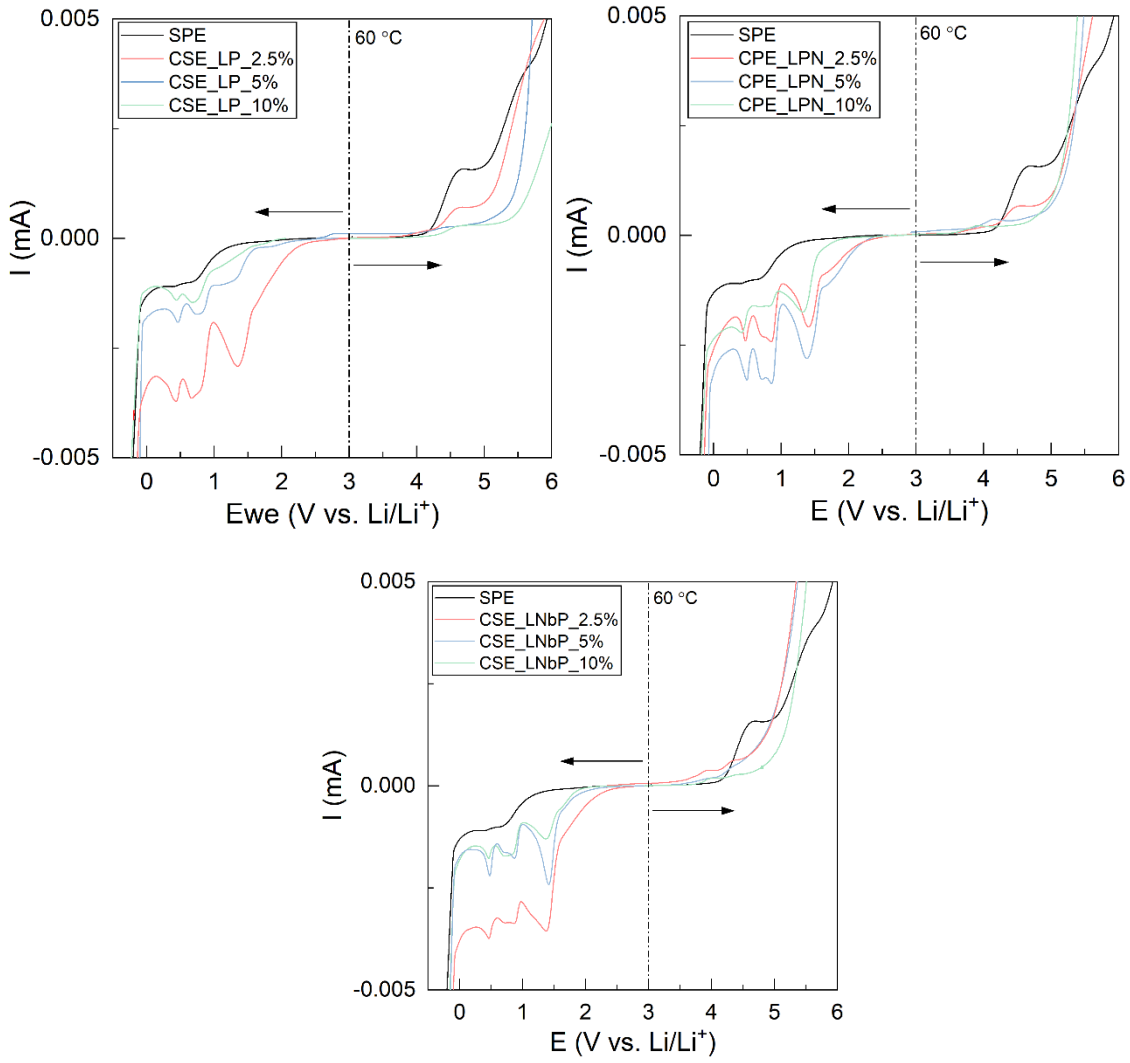

Figure 6-15. Linear sweep voltammetry (LSV) at 60 °C vs. Li/Li^+, of solid polymer electrolyte (SPE) and composite electrolytes (CPE) incorporating different ceramic fillers. Forward and reverse sweeps are indicated by arrows. *(a)* Composite polymer electrolytes containing lithium-phosphate glass; *(b)* Composite solid electrolytes containing lithium-niobium-phosphate glass; and *(c)* Composite polymer electrolytes containing lithium-phosphate-nitride glass at 2.5, 5, and 10 wt%.

Although the majority of the articles reported an increase in oxidation stability of composite solid electrolytes as compared to the polymer precursor electrolyte, none of them explicitly explain its mechanisms. It is known that solid electrolytes such as LLZO, LAGP and LATP display high oxidation stability typical of oxide solid electrolytes [131]. In this way, the composite electrolyte may display higher oxidation potential than SPE because of the higher stability of ceramic oxide filler.

6.4.6.2 **Plating and Stripping**

In order to understand the behavior of solid electrolyte as a conducting medium in solid state batteries, the plating and stripping measurements are a good technique to understand the current density that the electrolyte can handle with regard to the lithium – solid electrolyte interface, which is usually the most problematic (limiting) interface in lithium metal batteries. As a result, Figure 6-16 exhibits the step increase plating and stripping behavior to evaluate the critical current density for dendrite growth for the composition under study. It is possible to observe that most of the samples reached a maximum of 0.21 mA cm^{-2}, including the SPE, where a sudden polarization increases the potential to 5 V. The increasing polarization up to 5 V marks the loss of ionic contact (void generation) between Li metal and solid electrolyte interface, otherwise, a short-circuit due to lithium dendrite penetration would collapse to ~0 V. This loss of contact is likely caused by the low pressure applied which is a characteristic of coin cells.

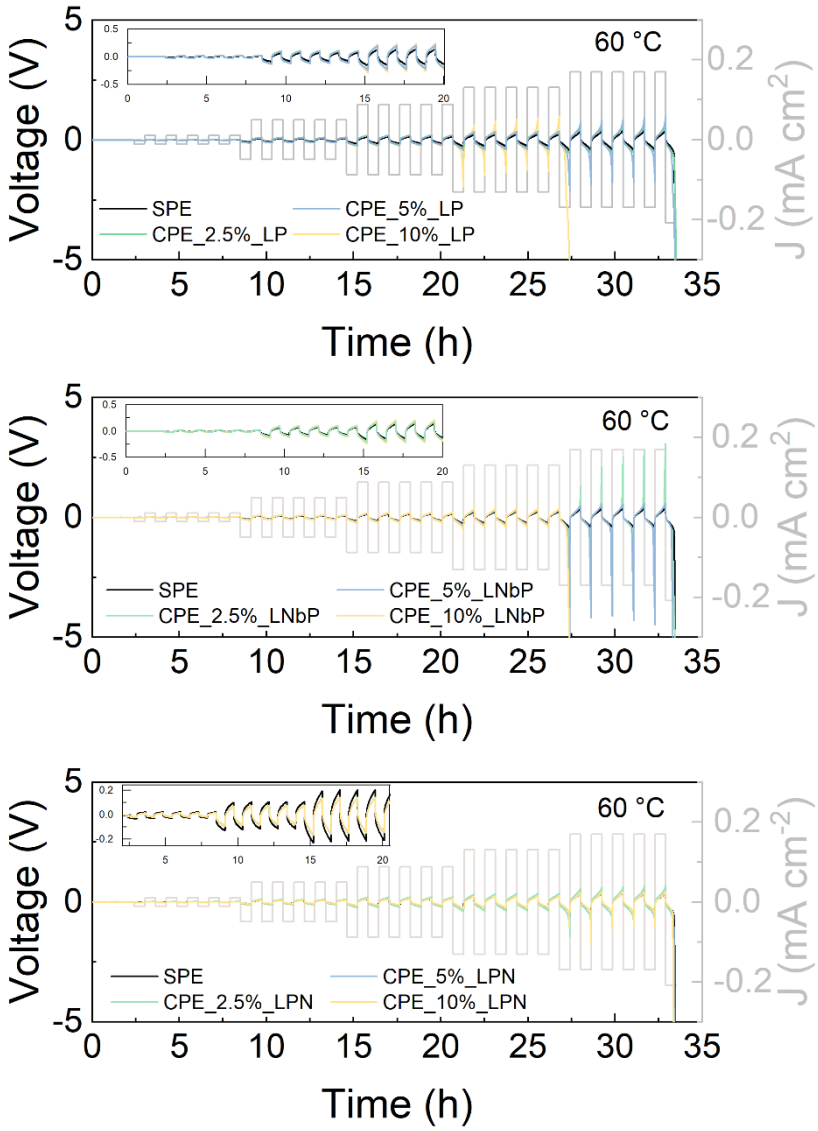

Figure 6-16. Step increased platting and stripping behavior to access critical current for dendrite growth for *(a)* Composite polymer electrolytes containing lithium-phosphate glass; *(b)* Composite solid electrolytes containing lithium-niobium-phosphate glass; and *(c)* Composite polymer electrolytes containing lithium-phosphate-nitride glass at 2.5, 5, and 10 wt%.

Figure 6-17 show galvanostatic Li plating/stripping in symmetric Li|electrolyte|Li cells at 60 °C at constant current density. After an initial activation period with gradually increasing current density, the cells are cycled at a constant density of 0.17 mA cm^{-2}. It is possible to observe a rapid

overpotential growth and failure of SPE at around 55–60 h of cycling. On the other hand, CPE_2.5%_LP shows a lower initial polarization and a much slower amplitude growth, surviving > 80 h without losing contact, while CPE_2.5%_LNbP series reached >140 h, and CPE_2.5%_LPN reached almost 130 h. Although literature in crosslinking solid electrolytes is limited (the crosslinking is vast for gel polymers), LLZTO particles facilitate uniform deposition of Li metal during charge and discharge process in PEO composite electrolytes by minimizing concentration gradients [114,115]. In our case, the ceramic filler may promote a more homogeneous electrodeposition would take longer to lose ionic contact, leading to increasing polarization up to 5V.

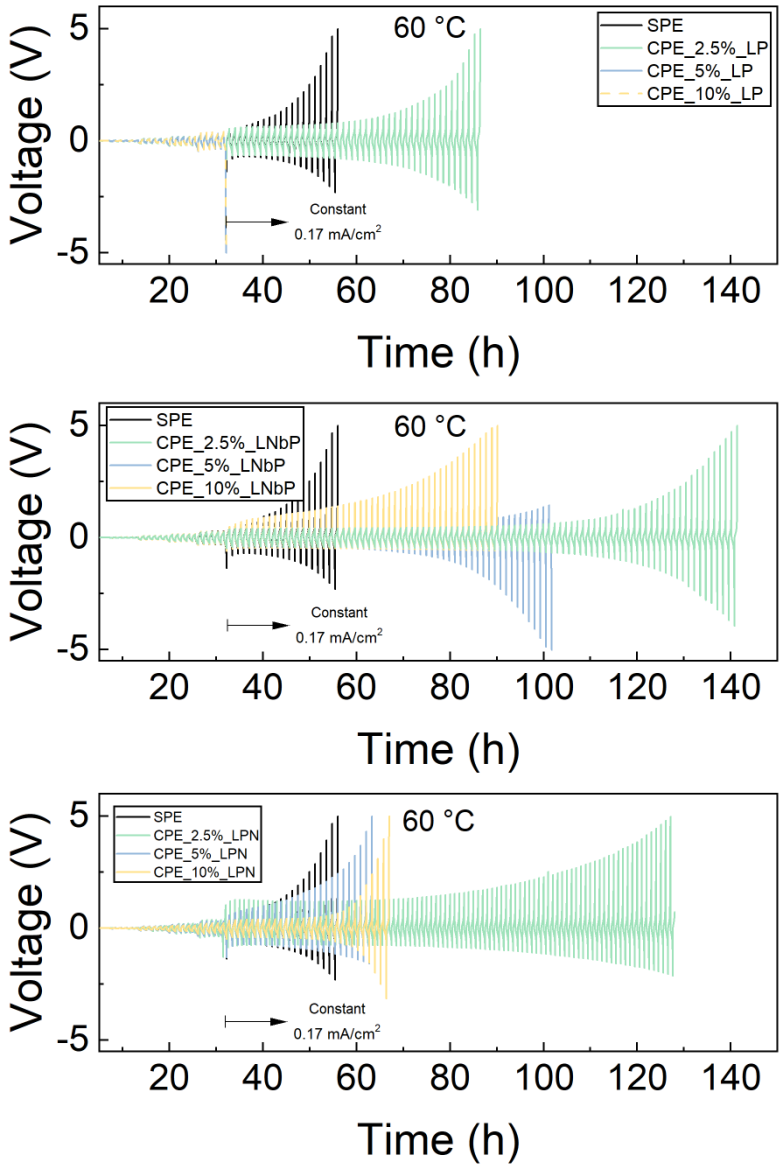

Figure 6-17. Platting and stripping behavior at constant current density for *(a)* Composite polymer electrolytes containing lithium-phosphate glass; *(b)* Composite solid electrolytes containing lithium-niobium-phosphate glass; and *(c)* Composite polymer electrolytes containing lithium-phosphate-nitride glass at 2.5, 5, and 10 wt%.

6.4.6.3 Li/SCE/LFP cell

The plot in Figure 6-18 is a classic C-rate test performed at 60 °C to evaluate the capacity retention under different charge and discharge currents, where the C-rate is stepped from 0.05 C to 2 C and then back down to 0.05 C. The neat solid polymer electrolyte (black) delivers around 70 mAh g^{-1} at 0.05C but loses most of its capacity as the rate approaches 1–2. By contrast, the composite polymer electrolytes (CPEs) that contain 2.5 wt% of ceramic filler retain more capacity, showing a smaller capacity drop at 1–2 C. It is worth mentioning that LiPON doped PEGDA + LiTFSI presented the best performance, highly like due SEI formation of Li_3N and LiF from decomposition of LiPON and LiTFSI, respectively. It is noteworthy that the faster c-rates with greater capacity retention associated with CSE is attributed to minimization of concentration gradients and more homogeneous electrodeposition of Li, as discussed hereinbefore. This behavior is more evident in LiPON most likely related to the chemical composition of SEI layer in contrast to LP and LNbP semples.

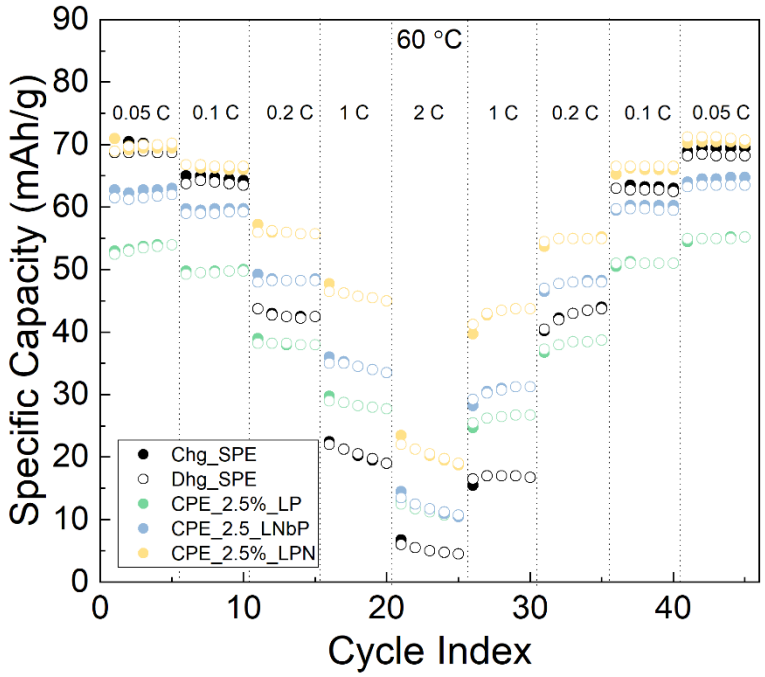

Figure 6-18. Electrochemical performance of Li‖PEGDA–LiTFSI–Ceramic‖LFP cells at 60 °C at different C rates.

6.5 Conclusion

The solvent-free UV-cross-linking strategy developed in this work enabled the fabrication of flexible and homogeneous PEGDA-based composite solid electrolytes incorporating a lithium-phosphate glass, a lithium niobium-phosphate glass, and an amorphous LiPON fillers, whose synergistic effects significantly improved interfacial stability, electrochemical behavior, and cycling performance compared to the neat polymer matrix (SPE). Although filler dispersion varied — ranging from well-distributed LP particles to more agglomeration-prone LNbP and LPN powders — the composites maintained mechanical integrity and showed clear interfacial benefits, markedly suppressing interfacial impedance growth and stabilizing Li interactions relative to the solid polymer electrolyte. All fillers broadened the electrochemical stability window and enabled more stable lithium plating/stripping, extending the cycling

time before cell failure. These interfacial benefits translated into improved rate capability in Li/LFP full cells, particularly for LiPON containing membranes, highlighting the importance of filler chemistry in SEI formation. Overall, this work demonstrates that photo-cross-linked glass–polymer composites are promising solid-state battery electrolytes, offering enhanced performance without the need for solvents or high-temperature processing. In addition, the use of glass and amorphous ceramic fillers results in lower density compared to crystalline solid electrolytes.

CHAPTER 7 SUMMARY AND GENERAL CONCLUSIONS

The growing demand for safer and higher-performance energy storage technologies has intensified research efforts toward solid-state electrolytes. Among the various classes of ionic conductors, glasses offer unique advantages due to their compositional flexibility, absence of grain boundary, lighter weight when compared to crystalline counterparts and no necessity of sintering in high temperature. The biggest drawback of oxide glasses has always been their insufficient ionic conductivity. In this context, the present thesis aimed to deepen the fundamental understanding of ionic conductivity in glasses and to translate these insights into the development of advanced solid-state battery electrolytes.

In Chapter 3, lithium disilicate glass was employed as a model system to critically examine the experimental determination of effective charge carrier density using electrode polarization phenomena. By identifying optimal experimental conditions, this chapter demonstrated that only a small fraction of lithium ions effectively contributes to ionic transport, which provides experimental support for the weak electrolyte model in oxide glasses and establishes a robust methodological framework for subsequent studies.

Building upon this methodology, Chapter 4 systematically investigated the relationship between charge carrier density and mobility as a function of alkali content in $Li_2O–SiO_2$ and $Li_2O–P_2O_5$ glasses, with different alkali contents. At moderate alkali concentrations, increases in ionic conductivity were primarily governed by an increase in the effective number of charge carriers, since the activation energy for ionic mobility remains nearly composition-independent. In contrast, near the vitrification limits of both systems, conductivity enhancement became mobility-controlled, associated with a reduction in the activation energy for ion motion.

Taken together, Chapters 3 and 4 address some fundamental aspects of ionic conductivity in silicate and phosphate glass systems, with particular emphasis on elucidating the importance of effective charge carrier density on

the total ionic conductivity. The results obtained in these chapters are consistent with the Ravaine–Souquet weak-electrolyte theory, in which only a small fraction of ions participates in the conduction mechanism and ionic mobility remains composition-independent across the glass formation range. Consequently, since alkali oxide in oxides glasses are weakly dissociated and mobility seems to not be the dominant limiting factor, strategies aimed at weakening the Li–O bond emerge as a promising route for the design of new glassy solid electrolytes.

Motivated by the some previous results showing that larger halogen anions lead to greater enhancements in ionic conductivity—presumably through the weakening of Li–O bonds—Chapter 5 investigated the possible incorporation of larger anionic species, such as $AlCl_4^-$ (compared to Cl^-), with the expectation of further weakening Li–O interactions. This study demonstrated that ionic conductivity can be significantly enhanced even while reducing the total charge carrier concentration within the glass. Since the addition of $AlCl_3$ does not introduce new cationic charge carriers such as Li^+, the observed conductivity enhancement must arise from a synergistic interaction between chloride anions and the glass network, despite the fact that direct evidence of $AlCl_4^-$ species could not be conclusively identified. Importantly, these results demonstrate a decoupling of ionic conductivity from both total charge carrier concentration and the degree of glass network polymerization.

Finally, Chapter 6 extends this thesis toward technological application. It proposes new pathways for incorporating glassy and amorphous ceramic oxide (an oxynitride composition) into environmentally friendlier, solvent-free composite solid electrolytes for solid-state battery applications. By combining glass and polymer chemistries, this approach highlights the potential of glass-based components in next-generation solid-state batteries.

SUGGESTION FOR FUTURE WORKS

- Extend the methodology developed in this work to investigate ionic transport in silicate glasses with lower alkali concentrations, with particular attention to the effects of glass–glass phase separation on charge carrier density and mobility.
- Apply the same experimental and analytical framework to phosphate glasses with low alkali content, emphasizing compositions with high P_2O_5 concentrations. In this case, glass synthesis in sealed ampules and sample preparation under inert atmosphere (glove box) are recommended to ensure compositional stability.
- Explore advanced solid-state NMR techniques to achieve a deeper understanding of the local environment and role of chloride ions in glassy systems, with special emphasis on the behavior of larger and more complex anionic species.
- Investigate the Li_2O–P_2O_5–AlI_3 and Li_2O–P_2O_5–$AlBr_3$ glass systems and systematically compare their structural and transport properties with those of LiI- and LiBr-containing glasses at equivalent salt concentrations, aiming to elucidate the influence of halide size on ionic conductivity.

BIBLIOGRAPHY

[1] J.-L. Souquet, M.L.F. Nascimento, A.C.M. Rodrigues, Charge carrier concentration and mobility in alkali silicates, J. Chem. Phys. 132 (2010) 034704.

[2] S.W. Martin, W. Yao, K. Berg, Space charge polarization measurements as a method to determine the temperature dependence of the number density of mobile cations in ion conducting glasses, Zeitschrift Für Physikalische Chemie 223 (2009) 1379–1393.

[3] E.D. Zanotto, J.C. Mauro, The glassy state of matter: Its definition and ultimate fate, J. Non. Cryst. Solids 471 (2017) 490–495.

[4] W.H. Zachariasen, The atomic arrangement in glass, J. Am. Chem. Soc. 54 (1932) 3841–3851.

[5] A.K. Varshneya, J.C. Mauro, Fundamentals of Inorganic Glasses, Third, Elsevier, 2019. https://doi.org/10.1016/C2017-0-04281-7.

[6] W.D. Kingery, H.K. Bowen, D.R. Uhlmann, Introduction to ceramics, John wiley & sons, 1976.

[7] H.L. Tuller, D.P. Button, D.R. Uhlmann, Fast ion transport in oxide glasses, J. Non. Cryst. Solids 40 (1980) 93–118.

[8] E.M. Birtch, M.G. Mesko, J.E. Shelby, Phase separation and properties of lithium barium silicate glasses, Physics and Chemistry of Glasses 44 (2003) 319–324.

[9] J.E. Shelby, Introduction to glass science and technology, Royal society of chemistry, 2020.

[10] D. Ravaine, S. JL, A THERMODYNAMIC APPROACH TO IONIC CONDUCTIVITY IN OXIDE GLASSES. 1. CORRELATION OF THE IONIC CONDUCTIVITY WITH THE CHEMICAL POTENTIAL OF ALKALI OXIDE IN OXIDE GLASSES., (1977).

[11] M.L.F. Nascimento, A.C.M. Rodrigues, J.L. Souquet, Microscopic and thermodynamic interpretations of experimental data on ionic conductivity in lithium silicate glasses, Physics and Chemistry of Glasses-European Journal of Glass Science and Technology Part B 51 (2010) 69–77.

[12] E.D. Zanotto, Effect of liquid phase separation on crystal nucleation in glass-formers. Case closed, Ceram. Int. 46 (2020) 24779–24791.

[13] S. V Pershina, A.A. Raskovalov, B.D. Antonov, T. V Yaroslavtseva, O.G. Reznitskikh, Y. V Baklanova, E.D. Pletneva, Extreme behavior of Li-ion conductivity in the Li2O–Al2O3–P2O5 glass system, J. Non. Cryst. Solids 430 (2015) 64–72.

[14] F. Moreau, A. Durán, F. Muñoz, Structure and properties of high Li2O-containing aluminophosphate glasses, J. Eur. Ceram. Soc. 29 (2009) 1895–1902.

[15] B.V.R. Chowdari, K. Radhakrishnan, Electrical and electrochemical characterization of Li2O: P2O5: Nb2O5-based solid electrolytes, J. Non. Cryst. Solids 110 (1989) 101–110.

[16] T. Okada, T. Honma, T. Komatsu, Synthesis and Li+ ion conductivity of Li2O–Nb2O5–P2O5 glasses and glass–ceramics, Mater. Res. Bull. 45 (2010) 1443–1448.

[17] J.P. Malugani, G. Robert, Conductivite ionique dans les verres LiPO3LiX (X= I, Br, Cl), Mater. Res. Bull. 14 (1979) 1075–1081.

[18] A. Levasseur, J.-C. Brethous, J.-M. Réau, P. Hagenmuller, Etude comparée de la conductivité ionique du lithium dans les halogenoborates vitreux, Mater. Res. Bull. 14 (1979) 921–927.

[19] Y. Wang, A. Osaka, Y. Miura, K. Takahashi, Effect of halide ions on Li+ ionic conductivity in oxyhalo-borate glasses, J. Mater. Res. 2 (1987) 606–609.

[20] W. Müller, D. Kruschke, M. Torge, A.-R. Grimmer, H.-J. Schütt, Enhancement of lithium conduction in borate glasses by chloride: An effect of network dilation or bonding strength variation?, Solid State Ion. 23 (1987) 53–58.

[21] V.C.V. Gowda, B.K. Chethana, C.N. Reddy, Ion transport studies in lithium phospho-molybdate glasses containing Cl− ion, Materials Science and Engineering: B 178 (2013) 826–833.

[22] M. Doreau, A. Abou El Anouar, G. Robert, Domaine vitreux, structure et conductivite electrique des verres du systeme LiCl/1b Li2O/1b P2O5, Mater. Res. Bull. 15 (1980) 285–294.

[23] K. Wätzig, J. Schilm, C. Heubner, K. Nikolowski, M. Partsch, Li+ conductivity in the system Li2O-Nb2O5-P2O5-LiCl as solid electrolyte based on synthesized glasses and sintered glass ceramics, Solid State Ion. 372 (2021) 115769.

[24] I.A. Sokolov, A.A. Il'in, N.A. Valova, N.Y. Ustinov, Y.P. Tarlakov, A.A. Pronkin, Investigation of the mechanism of charge carrier migration in glasses of the Li 2 O–P 2 O 5 and LiF–LiPO 3 systems, Glass Physics and Chemistry 29 (2003) 300–305.

[25] A.A. Kiprianov, N.M. Pankratova, Modeling the synthesis of oxyhalide glass of the Li 2 O-LiCl-SiO 2 system, Glass Physics and Chemistry 41 (2015) 359–366.

[26] J. Swenson, L. Börjesson, Correlation between free volume and ionic conductivity in fast ion conducting glasses, Phys. Rev. Lett. 77 (1996) 3569.

[27] S.W. Martin, Ionic conduction in phosphate glasses, Journal of the American Ceramic Society 74 (1991) 1767–1784.

[28] O.L. Anderson, D.A. Stuart, Calculation of activation energy of ionic conductivity in silica glasses by classical methods, Journal of the American Ceramic Society 37 (1954) 573–580.

[29] S.W. Martin, Conductivity Activation Energy Relations in High-Sodium-Content Borate and Aluminoborate Glasses, Journal of the American Ceramic Society 71 (1988) 438–445.

[30] D.P. Almond, G.K. Duncan, A.R. West, The determination of hopping rates and carrier concentrations in ionic conductors by a new analysis of ac conductivity, Solid State Ion. 8 (1983) 159–164.

[31] K. Funke, R. Hackenberg, Ionen-Halleffekt in α-AgJ, Berichte Der Bunsengesellschaft Für Physikalische Chemie 76 (1972) 883–885.

[32] D.S. Newman, C. Frank, R.W. Matlack, S. Twining, V. Krishnan, The ionic hall effect in the solid electrolyte C5H6NAg5I6, Electrochim. Acta 22 (1977) 811–814.

[33] C.H.J. Stuhrmann, H. Kreiterling, K. Funke, Ionic Hall effect measured in rubidium silver iodide, Solid State Ion. 154 (2002) 109–112.

[34] V. Clement, D. Ravaine, C. Déportes, R. Billat, Measurement of Hall mobilites in AgPO AgI glasses, Solid State Ion. 28 (1988) 1572–1578.

[35] J.R. Macdonald, Theory of ac space-charge polarization effects in photoconductors, semiconductors, and electrolytes, Physical Review 92 (1953) 4.

[36] M. Tomozawa, D.-W. Shin, Charge carrier concentration and mobility of ions in a silica glass, J. Non. Cryst. Solids 241 (1998) 140–148.

[37] C. KIM, M. TOMOZAWA, Electrode polarization of glasses, Journal of the American Ceramic Society 59 (1976) 127–130.

[38] P.M. Sutton, Space charge and electrode polarization in glass, I, Journal of the American Ceramic Society 47 (1964) 188–194.

[39] T.M. Proctor, P.M. SUTTON, Space-Charge Development in Glass, Journal of the American Ceramic Society 43 (1960) 173–178.

[40] J.R. MacDonald, Theory of space-charge polarization and electrode-discharge effects, J. Chem. Phys. 58 (1973) 4982–5001.

[41] T.M. Proctor, P.M. Sutton, Static Space-Charge Distributions with a Single Mobile Charge Carrier, J. Chem. Phys. 30 (1959) 212–220.

[42] P.M. SUTTON, Space charge and electrode polarization in glass, II, Journal of the American Ceramic Society 47 (1964) 219–230.

[43] J.H. Beaumont, P.W.M. Jacobs, Polarization in potassium chloride crystals, Journal of Physics and Chemistry of Solids 28 (1967) 657–667.

[44] D.W. Shin, M. Tomozawa, Electrical and dielectric relaxation in silica glasses at low temperature, J. Non. Cryst. Solids 211 (1997) 237–249.

[45] H. Eckert, A.C.M. Rodrigues, Ion-conducting glass-ceramics for energy-storage applications, MRS Bull. 42 (2017) 206–212.

[46] A.M. Cruz, E.B. Ferreira, A.C.M. Rodrigues, Controlled crystallization and ionic conductivity of a nanostructured LiAlGePO4 glass–ceramic, J. Non. Cryst. Solids 355 (2009) 2295–2301.

[47] V.M. Zallocco, J.M. Freitas, N. Bocchi, A.C.M. Rodrigues, Electrochemical stability of a NASICON solid electrolyte from the lithium aluminum germanium phosphate (LAGP) series, Solid State Ion. 378 (2022) 115888.

[48] E. Barsoukov, J.R. Macdonald, Impedance spectroscopy theory, experiment, and, Applications, 2nd Ed.(Hoboken, NJ: John Wiley &Sons, Inc., 2005) (2005).

[49] J.T.S. Irvine, D.C. Sinclair, A.R. West, Electroceramics: characterization by impedance spectroscopy, Advanced Materials 2 (1990) 132–138.

[50] J.C. Dyre, P. Maass, B. Roling, D.L. Sidebottom, Fundamental questions relating to ion conduction in disordered solids, Reports on Progress in Physics 72 (2009) 046501.

[51] S. Fleischmann, Y. Zhang, X. Wang, P.T. Cummings, J. Wu, P. Simon, Y. Gogotsi, V. Presser, V. Augustyn, Continuous transition from double-layer to Faradaic charge storage in confined electrolytes, Nat. Energy 7 (2022) 222–228.

[52] S. Fleischmann, J.B. Mitchell, R. Wang, C. Zhan, D. Jiang, V. Presser, V. Augustyn, Pseudocapacitance: from fundamental understanding to high power energy storage materials, Chem. Rev. 120 (2020) 6738–6782.

[53] R. Xu, X. Shen, X. Ma, C. Yan, X. Zhang, X. Chen, J. Ding, J. Huang, Identifying the critical anion–cation coordination to regulate the electric double layer for an efficient lithium-metal anode interface, Angew. Chem. Int. Ed. 60 (2021) 4215–4220.

[54] J. Wu, Understanding the electric double-layer structure, capacitance, and charging dynamics, Chem. Rev. 122 (2022) 10821–10859.

[55] W. Scheider, Theory of the frequency dispersion of electrode polarization. Topology of networks with fractional power frequency dependence, J. Phys. Chem. 79 (1975) 127–136.

[56] R. De Levie, The influence of surface roughness of solid electrodes on electrochemical measurements, Electrochim. Acta 10 (1965) 113–130.

[57] T. Pajkossy, Impedance of rough capacitive electrodes, Journal of Electroanalytical Chemistry 364 (1994) 111–125.

[58] R. De Levie, On the impedance of electrodes with rough interfaces, J. Electroanal. Chem. Interfacial Electrochem. 261 (1989) 1–9.

[59] R. De Levie, On porous electrodes in electrolyte solutions: I. Capacitance effects, Electrochim. Acta 8 (1963) 751–780.

[60] R. de Levie, Fractals and rough electrodes, J. Electroanal. Chem. Interfacial Electrochem. 281 (1990) 1–21.

[61] P. Córdoba-Torres, T.J. Mesquita, R.P. Nogueira, Relationship between the origin of constant-phase element behavior in electrochemical impedance spectroscopy and electrode surface structure, The Journal of Physical Chemistry C 119 (2015) 4136–4147.

[62] T. Aslyamov, Properties of electrolyte near rough electrodes: capacity and impedance, Curr. Opin. Electrochem. (2022) 101104.

[63] T. Pajkossy, R. Jurczakowski, Electrochemical impedance spectroscopy in interfacial studies, Curr. Opin. Electrochem. 1 (2017) 53–58.

[64] V.M. Zallocco, J.V. Campos, A.C.M. Rodrigues, Interfacial capacitance in lithium disilicate glass: Experimental factors and charge carrier density, Journal of the American Ceramic Society 108 (2025) e20210.

[65] P. Janoš, J. Ederer, V. Pilařová, J. Henych, J. Tolasz, D. Milde, T. Opletal, Chemical mechanical glass polishing with cerium oxide: Effect of selected physico-chemical characteristics on polishing efficiency, Wear 362 (2016) 114–120.

[66] S. Yamockul, N. Thamrongananskul, Cerium Oxide Polishes Lithium Disilicate Glass Ceramic via a Chemical–Mechanical Process, Eur. J. Dent. (2022).

[67] B. Hirschorn, M.E. Orazem, B. Tribollet, V. Vivier, I. Frateur, M. Musiani, Determination of effective capacitance and film thickness from constant-phase-element parameters, Electrochim. Acta 55 (2010) 6218–6227.

[68] A.A. Campos-Júnior, A.C.M. Rodrigues, Ionic blocking effect in partially crystallized lithium disilicate, J. Appl. Phys. 100 (2006) 053709.

[69] P.C. Soares Jr, E.D. Zanotto, V.M. Fokin, H. Jain, TEM and XRD study of early crystallization of lithium disilicate glasses, J. Non. Cryst. Solids 331 (2003) 217–227.

[70] H. Bradtmüller, A. Gaddam, H. Eckert, E.D. Zanotto, Structural rearrangements during sub-Tg relaxation and nucleation in lithium disilicate glass revealed by a solid-state NMR and MD strategy, Acta Mater. 240 (2022) 118318.

[71] M. Müller, H. Auer, A. Bauer, S. Uhlenbruck, M. Finsterbusch, K. Wätzig, K. Nikolowski, S. Dierickx, D. Fattakhova-Rohlfing, O. Guillon, Guidelines to correctly measure the lithium ion conductivity of oxide ceramic electrolytes based on a harmonized testing procedure, J. Power Sources 531 (2022) 231323.

[72] C. Gerhard, A. Taleb, F. Pelascini, J. Hermann, Quantification of surface contamination on optical glass via sensitivity-improved calibration-free laser-induced breakdown spectroscopy, Appl. Surf. Sci. 537 (2021) 147984.

[73] M. Pfiffer, J. Longuet, C. Labrugère, E. Fargin, B. Bousquet, M. Dussauze, S. Lambert, P. Cormont, J. Néauport, Characterization of the polishing-induced contamination of fused silica optics, Journal of the American Ceramic Society 100 (2017) 96–107.

[74] A.-K. Landry, R. Bayzou, A. Benayad, J. Trébosc, F. Pourpoint, O. Lafon, F. Le Cras, B.P. Le Cras, R.B. Nuernberg, Unveiling the origins of high ionic conductivity in lithium phosphorus oxynitride amorphous electrolytes, Chemistry of Materials (2023).

[75] D. Ravaine, S. JL, A THERMODYNAMIC APPROACH TO IONIC CONDUCTIVITY IN OXIDE GLASSES. 1. CORRELATION OF THE IONIC CONDUCTIVITY WITH THE CHEMICAL POTENTIAL OF ALKALI OXIDE IN OXIDE GLASSES., (1977).

[76] Y.H. Rim, M. Kim, C.G. Baek, Y.S. Yang, Effect of Li content in ion conductivity of lithium silicate glasses, J. Alloys Compd. 827 (2020) 154253.

[77] A. López-Grande, R. Dagupati, P. Galán del Sastre, F. Muñoz, Ionic conductivity of Li2O–P2O5 glasses from thermodynamic modeling of their chemical structure, Journal of the American Ceramic Society 104 (2021) 5625–5635.

[78] S.W. Martin, C.A. Angell, Dc and ac conductivity in wide composition range Li2O P2O5 glasses, J. Non. Cryst. Solids 83 (1986) 185–207.

[79] B.V.R. Chowdari, K. Radhakrishnan, Ionic conductivity studies of the vitreous Li2O: P2O5: Ta2O5 system, J. Non. Cryst. Solids 108 (1989) 323–332.

[80] M. Tatsumisago, Y. Kowada, T. Minami, Structure of rapidly quenched lithium phosphate glasses, Physics and Chemistry of Glasses 29 (1988) 63–66.

[81] R.J. Charles, Metastable liquid immiscibility in alkali metal oxide–silica systems, Journal of the American Ceramic Society 49 (1966) 55–62.

[82] M. Shibata, C. Sanchez, H. Patel, S. Feller, J. Stark, G. Sumcad, J. Kasper, The density of lithium borate glasses related to atomic arrangements, J. Non. Cryst. Solids 85 (1986) 29–41.

[83] R. Boekenhauer, H. Zhang, S. Feller, D. Bain, S. Kambeyanda, K. Budhwani, P. Pandikuthira, F. Alamgir, A.M. Peters, S. Messer, The glass transition temperature of lithium borosilicate glasses related to atomic arrangements, J. Non. Cryst. Solids 175 (1994) 137–144.

[84] N. Barrow, M. Packard, S. Vaishnav, M.C. Wilding, P.A. Bingham, A.C. Hannon, M. Appler, S. Feller, MAS-NMR studies of carbonate retention in a very wide range of Na2O-SiO2 glasses, J. Non. Cryst. Solids 534 (2020) 119958.

[85] E.I. Kamitsos, M.A. Karakassides, A.P. Patsis, Spectroscopic study of carbonate retention in high-basicity borate glasses, J. Non. Cryst. Solids 111 (1989) 252–262.

[86] J. Kim, J. Dawb, S. Choi, C. Sharradb, Utilizing Aluminium Chlorides for Oxygen Removal in Molten Fuel Salts, (n.d.).

[87] Y.S. Badyal, D.A. Allen, R.A. Howe, The structure of liquid AlCl3 and structural modification in AlCl3-MCl (M= Li, Na) molten salt mixtures, Journal of Physics: Condensed Matter 6 (1994) 10193.

[88] D. Möncke, M. da Cruz Barbosa Neto, H. Bradtmüller, G.B. de Souza, A.M. Rodrigues, H.S. Elkholy, H.A. Othman, B.J.A. Moulton, E.I. Kamitsos, A.C.M. Rodrigues, NaPO 3-AlF 3 GLASSES: FLUORINE EVAPORATION DURING MELTING AND THE RESULTING VARIATIONS IN STRUCTURE AND PROPERTIES., Journal of Chemical Technology & Metallurgy 53 (2018).

[89] A. Kozmidis-Petrovic, J. Šesták, Forty years of the Hrubý glass-forming coefficient via DTA when comparing other criteria in relation to the glass stability and vitrification ability, J. Therm. Anal. Calorim. 110 (2012) 997–1004.

[90] S.G.J. Van Meerten, W.M.J. Franssen, A.P.M. Kentgens, ssNake: A cross-platform open-source NMR data processing and fitting application, Journal of Magnetic Resonance 301 (2019) 56–66.

[91] U.B. Chanshetti, V.A. Shelke, S.M. Jadhav, S.G. Shankarwar, T.K. Chondhekar, A.G. Shankarwar, V. Sudarsan, M.S. Jogad, Density and molar volume studies of phosphate glasses, Facta Universitatis-Series: Physics, Chemistry and Technology 9 (2011) 29–36.

[92] A. Chatterjee, A. Ghosh, Correlation between ion transport and network structure of Li2O-P2O5 glasses, Solid State Ion. 314 (2018) 1–8.

[93] Y.M. Moustafa, K. El-Egili, Infrared spectra of sodium phosphate glasses, J. Non. Cryst. Solids 240 (1998) 144–153.

[94] H.A.A. Sidek, S.P. Chow, Z.A. Talib, S.A. Halim, Formation and elastic properties of lithium chlorophosphate glasses, Solid State Science and Technology 11 (2003) 103–108.

[95] L. Ouachouo, L. Bih, M. Jerroudi, Effect of halide addition on thermal and elastic properties of binary Li2O-P2O5 glasses, Mater. Today Proc. 58 (2022) 1415–1418.

[96] K. Muruganandam, M. Seshasayee, S. Patnaik, An X-ray RDF study of Li2O□ P2O5□ LiCl glasses, Solid State Ion. 89 (1996) 313–319.

[97] H. Bradtmüller, L. Zhang, C.C. de Araujo, H. Eckert, D. Moncke, D. Ehrt, Structural studies of NaPO3–AlF3 glasses by high-resolution double-resonance nuclear magnetic resonance spectroscopy, The Journal of Physical Chemistry C 122 (2018) 21579–21588.

[98] Z. Zhang, J. Ren, L. Hu, Fast Ionic Conducting Glasses in the System 20LiCl–40Li2O–(80–x) PO5/2–x MoO3: The Structural Dependence of Ion Conductivity Studied by Solid-State Nuclear Magnetic Resonance Spectroscopy, The Journal of Physical Chemistry C 124 (2020) 6528–6535.

[99] G. Czjzek, J. Fink, F. Götz, H. Schmidt, J.M.D. Coey, J.-P. Rebouillat, A. Liénard, Atomic coordination and the distribution of electric field gradients in amorphous solids, Phys. Rev. B 23 (1981) 2513.

[100] S.K. Lee, J.F. Stebbins, The structure of aluminosilicate glasses: high-resolution 17O and 27Al MAS and 3QMAS NMR study, J. Phys. Chem. B 104 (2000) 4091–4100.

[101] L. Zhang, H. Eckert, Short-and medium-range order in sodium aluminophosphate glasses: new insights from high-resolution dipolar solid-state NMR spectroscopy, J. Phys. Chem. B 110 (2006) 8946–8958.

[102] S. Wegner, L. van Wüllen, G. Tricot, The structure of aluminophosphate glasses revisited: Application of modern solid state NMR strategies to determine structural motifs on intermediate length scales, J. Non. Cryst. Solids 354 (2008) 1703–1714.

[103] P. Richet, Encyclopedia of Glass Science, Technology, History, and Culture, 2 Volume Set, John Wiley & Sons, 2026.

[104] R. Chen, Q. Li, X. Yu, L. Chen, H. Li, Approaching practically accessible solid-state batteries: stability issues related to solid electrolytes and interfaces, Chem. Rev. (2019).

[105] J. Feng, L. Wang, Y. Chen, P. Wang, H. Zhang, X. He, PEO based polymer-ceramic hybrid solid electrolytes: a review, Nano Converg. 8 (2021) 2.

[106] Y. Song, M. Su, H. Xiang, J. Kang, W. Yu, Z. Peng, H. Wang, B. Cheng, N. Deng, W. Kang, PEO-Based Solid-State Polymer Electrolytes for Wide-Temperature Solid-State Lithium Metal Batteries, Small 21 (2025) 2408045.

[107] S. Chen, D. Xie, G. Liu, J.P. Mwizerwa, Q. Zhang, Y. Zhao, X. Xu, X. Yao, Sulfide solid electrolytes for all-solid-state lithium batteries: Structure, conductivity, stability and application, Energy Storage Mater. 14 (2018) 58–74.

[108] X. Nie, J. Hu, C. Li, Halide-based solid electrolytes: The history, progress, and challenges, Interdisciplinary Materials 2 (2023) 365–389.

[109] K.J. Kim, M. Balaish, M. Wadaguchi, L. Kong, J.L.M. Rupp, Solid-state Li–metal batteries: challenges and horizons of oxide and sulfide solid electrolytes and their interfaces, Adv. Energy Mater. 11 (2021) 2002689.

[110] P. Jiang, G. Du, J. Cao, X. Zhang, C. Zou, Y. Liu, X. Lu, Solid-State Li Ion Batteries with Oxide Solid Electrolytes: Progress and Perspective, Energy Technology 11 (2023) 2201288.

[111] M. Hou, F. Liang, K. Chen, Y. Dai, D. Xue, Challenges and perspectives of NASICON-type solid electrolytes for all-solid-state lithium batteries, Nanotechnology 31 (2020) 132003.

[112] M. Dirican, C. Yan, P. Zhu, X. Zhang, Composite solid electrolytes for all-solid-state lithium batteries, Materials Science and Engineering: R: Reports 136 (2019) 27–46.

[113] J. Zhang, N. Zhao, M. Zhang, Y. Li, P.K. Chu, X. Guo, Z. Di, X. Wang, H. Li, Flexible and ion-conducting membrane electrolytes for solid-state lithium batteries: Dispersion of garnet nanoparticles in insulating polyethylene oxide, Nano Energy 28 (2016) 447–454.

[114] J. Zagórski, J.M. López del Amo, M.J. Cordill, F. Aguesse, L. Buannic, A. Llordés, Garnet–polymer composite electrolytes: new insights on local Li-ion dynamics and electrodeposition stability with Li metal anodes, ACS Appl. Energy Mater. 2 (2019) 1734–1746.

[115] L. Chen, Y. Li, S.-P. Li, L.-Z. Fan, C.-W. Nan, J.B. Goodenough, PEO/garnet composite electrolytes for solid-state lithium batteries: From

"ceramic-in-polymer" to "polymer-in-ceramic," Nano Energy 46 (2018) 176–184.

[116] S.H.-S. Cheng, K.-Q. He, Y. Liu, J.-W. Zha, M. Kamruzzaman, R.L.-W. Ma, Z.-M. Dang, R.K.Y. Li, C.Y. Chung, Electrochemical performance of all-solid-state lithium batteries using inorganic lithium garnets particulate reinforced PEO/LiClO4 electrolyte, Electrochim. Acta 253 (2017) 430–438.

[117] M. Keller, G.B. Appetecchi, G.-T. Kim, V. Sharova, M. Schneider, J. Schuhmacher, A. Roters, S. Passerini, Electrochemical performance of a solvent-free hybrid ceramic-polymer electrolyte based on Li7La3Zr2O12 in P (EO) 15LiTFSI, J. Power Sources 353 (2017) 287–297.

[118] Q. Li, Y. Li, H. Chen, H. Liu, L. Li, J. Song, M. Xu, S.-J. Bao, Dry approach production of a garnet solid electrolyte membrane for lithium batteries, Inorg. Chem. Front. 10 (2023) 6023–6031.

[119] T. Jiang, P. He, G. Wang, Y. Shen, C. Nan, L. Fan, Solvent-free synthesis of thin, flexible, nonflammable garnet-based composite solid electrolyte for all-solid-state lithium batteries, Adv. Energy Mater. 10 (2020) 1903376.

[120] T. Vallier, R.B. Nuernberg, S. Issa, J.-L. Ferrandis, L. Stievano, B. Ameduri, V. Lapinte, L. Monconduit, Understanding Na+ Diffusion, Physicochemical Behavior, and Electrochemical Performance of a Gel Polymer Electrolyte, ACS Appl. Mater. Interfaces 16 (2024) 29077–29086.

[121] X. Wang, J. Chen, M. Gao, S. Xiao, Z. Guo, Application of Polymer Electrolytes Prepared by Ultraviolet Polymerization in Various Lithium Metal Battery Systems, ACS Appl. Energy Mater. 8 (2025) 5564–5584.

[122] Y. Ji, C. Zhang, X. Xu, J. Zhao, J. Liu, Y. Huo, Green and Environmentally Friendly Photopolymerization Technology to Solid/Quasi-Solid Polymer Electrolytes for Rechargeable Batteries: Recent Progress and Prospects, Small (2025) e09388.

[123] R. Khurana, J.L. Schaefer, L.A. Archer, G.W. Coates, Suppression of lithium dendrite growth using cross-linked polyethylene/poly (ethylene

oxide) electrolytes: a new approach for practical lithium-metal polymer batteries, J. Am. Chem. Soc. 136 (2014) 7395–7402.

[124] X. Yu, Y. Liu, J.B. Goodenough, A. Manthiram, Rationally designed PEGDA–LLZTO composite electrolyte for solid-state lithium batteries, ACS Appl. Mater. Interfaces 13 (2021) 30703–30711.

[125] Machet Constantin, Étude d'une nouvelle voie de synthèse pour les électrolytes solides de type LiPON, Bordeaux, 2025.

[126] J. Zagorski, B. Silvan, D. Saurel, F. Aguesse, A. Llordes, Importance of composite electrolyte processing to improve the kinetics and energy density of Li metal solid-state batteries, ACS Appl. Energy Mater. 3 (2020) 8344–8355.

[127] M.T. Rahman, Z. Barikbin, A.Z.M. Badruddoza, P.S. Doyle, S.A. Khan, Monodisperse polymeric ionic liquid microgel beads with multiple chemically switchable functionalities, Langmuir 29 (2013) 9535–9543.

[128] R. Bakar, S. Darvishi, U. Aydemir, U. Yahsi, C. Tav, Y.Z. Menceloglu, E. Senses, Decoding polymer architecture effect on ion clustering, chain dynamics, and ionic conductivity in polymer electrolytes, ACS Appl. Energy Mater. 6 (2023) 4053–4064.

[129] J.-H. Choi, C.-H. Lee, J.-H. Yu, C.-H. Doh, S.-M. Lee, Enhancement of ionic conductivity of composite membranes for all-solid-state lithium rechargeable batteries incorporating tetragonaláLi7La3Zr2O12 into a polyethylene oxide matrix, J. Power Sources 274 (2015) 458–463.

[130] J. Zheng, M. Tang, Y. Hu, Lithium ion pathway within Li7La3Zr2O12-polyethylene oxide composite electrolytes, Angew. Chem. Int. Ed. 55 (2016) 12538–12542.

[131] Y. Zhu, X. He, Y. Mo, Origin of outstanding stability in the lithium solid electrolyte materials: insights from thermodynamic analyses based on first-principles calculations, ACS Appl. Mater. Interfaces 7 (2015) 23685–23693.

APPENDIX A

Table S1. ^{31}P isotropic chemical shift, δ_{iso}^{CS}, full width at half maximum, FWHM, chemical shift anisotropy, Δ_{CSA}, asymmetry parameter, η_{CS}, area fraction, f, and average degree of polymerization, $< n >$, obtained from the deconvolution model of the spectra shown in Figure 5-1.

Parameter /Sample	δ_{iso}^{CS} / ppm (± 0.1)	FWHM / ppm (± 0.5)	Δ_{CSA} / ppm (± 10)	η_{CS} (±0.2)	f / % (±1)
100-x (55Li_2O-45P_2O_5) · x $AlCl_3$					
x = 0 – <*n*> = 1.82					
P^1	-3.8	5.9	84	0.8	18
P^2	-21.8	9.2	-122	0.5	82
x = 5 – <*n*> = 1.96					
P^1	-3.8	5.9	89	0.8	11
P^2	-21.8	9.2	-124	0.5	66
P^2_{1Al}	-11.4	9.2	81	0.7	16
P^3_{1Al} / P^4_{2Al}	-29.7	9.6	93	1.0	6
P^3	-39.0	9.0	96	0.7	1
x = 10 – <*n*> = 2.02					
P^1	-3.8	5.9	89	0.7	8
P^2	-21.4	9.7	-116	0.5	56
P^2_{1Al}	-11.4	9.6	85	0.9	26
P^3_{1Al} / P^4_{2Al}	-29.7	9.6	93	1.0	9
P^3	-39.0	9	96	0.7	1
x = 15 – <*n*> = 2.02					
P^1	-3.8	6.7	82	0.8	6
P^2	-20.6	11.2	-92	1.0	45
P^2_{1Al}	-11.1	10.9	-86	0.6	41
P^3_{1Al} / P^4_{2Al}	-29.7	10.5	80	1.0	7
P^3	-39.0	10.0	78	1.0	1
100-x (60Li_2O-40P_2O_5) · x $AlCl_3$					
x = 0 – <*n*> = 1.54					
P^1	-3.4	6.0	83	0.8	46
P^2	-20.2	9.9	-115	0.6	54
x = 5 – <*n*> = 1.76					
P^1	-3.4	5.9	87	0.7	27
P^2	-20.2	10.0	-110	0.6	44
P^2_{1Al}	-9.6	9.2	-78	0.9	26
P^3_{1Al} / P^4_{2Al}	-28.5	10.9	119	1.0	3
x = 10 – <*n*> = 1.79					
P^1	-3.4	6.2	82	0.7	24
P^2	-19.4	10.2	-104	0.7	32
P^2_{1Al}	-9.5	9.4	-78	0.9	41
P^3_{1Al} / P^4_{2Al}	-28.5	12.4	61	0.1	3
x = 15 – <*n*> = 1.84					
P^1	-3.1	6.3	80	0.7	18
P^2	-18.9	10.6	-94	0.6	32
P^2_{1Al}	-9.6	9.6	-79	1.0	48
P^3_{1Al} / P^4_{2Al}	-28.5	12.2	56	0.0	2
100-x (60Li_2O-40P_2O_5) · x Al_2O_3					
x = 2.5 – <*n*> = 1.66					

P^1	-3.4	6.1	83	0.75	35
P^2	-19.8	10.1	-109	0.6	38
P^2_{1Al}	-9.7	9.2	-78	1.0	26
P^3_{1Al} / P^4_{2Al}	-30.8	14.1	129	0.4	2
x = 5 – <*n*> = 1.76					
P^1	-3.0	6.4	80	0.8	27
P^2	-19.0	9.4	-98	0.7	23
P^2_{1Al}	-9.7	9.5	-78	1.0	47
P^3_{1Al} / P^4_{2Al}	-28.5	10.6	99	0.6	3
100-x ($64.5Li_2O$-$34.5P_2O_5$) · x $AlCl_3$					
x = 0 – <*n*> = 1.26					
P^1	-2.9	6.0	-77	1.0	72
P^2	-18.4	9.7	-107	0.6	28
x = 5 – <*n*> = 1.50					
P^1	-2.9	6.3	-76	1.0	49
P^2	-18.4	9.1	-96	0.8	14
P^2_{1Al}	-9.1	9.0	-77	1.0	35
P^3_{1Al} / P^4_{2Al}	-28.5	11.0	110	0.0	1
P^0	7.0	6.0	36	0.0	1
x = 10 – <*n*> = 1.68					
P^1	-2.9	6.7	-75	0.6	29
P^2	-18.2	10.0	-98	0.8	18
P^2_{1Al}	-9.0	9.5	-77	1.0	49
P^3_{1Al} / P^4_{2Al}	-28.5	12.0	118	0.0	1
P^0	7.0	6.0	104	0.0	2
P^1_{1Al} / P^2_{2Al}	2.8	4.7	66	1.0	1
x = 15 – <*n*> = 1.78					
P^1	-2.9	6.7	-67	0.9	19
P^2	-17.3	10.7	-76	0.6	23
P^2_{1Al}	-9.2	10.0	-69	0.9	48
P^3_{1Al} / P^4_{2Al}	-28.5	12.0	87	0.0	3
P^0	7.0	6.0	77	1.0	2
P^1_{1Al} / P^2_{2Al}	2.8	4.7	61	1.0	5

Table S2. ^{27}Al isotropic chemical shift, δ_{iso}^{CS}, full width at half maximum, FWHM, width, σ, and area fraction *f*, obtained from the deconvolution model of the spectra shown in Figure 5-4. Note that the average C_Q value is twice the Czjzek distribution width σ in good approximation.

Parameter / Sample	**δ_{iso}^{CS} / ppm (± 1)**	**FWHM / ppm (± 1)**	**σ / MHz (± 0.25)**	***f* / % (±2)**
100-x($55Li_2O$-$45P_2O_5$)x$AlCl_3$				
x = 5				
Al^4	43.3	11.5	3.3	19
Al^5	16.4	9.2	2.4	20
Al^6	-9.2	5.8	2.4	61
x = 10				
Al^4	44.3	12.0	2.5	22
Al^5	16.8	10.0	3.5	23
Al^6	-9.0	6.5	2.4	55
x = 15				

Al^4	45.2	12.3	2.5	30
Al^5	17.6	10.0	3.6	26
Al^6	-8.8	6.7	2.4	44
100-x(60Li_2O-40P_2O_5)x$AlCl_3$				
x = 5				
Al^4-O-Al^4	66.2	38.5	2.9	5
Al^4	46.0	11.8	2.7	12
Al^5	19.4	8.9	4.1	22
Al^6	-8.0	6.2	2.3	61
x = 10				
Al^4-O-Al^4	66.2	38.5	2.9	3
Al^4	46.2	10.5	2.6	12
Al^5	19.9	8.4	4.1	23
Al^6	-7.9	6.1	2.3	62
x = 15				
Al^4-O-Al^4	66.2	38.5	2.9	3
Al^4	46.7	11.3	2.7	17
Al^5	20.0	8.3	4.1	26
Al^6	-8.0	6.3	2.3	54
100-x(60Li_2O-40P_2O_5)xAl_2O_3				
x = 2.5				
Al^4-O-Al^4	57.5	38.5	2.9	4
Al^4	45.8	8.2	3.1	8
Al^5	16.2	8.5	3.2	13
Al^6	-9.6	6.0	2.4	75
x = 5				
Al^4-O-Al^4	-	-	-	-
Al^4	47.1	9.9	3.0	13
Al^5	17.0	8.5	3.4	18
Al^6	-9.4	6.0	2.4	69
100-x(64.5Li_2O-35.5P_2O_5)x$AlCl_3$				
x = 5				
Al^4-O-Al^4	66.2	25.6	2.9	2
Al^4	49.2	10.4	3.1	10
Al^5	21.0	7.0	4.4	21
Al^6	-7.6	5.9	2.3	66
x = 10				
Al^4-O-Al^4	-	-	-	-
Al^4	45.4	11.5	2.6	15
Al^5	18.8	7.59	4.0	20
Al^6	-9.1	5.6	2.4	65
x = 15				
Al^4-O-Al^4	66.2	29.7	2.5	3
Al^4	50.5	11.4	2.9	57
Al^5	19.8	10.7	3.7	22
Al^6	-8.7	8.3	2.3	18